AD-A020 708

PASSIVE NOSETIP TECHNOLOGY (PANT) PROGRAM.   VOLUME X.
SUMMARY OF EXPERIMENTAL AND ANALYTICAL RESULTS

M. R. Wool

Acurex Corporation
Mountain View, California

January 1975

055040

SAMSO-TR-74-86
Volume X

INTERIM REPORT
PASSIVE NOSETIP TECHNOLOGY
(PANT) PROGRAM

Volume X.   Summary of Experimental and Analytical Results
(for the Period May 1973 to December 1974)

Edited by

M. R. Wool

Aerotherm Division/Acurex Corporation

SAMSO-TR-74-86

January 1975

D D C
RECEIVED
FEB 17 1976
A·⌐

AEROTHERM REPORT 74-100

Air Force Space and Missile
Systems Organization
Los Angeles, California

Contract F04701-71-C-0027

INTERIM REPORT
PASSIVE NOSETIP TECHNOLOGY
(PANT) PROGRAM

Volume X. Summary of Experimental and Analytical Results
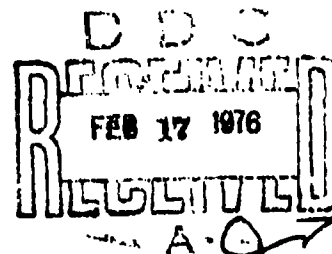(for the Period May 1973 to December 1974)

Edited by

M. R. Wool

FOREWORD

This document is Volume X of the Interim Report series for the Passive Nosetip Technology (PANT) program. A summary of the documents in this series prepared to date is as follows:

Volume I   – Program Overview (U)

Volume II   – Environment and Material Response Procedures for Nosetip Design (U)

Volume III – Surface Roughness Effects

        Part I   – Experimental Data

        Part II   – Roughness Augmented Heating Data Correlation and Analysis (U)

        Part III – Boundary Layer Transition Data Correlation and Analysis (U)

Volume IV   – Heat Transfer and Pressure Distributions on Ablated Shapes

        Part I   – Experimental Data

        Part II   – Data Correlation and Analysis

Volume V   – Definition of Shape Change Phenomenology from Low Temperature Ablator Experiments

        Part I   – Experimental Data, Series C (Preliminary Test Series)

        Part II   – Experimental Data, Series D (Final Test Series)

        Part III – Shape Change Data Correlation and Analysis

Volume VI   – Graphite Ablation Data Correlation and Analysis (U)

Volume VII – Computer User's Manual, Steady-State Analysis of Ablating Nosetips (SAANT) Program

Volume VIII – Computer User's Manual, Passive Graphite Ablating Nosetip (PAGAN) Program

Volume IX   – Unsteady Flow on Ablated Nosetip Shapes – PANT Series G Test and Analysis Report

Volume X   - Summary of Experimental and Analytical Results

Volume XI   - Analysis and Review of the ABRES Combustion Test Facility
                for High Pressure Hyperthermal Reentry Nosetip Systems
                Tests

Volume XII   - Nosetip Transition and Shape Change Tests in the AFFDL 50
                MW RENT Arc - Data Report

Volume XIII   - An Experimental Study to Evaluate Heat Transfer Rates to
                Scalloped Surfaces - Data Report

Volume XIV   - An Experimental Study to Evaluate the Irregular Nosetip
                Shape Regime - Data Report

Volume XV   - Roughness Induced Transition Experiments - Data Report

This report was prepared by Aerotherm Division/Acurex Corporation under
Contract F04701-71-C-0027. Volumes I through IX covered PANT activities from
April 1971 through April 1973. Volumes X through XV represent contract efforts
from May 1973 to December 1974. Volume X summarizes the respective test pro-
grams and describes improvements in nosetip analysis capabilities. Volume XI
presents an evaluation of the ABRES test facility in terms of performing ther-
mostructural and reentry flight simulation testing. Volumes XII through XV are
data reports which summarize the experiments performed for the purpose of de-
fining the irregular flight regime. The analysis of these data are presented
in Volume X.

This work was administered under the direction of the Space and Missile
Systems Organization with Lieutenant A. T. Hopkins and Lieutenant E. G. Taylor
as Project Officers with Mr. W. Portenier and Dr. R. L. Baker of the Aerospace
Corporation serving as principal technical monitors. Mr. D. L. Baker was the
Aerotherm Program Manager, and Mr. M. R. Wool was the Aerotherm Project Engi-
neer.

This technical report has been reviewed and is approved.

E G Taylor

E. G. Taylor, Lt., USAF
Project Officer
Aero and Materials Division
Directorate of Systems Engineering
Deputy for Reentry Systems

ABSTRACT

Results from experimental and analytical efforts performed on the Passive Nosetip Technology (PANT) program between May 1973 and December 1974 are reported. Four test programs were conducted consisting of one test series in the AFFDL 50 MW arc heater, and three test series in the Naval Ordnance Laboratory, Wind Tunnel No. 8. Test objectives and nominal results are summarized for each test series. Analysis of heat transfer and boundary layer transition data are described and changes to nosetip analysis procedures are recommended. The effect of modeling changes on nosetip response predictions are illustrated for several flight environment cases.

TABLE OF CONTENTS

LIST OF FIGURES

LIST OF FIGURES (Concluded)

LIST OF TABLES

LIST OF SYMBOLS

B'	dimensionless blowing rate
C_{H_S}	smooth wall Stanton number
$C_{H,C,S}$	heat transfer coefficient, composite, smooth wall
$C_{H,C,R}$	heat transfer coefficient, composite, rough wall
$C_{H,T,R}$	heat transfer coefficient, transitional, rough wall
D_e	nozzle exit diameter (inches)
D^*	throat diameter (inches)
h_e	local boundary layer edge enthalpy
h_o	stagnation enthalpy
h_w	wall enthalpy
H_B	bulk stagnation enthalpy
H_C	chamber stagnation enthalpy
k	sandgrain roughness height
k_t	turbulent roughness height
k_{PV}	peak to valley roughness
K_r	heating augmentation factor
M_∞	free stream Mach number
P_c	nozzle chamber pressure
P_o	stagnation pressure

P_{t_2} — stagnation pressure behind normal shock

R_L — laminar Reynolds analogy factor

R_N — nose radius

R_S — shoulder radius

R_T — turbulent Reynolds analogy factor

Re_e — edge Reynolds number $(\rho_e u_e / \mu_e)$

Re_k — boundary layer edge Reynolds number based on roughness height $= \rho_e u_e k / \mu_e$

Re_θ — momentum thickness Reynolds number $(\rho_e u_e \theta / \mu_e)$

Re_∞ — Reynolds number $(\rho_\infty u_\infty / \mu_\infty)$ ft^{-1}

S — surface stream length

T_e — local boundary layer edge temperature

T_o — stagnation temperature

T_r — recovery temperature

T_w — wall temperature

u_e — local boundary layer edge velocity

u_∞ — free stream velocity

γ_e — entry angle

δ_{SL} — laminar sublayer thickness

θ — boundary layer momentum thickness

LIST OF SYMBOLS (Concluded)

ψ effective wall cooling ratio

ρ_e local boundary layer edge density

ρ_∞ free stream density

μ_e local boundary layer edge viscosity

μ_∞ free stream viscosity

$(\tilde{\ })$ quantities evaluated at the reference enthalpy temperature

SECTION 1

INTRODUCTION

During the period April 1971 through April 1973, the Aerotherm
Division of Acurex Corporation was involved in the development of reentry-
vehicle, passive nosetip design tools under the SAMSO sponsored Passive
Nosetip Technology (PANT) program. The effort included experimental and
analytical investigations of the fundamental phenomena controlling the
response of nosetip materials. Results of this effort were reported in
the PANT program, Interim Final Report, dated January 1974, Reference 1-1.
The significant findings consisted of the following:

- The importance of the nosetip surface roughness on boundary
  layer transition and heat transfer was demonstrated through
  wind tunnel simulation experiments.

- Wind tunnel simulation experiments also demonstrated that the
  surface temperature to boundary layer edge temperature ratio
  significantly influences the location and occurrence of bound-
  ary layer transition.

- Nosetip ablation tests in both wind tunnel and hyperthermal
  facilities indicated that surface roughness patterns (i.e.,
  scallops) which affect heat transfer, develop during turbu-
  lent ablation.

- Consideration of roughness effects on heat transfer indicated
  that the micromechanical particulate component of graphitic
  nosetip mass loss is negligible and that graphite mass loss
  and surface temperature data can be predicted utilizing equi-
  librium thermochemistry theory.

- Nosetip shape-change data, primarily from wind tunnel tests,
  indicated that nosetip ablation can produce irregular (slen-
  der or asymmetric) shapes which are prone to gross failures.

Computational procedures developed to model the above findings were only
partially successful due in part to the tendency of nosetips to develop
an irregular shape in some environmental regimes. Further efforts to
better understand boundary layer transition, roughness pattern effects

1

on heating, and irregular shape onset were, therefore, recommended to SAMSO. These additional activities were performed under PANT program work statement, paragraph 4.2.5, between May 1973 and December 1974 and are documented in Interim Report Volumes XI through XV.

The general objective of Task 4.2.5 was to define the reentry regimes which produce irregular nosetip shapes. In order to satisfy this objective a sieres of wind tunnel and high-pressure ablation tests was required. The tests were designed to obtain calorimeter and shape-change data for geometries and envionments of interest. The specific objectives of the four-test series are given below:

> 50 MW Arc Heater Tests — Test ATJ-S graphite, Mod-III carbon/ carbon, and reverse chevron carbon phenolic nosetip models in the 50 MW arc using a $M_\infty = 3$ nozzle to assess the transition behavior and shape-change response of "real" materials in a hyperthermal environment.

> Series H Wind Tunnel Tests — Generate heat transfer data for a calorimeter replica of an LTA scallop roughened surface for comparison with inferred heat transfer data and predictions.

> Series I Wind Tunnel Tests — Generate low temperature ablator (LTA) shape change data to determine the effect of relevant nosetip parameters on the formation and extent of irregular shapes.

> Series J Wind Tunnel Tests — Generate heat transfer data which show the effect of surface roughness and model size on boundary layer transition.

The 50 MW tests were conducted in the RENT leg of the 50 MW arc facility at the Air Force Materials Flight Dynamics Laboratory. Test Series H and J were conducted in Tunnel No. 8 at the Naval Ordnance Laboratory (NOL) from February 21 to February 26, 1974. Test Series I was conducted at NOL from March 27 to April 4, 1974.

These test series complement Series E and G which were directed at obtaining pressure data on nosetips of irregular shape. A brief description of these two test series is given below:

> Series E (Task 4.2.3) — Generate high-frequency pressure, acceleration, and shock-shape stability data to establish the occurrence of high-frequency flow field pulsations on ablated nosetip shapes.

Series G (Task 4.2.7) — Generate high-frequency pressure, accelera-
tion, and shock-shape stability data to determine the envelope
of realisitic nosetip shapes which induce high-frequency flow
field pulsations.

Test Series E and G were conducted in NOL Tunnel No. 8; Series E
was conducted in October of 1972 and Series G was conducted from July 25
to August 1, 1973. Series E and G data are reported in Reference 1-2.

Volume XI of the Interim Report series documents an ancillary analy-
sis of calibration data and reentry simulation capabilities of the ABRES
Combustion Test Facility at the Air Force Rocket Propulsion Laboratory and
is not summarized herein. Data reports for the four test series performed
under Task 4.2.5 are included as Volumes XII, XIII, XIV, and XV. In this vol-
ume, the results of the various nosetip experiments and the associated
improvements in response modeling procedures are summarized. In Section 2,
the 50 MW arc ablation test series is summarized. In Section 3, the
Series H wind tunnel test results and other scallop effects data are pre-
sented. The Series I shape-change data and response trends are summarized
in Section 4, and the Series J data are reviewed in Section 5. Section 6
includes a review of response modeling improvements and indicates the
overall effects of the improvements on the predictions for seven baseline
flight cases. Conclusions and recommendations from the program are re-
viewed in Section 7.

SECTION 1 REFERENCES

1-1. "Passive Nosetip Technology (PANT) Program, Interim Report, Volumes
     I through VIII," SAMSO-TR-74-86, Aerotherm Report 74-90, Aerotherm
     Division, Acurex Corporation, January 1974.

1-2. Abbett, M. J., et al., "Passive Nosetip Technology (PANT) Program,
     Interim Report, Volume IX, Unsteady Flow on Ablated Nosetip Shapes,
     PANT Series G Test and Analysis Report," SAMSO-TR-74-06, Aerotherm
     Report 73-87, Aerotherm Division/Acurex Corporation, December 1973.

SECTION 2

AFFDL 50 MW ARC TESTS

The Fall 1973 PANT test series at the AFFDL 50 MW RENT facility
was conducted for two purposes:

1. Nosetip shape change testing in a regime predicted to pro-
    duce irregular shapes

2. Testing to obtain data on the effects of nose radius and
    material on transition.

The test series included exposure of 16 models during six arc runs plus
exposure of one additional model during a subsequent test series. The
test operations were generally smooth and data acquisition goals were met
although minor problems in model design were discovered. Details of
the test plan and data are documented in References 2-1 and Volume XII
of this series of PANT reports, respectively. Section 2.1 gives a brief
description of the testing, and Section 2.2 discusses the nosetip re-
sponse results.

2.1 TEST SUMMARY

Irregular nosetip shapes have been observed in numerous PANT wind
tunnel tests of low temperature ablator models (see, for example, Refer-
ences 2-2, 2-3, or Volume XIV). The formation of these undesirable shapes
appears to require at least the following two conditions:

*   Boundary layer transition should occur forward of the sonic
    point on the nosetip

*   The flow field Mach number must be high enough to produce a
    strong curved shock which can influence heat and mass transfer
    rates and nosetip shape change.

As a result of the emphasis in most hyperthermal materials tests on maxi-
mizing impact pressure, flow field Mach number is generally near one, and
the second requirement is rarely met. Thus, development of irregular

shapes has not been seen on ground tests of graphitic materials. Based on analyses presented in Reference 2-4, it was determined that testing in the RENT facility using the 0.9-inch throat/2.39-inch exit diameter contoured nozzle would be, at most, marginally capable of producing the conditions likely to form irregular shapes.

The other purpose of the testing was to provide additional data on material and nose radius effects on transition in a hyperthermal environment. The PANT transition correlation (Reference 2-5) was developed principally based on wind tunnel testing, and its application to hyperthermal environments had been examined only for graphite nosetips with 0.25-inch nose radii (Reference 2-6). This test series was designed to supply pertinent data on transition for carbon phenolic, carbon/carbon, and graphite materials over a range of nose radii. The materials were chosen to provide a variation of surface roughness characteristics. For transition tests of the smaller models, higher stagnation pressure conditions were necessary. Thus, two of the arc runs were performed using the 0.9-inch throat/1.49-inch exit diameter nozzle.

The test matrix as actually run is shown in Table 2-1 although data from the subsequent testing (RTN 52-10) are not included. Runs 4, 5, and 7 were directed towards the shape change objective. Runs 6, 8, and 9 primarily provided transition information. All models except three had spherical nose radii on either a cylinder or an 8° aft cone. Nose radii varied from 0.2 to 0.75 inch. Two models were 30°/8° sharp biconics, and one model was a flat-ended, 0.3-inch radius cylinder.

In all runs the bulk enthalpy was lower than originally anticipated due to arc heater modifications implemented just prior to testing. These modifications improved cooling and reduced erosion of the front electrode. The first model (ATJ-S) tested failed catastrophically at 9 seconds into the run. Evaluation of the model design indicated that epoxy adhesive used to mate the ATJ-S nosetip to the silica phenolic skirt probably volatilized and fractured the graphite. The testing sequence was reordered while vent holes were drilled in the remaining graphite models of the same design and while Southern Research Institute fabricated a solid graphite backup model (RTN 52-007, Sting 3). All other aspects of testing were successful.

2.2   NOSETIP RESPONSE RESULTS

The results of the shape change tests (Runs 4, 5, and 7) provide detailed large scale information on shape behavior in realistic

2-2

TABLE 2-1

PANT ARC JET TEST MATRIX

RTM-52- ①	NOZZLE D*/Dₑ	P_c (psig)	P_{t_2} ② (atm)	H_B (Btu/lbm)	est H_t ③ (Btu/lbm)	MODEL OR START NO.					PRIMARY PURPOSE
						1	2	3	4	5	
004	0.5"/2.39"	1674.	25.	1754.	2190.	ATJ-S $R_N=.625"/8°$ brake at 9 sec	CP $R_N=.625"/8°$ 25 sec	$\theta_o=.75"$ $R_N=20$ in/sec	$P_o=.75"$ $R_N=20$ in/sec	$\theta_{stag}=.25"$ $R_N=20$ in/sec	Shape Change
005	0.5"/2.39"	1050.	16.	1924.	2100.	CP $R_N=.625"/8°$	CP 30°/8°Biconic 25 sec	—			Shape Change
006	0.5"/2.39"	900.	14.	1853.	1960.	CP $R_N=.5"/cyl$ 15 sec	CP $R_N=.25"/cyl$ 10 sec	MOD-III $R_N=.75"/cyl$ 15 sec			Transition
007	0.5"/2.39"	1665.	25.	1678.	2350.	ATJ-S $R_N=.625"/8°$ 25 sec	ATJ-S 30°/8°Biconic 25 sec	ATJ-S (Solid) $R_N=.625"/8°$ 20 sec			Shape Change
008	0.5"/1.49"	1077.	35.	1923.	2100.	ATJ-S $R_N=.2"/cyl$ 4 sec	ATJ-S $R_N=.4"/cyl$ 4 sec	MOD-III $R_N=.2"/cyl$ 4 sec	$P_o=.5"$ $R_N=20$ in/sec	$\theta_{stag}=.25"$ $R_N=20$ in/sec	Transition
009	0.5"/1.49"	982.	32.	2014.	2160.	Flat, $R_{cyl}=.3"$ 4 sec	ATJ-S $R_N=.3"/cyl$ 4 sec	MOD-III $R_N=.3"/cyl$ 4 sec			Transition

NOTES:
① RTM-S2-001 through 003 were check-out runs; no ablation data but provided calibration data.
② P_{t_2}/P_c derived from pressure calibration data.
③ All tests run at flat enthalpy profile for uniformity and maximum H_B; H_t/H_B estimated from calibration data.

environments for carbon phenolic and graphite. The model behavior was generally indicative of fully turbulent conditions without major asymmetries or irregular shapes. This was particularly true of the carbon phenolic models which, despite attempts to produce transitional flow, always exhibited well-behaved fully turbulent shapes. With the ATJ-S models, small protrusions or knobs developed at the stagnation point and in fact appeared quite similar to previous low temperature ablator shape profiles as illustrated in Figure 2-1. The figure compares an ATJ-S model with a camphor model tested at $Re_\infty = 5.10^6/ft$ and $M_\infty = 5$ in the NOL hypersonic wind Tunnel Number 8.

(a)   Run 007, Sting 2 — Graphite   (b)   PANT Run 204 — Camphor
                                                low temperature ablator
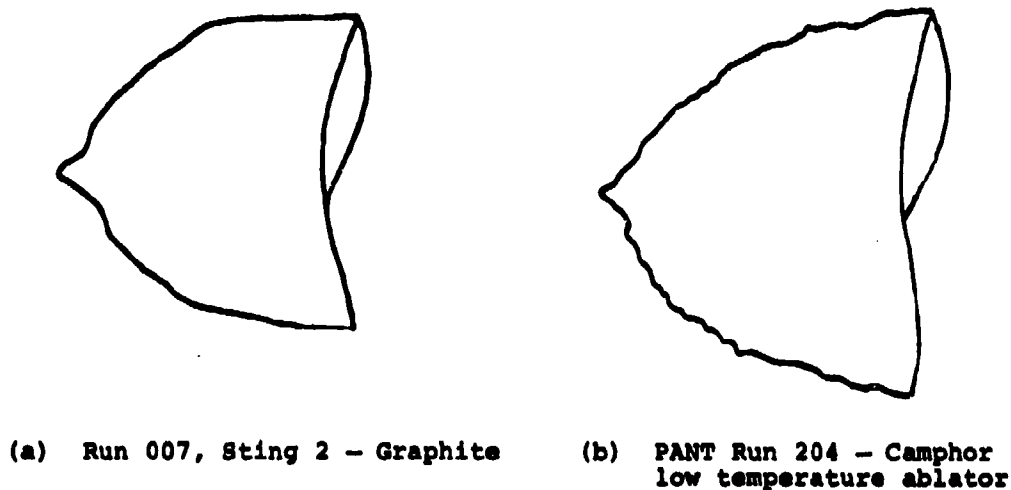
Figure 2-1.   Comparison of Nosetip Shape Profiles

Both the ATJ-S and the carbon phenolic sphere/cylinder models exhibited two distinct recession regimes. After transition occurred at about the sonic point, the shapes proceeded to sharpen to a conic configuration without substantial stagnation point recession. After achieving the sharpened shape, recession increased substantially and the shape remained relatively uniform. The presharpened (30°) configurations for both materials began to recede immediately without having to sharpen thus achieving substantially greater total recession in a shorter time.

The transition tests (Runs 6, 8, and 9) produced satisfactory results except for the two carbon phenolic models. The carbon phenolic at the low impact pressure appeared to develop a significant char layer and then delaminate. The carbon phenolic models transitioned close to the

2-4

stagnation point, but the shape change and roughness were dominated by the delamination characteristics rather than the fluid mechanics.

The remaining models all presented useful information on size, shape, and material properties effects on transition. All models tested in the small (1.49 inch) nozzle with the exception of the flat faced ATJ-S model exhibited immediate transition which seemed to remain for a long time in an "intermediate shape" pattern consisting of a laminar region extending up to about the sonic point and then an obviously turbulent region with a fine scale scallop pattern. This shape slowly sharpens to a configuration which is similar to low temperature ablation nosetips, as illustrated in Figure 2-2.

(a) Run 008, Sting 2 — Graphite   (b) PANT Run 216 — Camphor
                                             low temperature ablator
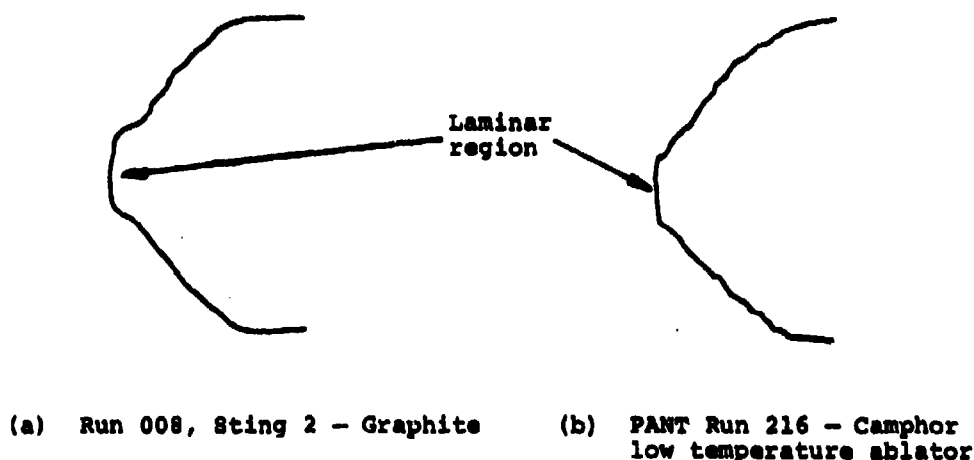
Figure 2-2. Comparison of Transitional Shapes

The large (0.75 inch nose radius) Mod-III model on Sting 3 of Run 006 appeared to be transitional at completion of testing. Large gouges were evident starting at about the 45° location around the nose. Thus, this large nose radius Mod-III appeared to be experiencing incipient transition even at this low pressure (p_{t_2} = 12 atm) test condition.

The flat faced ATJ-S model on Sting 1 of Run 009 appeared to maintain a laminar boundary layer through most of its exposure. This model experienced very little recession. In particular, during the four seconds of exposure, this model did not even ablate to a rounded blunt "laminar" shape as might be expected. It is uncertain whether or not the irregular ablation at the corners of this model near the end of the exposure is indicative of transition.

As indicated above, the shape change responses of the nosetip models tested in this 50 MW arc test series are, in general, consistent with response trends observed in low temperature ablator experiments. It is unfortunate that the formation of extremely irregular (slender or asymmetric) nosetip shapes was not observed. The lower-than-anticipated enthalpy levels achieved in these arc tests undoubtedly contributed to missing the irregular shape regime in these tests.

Although the transition data are adequate to yield useful quantitative information on transition of real materials, these data have yet to be analyzed. Comparison between transition in these contoured nozzle tests with transition observed in ramped-environment, flared nozzle tests would provide an indication of flow effects on boundary layer transition.

SECTION 2 REFERENCES

2-1. Powars, C. A., "Test Plan: PANT Program Nosetip Transition and Shape Change Tests in the AFFDL 50 MW RENT Arc," Aerotherm Division, Acurex Corporation, Mountain View, California, Aerotherm Report TM-73-36, C/N 7040-298, October 1973.

2-2. Derbidge, T. C. Wool, M. R., and Baker, D. L., "Passive Nosetip Technology (PANT), Interim Report, Volume IV — Definition of Shape Change Phenomenology from Low Temperature Ablator Experiments, Part II — Experimental Data, Series D," SAMSO-TR-74-86, Aerotherm Report 74-90, Aerotherm Division, Acurex Corporation, January 1974.

2-3. Baker, D. L., Wool, M. R., Powars, C. A., and Derbidge, T. C., "Passive Nosetip Technology (PANT), Interim Report, Volume V — Definition of Shape Change from Low Temperature Ablator Experiments, Part I — Experimental Data, Series C," SAMSO-TR-74-86, Aerotherm Report 74-90, Aerotherm Division, Acurex Corporation, January 1974.

2-4. Shimizu, A. B., "The Feasibility of Studying the Development of Irregular Ablated Shapes in the 50 MW Arc," TM-73-37, Aerotherm Division, Acurex Corporation, October 1973.

2-5. Anderson, A. D., "Passive Nosetip Technology (PANT), Interim Report, Volume III — Surface Roughness Effects, Part III — Boundary Layer Transition Data Correlation and Analysis," SAMSO-TR-74-86, Aerotherm Report 74-90, Aerotherm Division, Acurex Corporation, January 1974.

2-6. Ferrell, J. E. and Powars, C. A., "Preliminary Correlations of Transition Data from Ablation Profiles," Aerotherm Report TM-73-38, November 1973.

SECTION 3

SCALLOP EFFECTS ON HEAT TRANSFER

One of the important results of the initial efforts conducted under the PANT program was the discovery that surface scallops significantly increase graphite recession rate above smooth wall predicted values (Reference 3-1). In fact graphite ablation data from such diverse test facilities as the AFFDL 50 MW arc heater and the AEDC Range G ballistic range are consistently predicted only if proper account of scallop effects on heat transfer are included.

Low temperature ablator (LTA) wind tunnel test models conducted under the PANT program experienced the formation of scallops which are geometrically similar to those which form on graphite. An apparent increase in recession rate was also observed in the LTA tests. Based on these results a task was defined to accomplish the following objectives:

- Measure scallop dimensions on LTA models.

- Quantitatively infer the heating rate to a scalloped LTA surface.

- Measure the heating rate to a calorimeter replica of the scalloped LTA surface (Series H test series).

LTA models were used for these measurements as opposed to graphite models for the following reasons:

- LTA models were tested at hypersonic conditions ($M_\infty = 5$) which is a much better flight simulation than most graphite ground tests ($M_\infty = 1.7$) (anticipated to influence cone scallops).

- LTA scallop sizes are larger and, hence, can be more accurately measured.

- LTA thermochemistry is simple (sublimation – no chemical reactions) and well defined. This aids in inferring heating rate.

- Test conditions are more well defined (wind tunnel versus arc heater).

3-1

- LTA models are larger than typical graphite models (2.5 versus 0.25 inch nose radius). This simplifies the construction of the replica calorimeter.

In order to satisfy the stated objectives within the scope of the program a single LTA model was selected for the majority of the detailed measurements and tests. The model was selected based on its compatibility with the task objectives and involved consideration of

- Model symmetry
- Shape stability
- Variability of recession rate
- Ability to duplicate LTA test condition for a calorimeter replica

Based on these considerations PANT Series D LTA Run 201 (Reference 3-2) was selected. The results of the roughness measurements and tests are discussed in the following sections. Section 3.1 describes measurements of scallop roughness and inferred heat transfer rate. Section 3.2 presents results from the scallop replica calorimeter tests. Comparisons between inferred, scallop calorimeter, and other rough wall calorimeter data are covered in Section 3.3.

3.1 MEASUREMENTS FROM LTA TESTS

Two types of measurements were made from the LTA test data: (a) scallop roughness, and (b) inferred heat transfer rate. These are discussed in the following two sections.

3.1.1 Scallop Roughness Measurements

Measurements of scallop roughness were taken from post test replicas of LTA models for the following reasons:

- To relate scallop roughness heating augmentation to sandgrain type augmentation
- To observe scallop roughness trends with test condition

Figure 3-1 shows photographs of a turbulent ablating LTA surface from the PANT Series D tests and illustrates the irregular character of scallops. Close examination of replicas of scalloped surfaces shows that even at a constant streamwise location there is considerable variation from one scallop to the next. Because of this basic variability in scallop size, conclusions about typical scallop roughness must be drawn

3-2
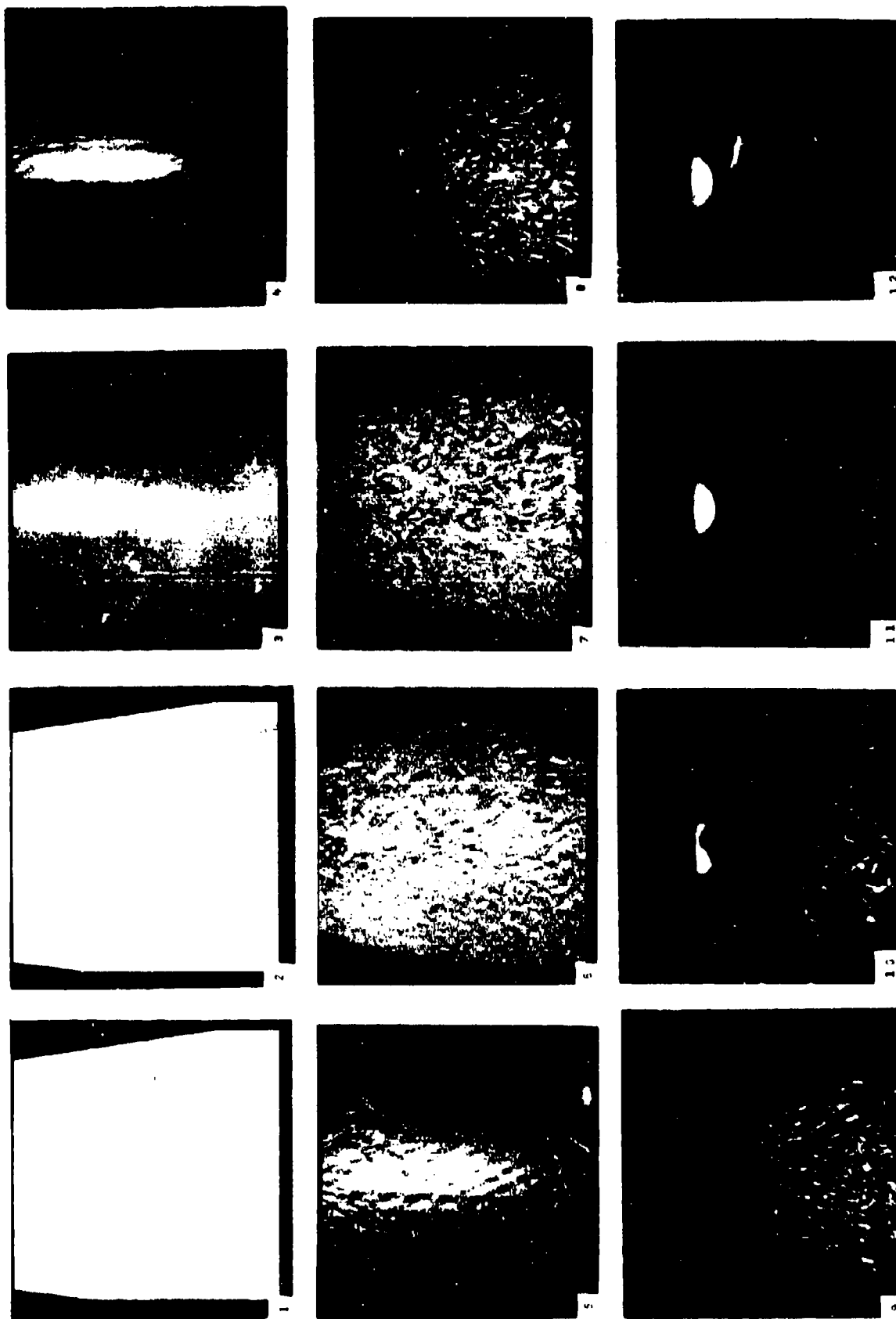
Figure 3-1. Closeup Photography of a Typical Scalloped Surface
(Run No. 207, $Re_\infty = 10.16 \times 10^6/ft$)

from a statistically significant data base. In order to establish such
a data base for each model the model was divided into two regions, as
follows:

- The high angle subsonic/transonic nose region

- The low angle supersonic cone region

The two types of scallop measurements are discussed in the following
paragraphs.

Nose Region Scallops

Scallops in the nose region are much smaller than cone scallops
and, hence, greater care must be taken in their measurement. The tech-
nique used was to section plaster cast replicas of the model. These
replicas were made from RTV molds produced directly after each LTA test
and provide an accurate record of surface details. The plaster sections
were then enlarged 10X on an optical comparator, and profile traces of
the scalloped surface were made. A datum surface was defined for each
profile, and roughness heights were measured. Figure 3-2 presents a
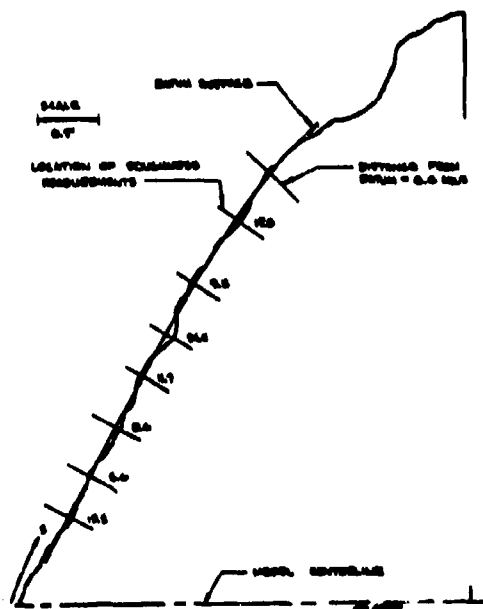
Figure 3-2. Typical Nose Region Profile Trace (Run 201)

3-4

typical profile trace and roughness measurements. In the nose region, only longitudinal (i.e., parallel to the model centerline) cuts were made. This is because cuts in the lateral direction (i.e., perpendicular to the centerline) intersect the surface at a significant angle (approximately 45°) and, hence, in order to determine normal roughness height from the profile trace a correction must be made. Unfortunately, the amount of the correction is a function of both the surface intersection angle and the roughness geometry. Also, the correction becomes increasingly larger as the surface intersection angle is increased.

Nose region scallop measurements were only made for the baseline case, Run 201. Four longitudinal cuts were made. The roughness measurements from all longitudinal cuts were considered together when calculating the mean and standard deviation. Table 3-1 presents these results.

TABLE 3-1

NOSE REGION SCALLOP ROUGHNESS MEASUREMENTS,
RUN 201

| Number of Measurements	Mean Peak to Valley Roughness (mils)	Standard Deviation (mils)
31	27.3	11.5

These roughnesses will be used later when comparing scallop and sand-grain roughness augmentation to heat transfer.

Cone Region Scallops

The cone region was defined as that region aft of where the surface angle is less than 20°. The technique used to measure scallops was basically the same as that used on the nose except that the scallops on the cone are large enough that the profile traces can be made directly from the plaster sections; no magnification is necessary. In addition, lateral cuts of the cone surface can be used for scallop measurements because the intersection angle correction is small. Figures 3-3a and 3-3b show typical longitudinal and lateral cone profile traces and scallop measurements.

Cone scallop measurements were made on four models covering a range of parameters. Table 3-2 presents the range of conditions considered. For each model a minimum of four longitudinal and three lateral profile cuts were considered. The mean scallop dimension measurement was
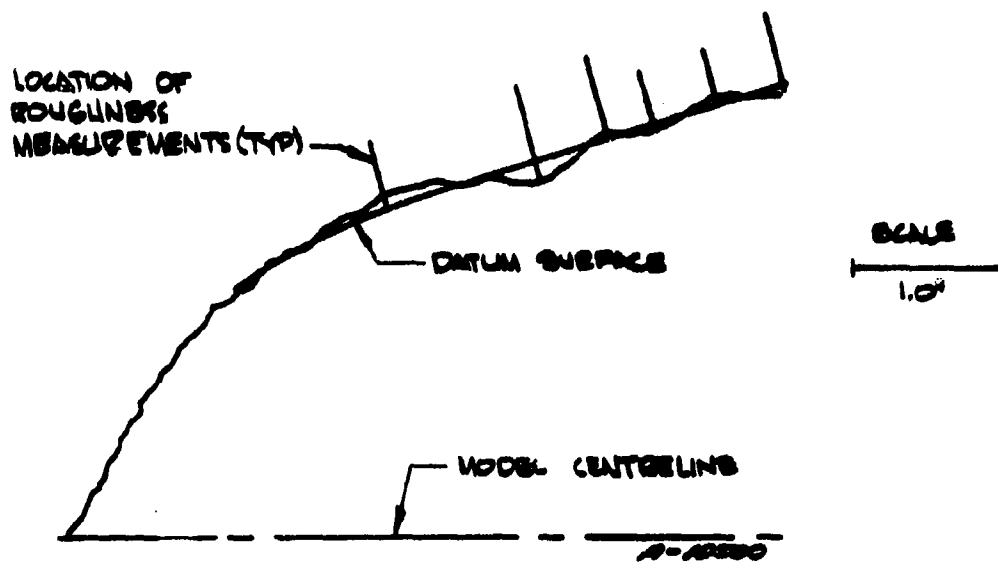
a.) LONGITUDINAL PROFILE TRACE (RUN 201)
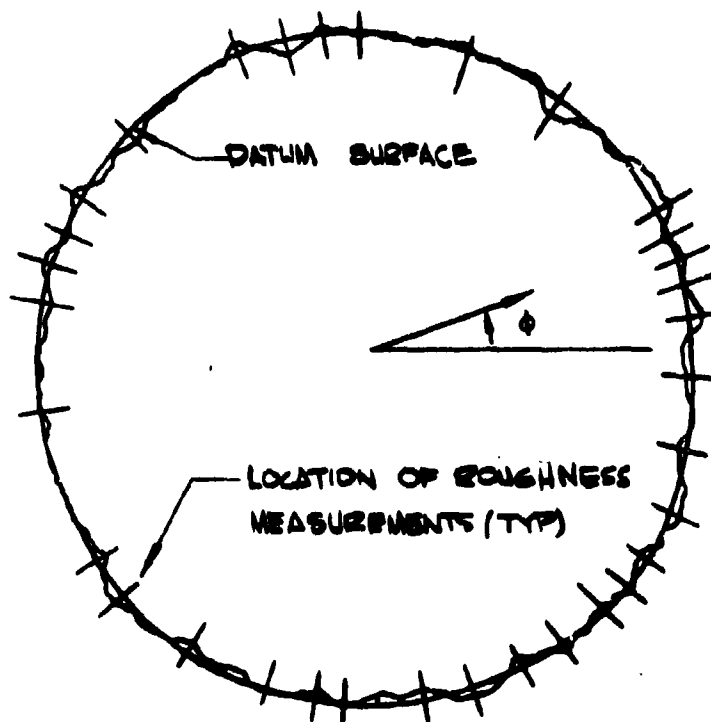
b.) LATERAL PROFILE TRACE (RUN 201, $Z = 7.06$ IN.)

Figure 3-3. Typical Cone Region Profile Traces

TABLE 3-2

CONE REGION SCALLOP MEASUREMENT MATRIX

Run* No.	Test Conditions				Nose Radius (in.)	Description
	P_O (psia)	T_O (°F)	M_∞	Re_∞ $(10^6/ft)$		
201	480	585	5	10.02	2.5	Baseline model
203	775	975		10.15	2.5	Effect of varying pressure at constant Reynolds number
204	395	975		5.23	2.5	Effect of Reynolds number
207	786	989		10.16	1.5	Effect of nose radius

*All tests were performed on PANT test Series D.

calculated by lumping all longitudinal and lateral cut data. These results are displayed in Figure 3-4 which shows a comparison of the longitudinal and lateral cut measurements; also, a net mean calculation using both longitudinal and lateral measurements is shown. The comparison between the longitudinal and lateral measurements is reasonable considering the basic variability in scallop sizes. Figure 3-4 demonstrates the validity of the assumption that the scallops on the cone form a single statistical group.

As an indication of the variation of cone scallop depth with test condition, Figure 3-5 shows the mean scallop dimensions plotted versus two test parameters. Figure 3-5a shows a plot of mean peak to valley scallop dimension versus tunnel supply pressure. Scallop analysis reported in Reference 3-3 indicates that if surface deformation is a predominant mechanism in scallop formation that cone scallop depth should vary as cone pressure. For comparison, a plot of scallop depth versus free stream unit Reynolds number is shown in Figure 3-5b. Although more data are needed to be conclusive, these two plots seem to indicate that scallop depths correlate better with Reynolds number than pressure.

3.1.2 Inferred Heating Data

In this program, a method was developed for inferring the heating rate to an ablating camphor surface. Basically, the technique involves combining measurements of surface recession rate with material
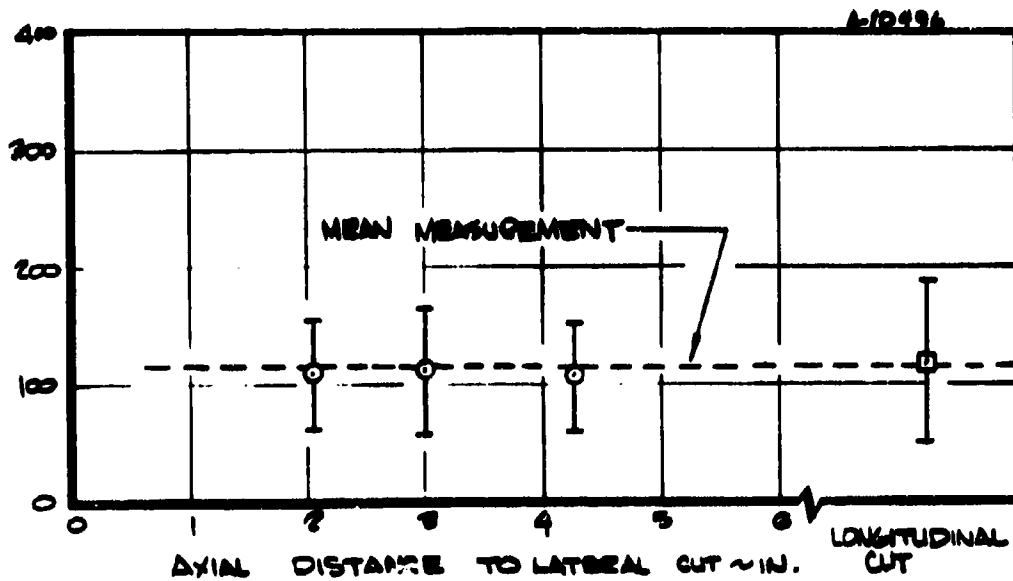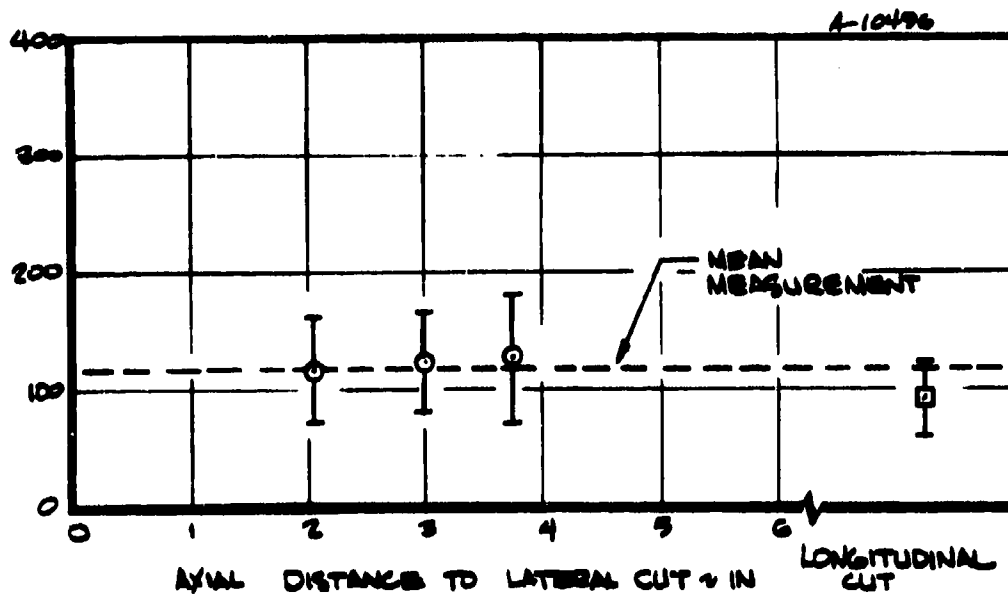
Figure 3-4. Comparison of Longitudinal and Lateral Cut
Scallop Measurements
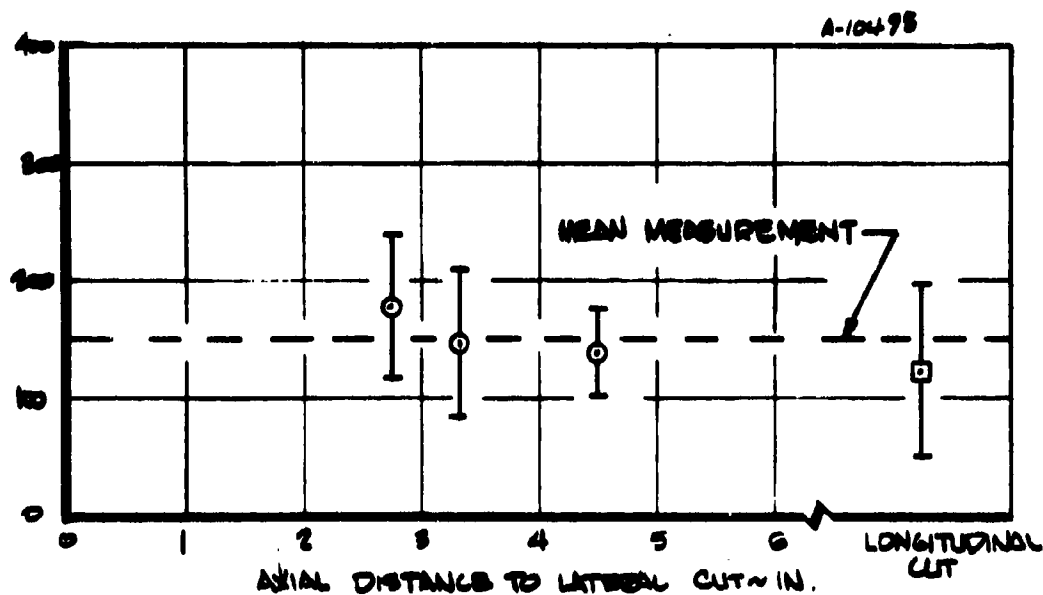
c) RUN 804
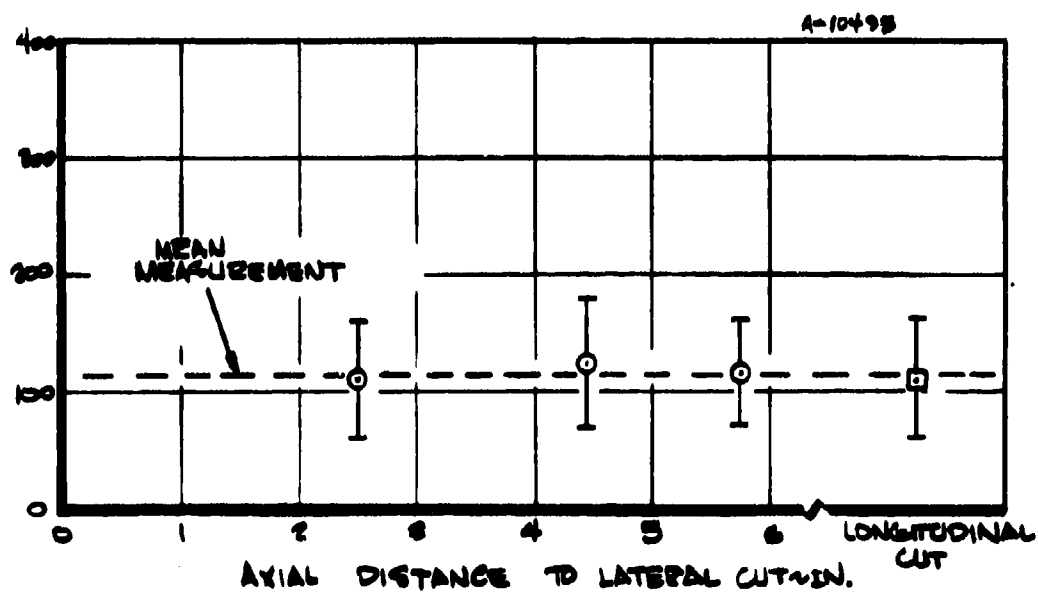
D) RUN 807

Figure 3-4. (Concluded)
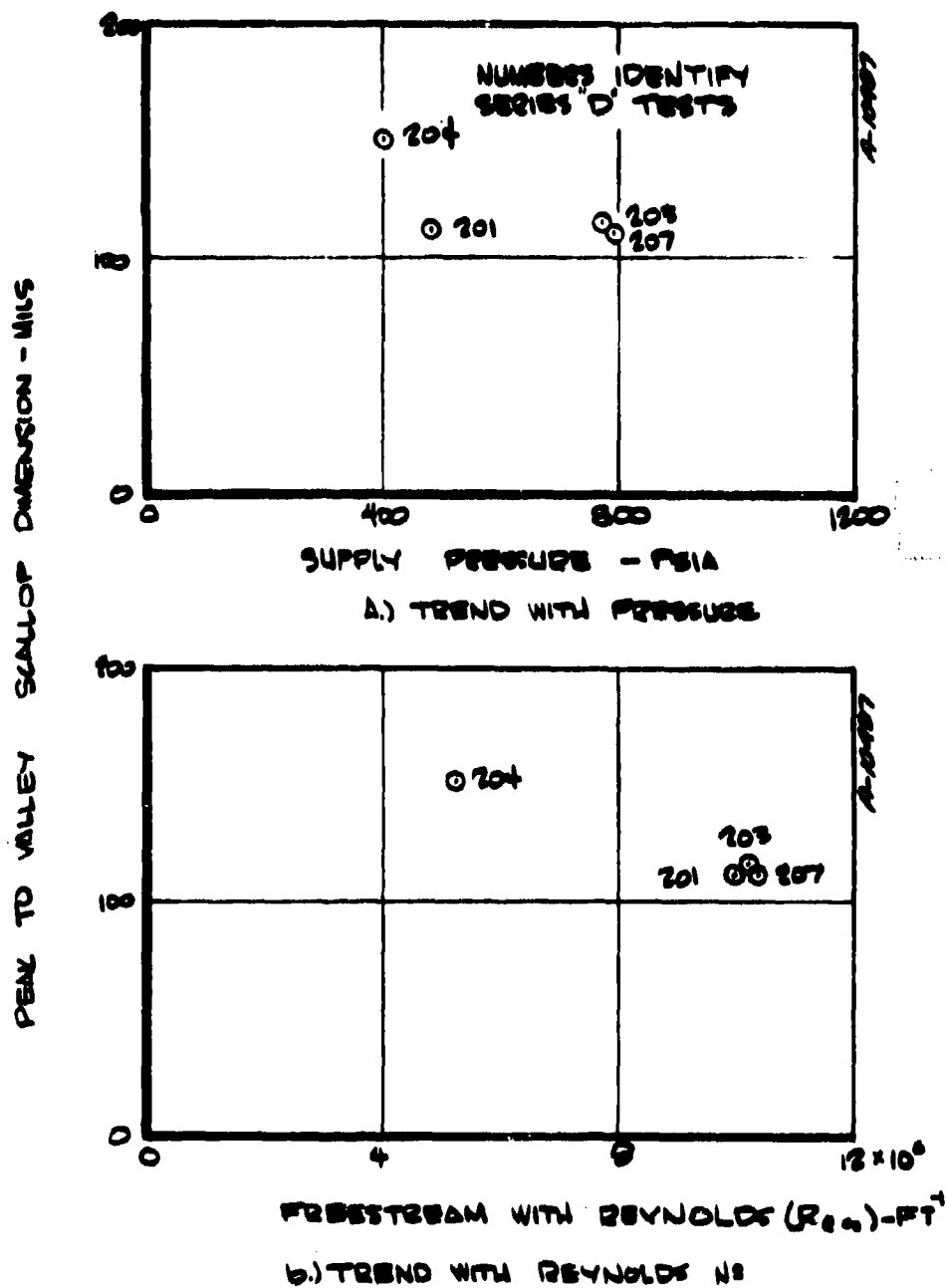
Figure 3-5. Variation of Peak to Valley Scallop Dimension
With Test Condition

thermochemistry and calculated edge conditions to infer the heating rate required to match the observed recession rate. It should be emphasized that, for camphor, recession rate is directly proportional to heating and, therefore, the accuracy of the inferred heating is proportional to the accuracy of the measured recession rate.

Inferred heating rate values were determined for the baseline test (Run 201). These heating rates are shown in Figure 3-6. The uncertainty band shown for the inferred heating is due primarily to uncertainty in the measurement of normal surface recession rate. The uncertainty in normal recession rate is, in turn, due to uncertainty in both surface angle measurement and recession rate component (either axial or radial). This inferred heating distribution is compared with calorimeter data and heating predictions in Section 3.3.
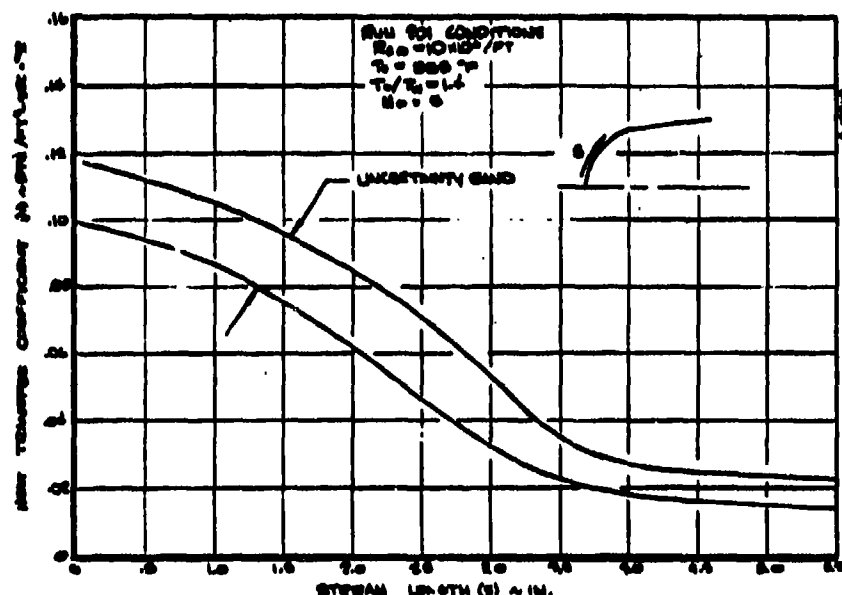
Figure 3-6. Inferred Distribution of Nonblown Heat Transfer Coefficient for the Final Shape of Run 201

3.2   SCALLOP CALORIMETER TESTS (SERIES H)

A metal calorimeter replica of the final ablated shape of the baseline test (Run 201) was constructed and tested in the Naval Ordnance Laboratory (NOL) No. 8 wind tunnel on February 26, 1974. The objectives of these tests were to:

1. Generate heat transfer data for a calorimeter replica of an ablated LTA scallop roughened surface for comparison with heat transfer data inferred from the recession rate of the LTA model.

3-11

2. Generate heat transfer data for a scallop calorimeter model over a range of Reynolds numbers for comparison with prediction techniques, and other rough wall heating data.

It was felt that if the calorimeter results compared favorably with the inferred heat transfer results, then other camphor nosetip ablation data could be used to generate additional scallop effects data for a wide range of test conditions and nosetip shapes.

The calorimeter model and test approach are described briefly in Section 3.2.1 and the test results are covered in Section 3.2.2.

3.2.1 Calorimeter Model and Test Approach

The purpose of the calorimeter model is to measure convective heat flux to a surface which is a replica of an ablated LTA surface. The determination of heat flux is based on the measurement of the temperature history of an isolated thermal capacitance element. Heat flux is determined from this temperature history by application of the law of conservation of energy.

The calorimeter model is a replica of the final ablated shape of Run 201 (PANT, Series D). A complete description of the calorimeter is given in Volume XIII of this Interim Report. The configuration of the calorimeter model is shown in Figure 3-7. The thermal capacitance
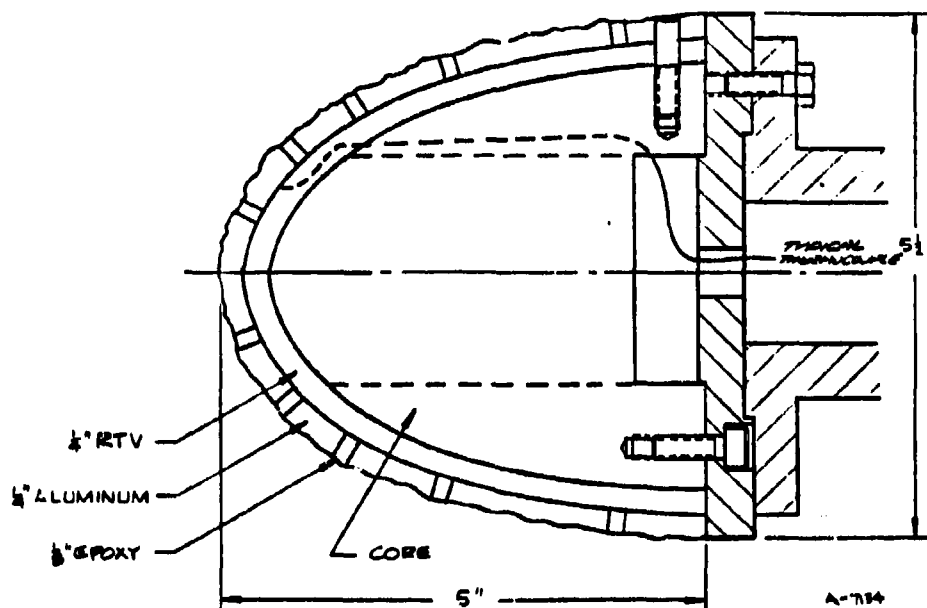
Figure 3-7. Calorimeter Model Configuration

elements are segments of an aluminum shell which was cast from the post-test replica of Run 201. The segments are supported and insulated from one another by a high temperature glass filled epoxy. For measurement of temperature history the aluminum segments are instrumented with a total of 18 thermocouples. Figure 3-8 indicates the thermocouple locations.
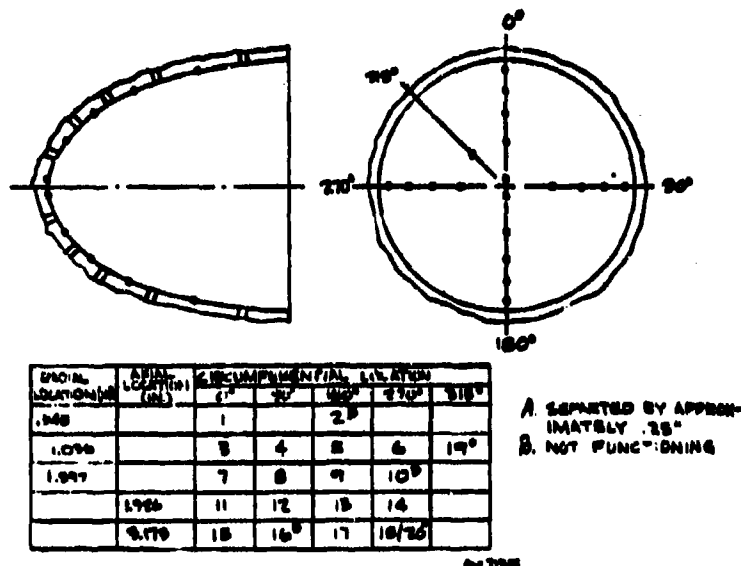
Figure 3-8. Definition of Thermocouple Locations

During testing, data from each thermocouple were sampled at least every 0.112 second. These data were then curve fit using a splined quadratic least squares technique to define the derivatives of temperature with time ($dT/d\theta$). When conduction losses from the isolated thermocapacitance elements are small the heat flux can be evaluated directly from the temperature derivative using the approximation

$$\dot{q}_{conv} = \frac{\rho C V}{A} \frac{dT}{d\theta} \qquad (3-1)$$

where

$\dot{q}_{conv}$ = convective heat flux, Btu/ft^{2}sec

ρ = material density, lbm/ft^3

C = material specific heat, Btu/lbm°R

V = segment volume, ft^3

3-13

A = segment projected area, ft^2

dT/dθ = derivative of temperature with time, °R/sec

Analysis presented in Volume XIII indicate that Equation (3-1) is sufficiently accurate (error is less than 10 percent) if applied to times less than 1.0 second.

3.2.2 Test Results

A series of seven tests designated Test Series H were performed with the replica calorimeter. The test conditions are given in Table 3-3.

TABLE 3-3

TEST CONDITIONS FOR PANT SERIES H WIND
TUNNEL TESTS — FEBRUARY 1974[a]

Run[b] No.	Air Supply		Free Stream		Exposure Time (sec)
	P_o (psia)	T_o (°F)	M_∞	Re_∞ (10^6/ft)	
501	85	392	4.95	2.61	45.7
502	370	384	4.99	10.93	14.1
503	170	375	4.97	5.16	18.5
504	258	379	4.98	7.74	15.3
505	369	345	4.99	11.76	13.7
506	675	352	5.00	21.15	12.1
507	503	350	5.00	15.78	12.0

[a]A single calorimeter was tested which was a replica of PANT, Series D, low temperature ablator, Run 201, final shape.

[b]All runs at zero angle of attack.

During each test, shadowgraph photographs were taken to define the bow shock shape and determine whether flow anomalies were occurring. One of two types of photographs were taken, either a close-up or an overview, a sample of each type is shown in Figure 3-9.

Run 502 represents the most comparable test conditions between the calorimeter and the LTA test from which the calorimeter was constructed. Measured early time (θ = 1.0 second) heat flux levels for Run 502 are shown as a function of stream length in Figure 3-10. Certain thermo-couples had consistently suspicious response and these thermocouples
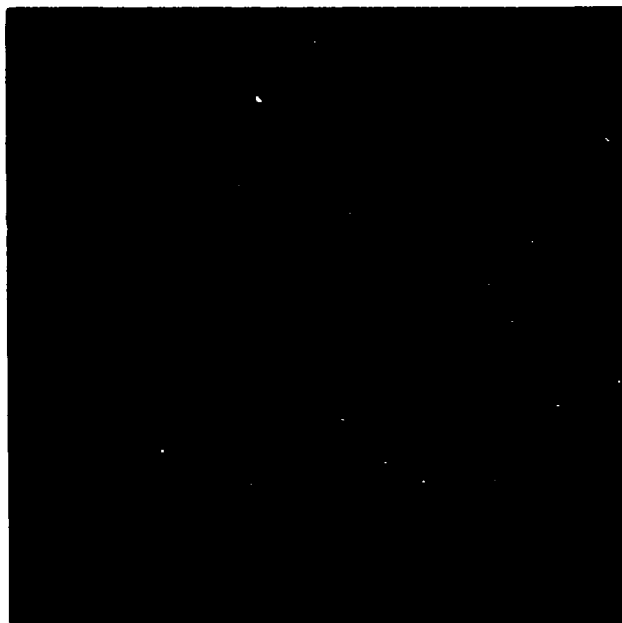
a. Overview, Run 507

b. Close-up, Run 502

Figure 3-9. Sample Shadowgraph Photographs
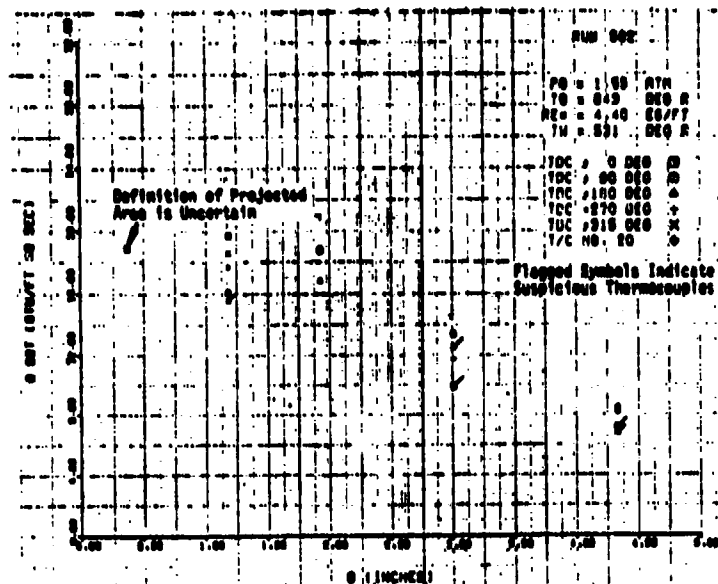
Figure 3-10. Measured Heat Flux Levels for Run 502
(Re$_\infty$ = 10.93 x 10^6/ft)

are shown with flagged symbols. Also, the definition of the projected area used in Equation (3-1) for the stagnation region segment is uncertain and, therefore, the heat flux is also uncertain.

For purposes of comparison with other data the heat transfer coefficient is more applicable than the heat flux. The heat transfer coefficient was calculated from

$$h = \frac{\dot{q}_{conv}}{T_r - T_w} \qquad (3-2)$$

where

h = convective heat transfer coefficient

T_r = boundary layer edge recovery temperature

T_w = wall temperature

The recovery temperature (T_r) was calculated using the environmental routines in the PANT developed shape change code (Reference 3-4). Comparisons of measured heat transfer coefficient with other data and predictions are given in Section 3.3.

3-16

3.3 DATA COMPARISONS

Three sets of relevant rough wall heat transfer data are comparable:

- Heat transfer rates inferred from the measured recession rate for Run 201

- Heat transfer data measured from the scallop replica calorimeter model (Series H)

- Heat transfer data measured for sandgrain roughened calorimeter models (Series A)

A comparison of the inferred heat transfer rates and scallop replica data is given in Section 3.3.1. Comparisons of the scallop calorimeter data with the PANT correlation developed from the Series A sandgrain roughness calorimeter data are discussed in Section 3.3.2. Conclusions regarding these data comparisons are presented in Section 3.3.3.

3.3.1 Comparison of Inferred Heat Transfer Rates and Scallop Replica Data

Since the scallop replica model was constructed of materials which degrade at higher temperatures, all Series H tests were conducted at supply temperatures below 400°F. The comparable LTA model (Run 201) was, however, tested at a supply temperature of 585°F. In order to compare the inferred heating rates from the ablation test with the calorimeter data, the inferred heating was corrected to account for differences in supply temperature and pressure as described in Volume XIII. Figure 3-11 shows the adjusted inferred heating distribution and the comparable calorimeter data (Run 502, $Re_\infty = 10 \times 10^6 /ft$). The boxed areas around the calorimeter data indicate the spread in the data on a given ring and the stream length covered by each ring. Because the rings are insulated from one another the measured heat flux represents an average of the local heat flux over the ring. The data are in general agreement with inferred heat coefficients from the LTA data. The calorimeter data on the forecone (Rings, 2, 3, and 4) agree quite well with the inferred heat transfer but the aft cone data (Ring 5) is higher than the inferred.
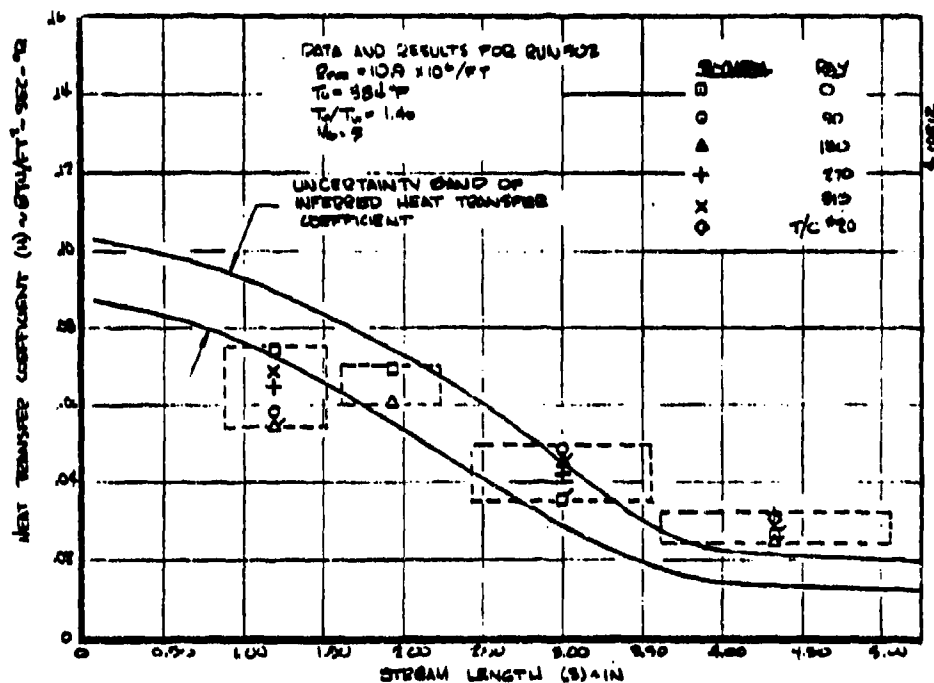
Figure 3-11. Comparison of Inferred and Measured Heat Transfer Coefficient
Distribution for the Baseline Reynolds Number Condition (Run 502)

Indeed, the mean of the calorimeter data increases relative to the mean
of the inferred values as a function of streamwise distance. It may be
speculated that this trend is associated with the accumulating effects
of ablation products on the boundary layer heat and mass transfer. For
the ablating case, mass addition to the boundary layer over the forecone
would reduce mass transfer (and, hence, inferred heat transfer) at aft
cone locations. No calculations were performed to assess this specula-
tion.

3.3.2 Comparison of Scallop Replica Data with Sandgrain Roughness Effects Data and Correlations

Under the PANT program extensive testing of sandgrain type
roughened calorimeters was performed (Series A tests — Reference 3-5).
The data from these tests was used to develop a rough wall heating corre-
lation applicable to sandgrain type surface roughness (Reference 3-6).
In this correlation the roughness heating augmentation factor

$$K_r = \frac{h_{rough}}{h_{smooth}} \qquad (3-3)$$

3-18

is correlated versus a parameter which is approximately proportional to the ratio of the roughness height to the laminar sublayer thickness

$$\frac{k}{\delta_{SL}} \propto Re_k \sqrt{C_{H_S}} \left(\frac{T_e}{T_w}\right)^{1.3} \qquad (3-4)$$

where

k = sandgrain roughness height

δ_{SL} = laminar sublayer thickness

$Re_k = \dfrac{\rho_e u_e k}{\mu_e}$ = boundary layer edge Reynolds number based on roughness height

C_{H_S} = smooth wall Stanton number

T_e = local boundary layer edge temperature

T_w = local wall temperature

A comparison of the Series H calorimeter data with the PANT rough wall heating correlation is shown in Figure 3-12. The value of K_r for each data point was calculated by dividing the measured heat transfer coefficient by the smooth wall, turbulent PANT code prediction. The error bands on each K_r represent the spread in the data. The abscissa is

$$Re_e \sqrt{C_{H_S}} \left(\frac{T_e}{T_w}\right)^{1.3} \; mil^{-1} \qquad (3-5)$$

where

$Re_e = \dfrac{\rho_e u_e}{\mu_e}$

Therefore, the PANT correlation appears as a series of parallel lines, one for each roughness height. The value of the abscissa parameter for each data point was taken from the smooth wall predictions. Different symbols are shown for each wind tunnel run. The figure indicates that K_r is roughly 1.3 on the forecone ring (Ring 2), increases to 1.6 on Rings 3 and 4, and further increases to approximately 2.0 on Ring 5. This observation is consistent with the fact that scallop dimensions are greater on the aft cone than on the forecone. The point of interest is that the heating increase factor on each ring is not sensitive to the test Reynolds number. The measured heating rates scale closely with changes in smooth wall turbulent heating. This demonstrates that the

a. Ring 2 (S = 1.2 in.)

b. Ring 3 (S = 1.9 in.)
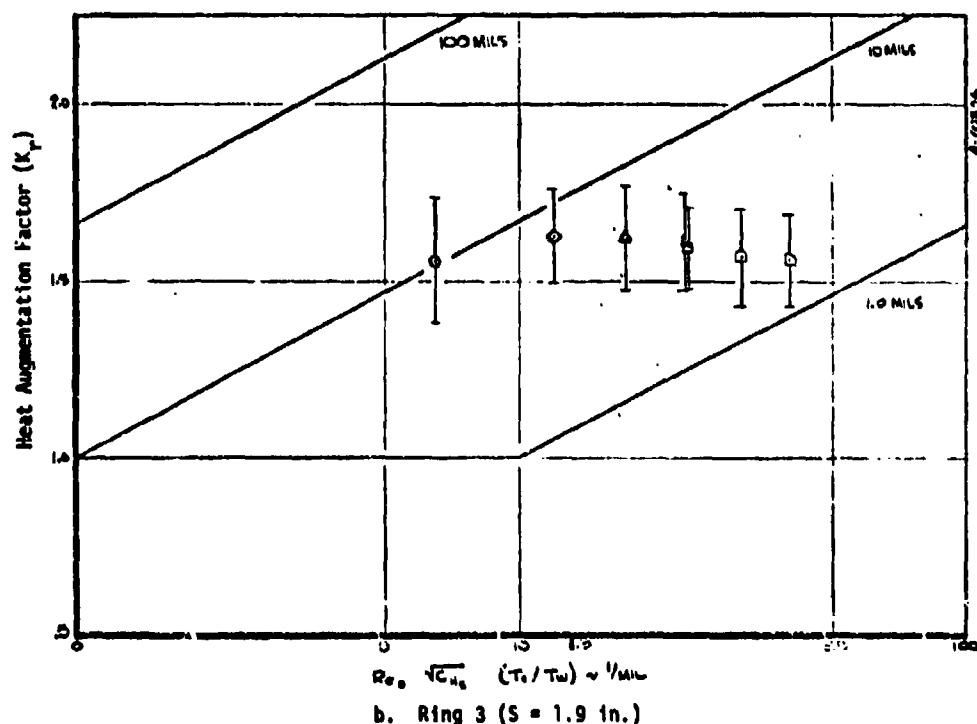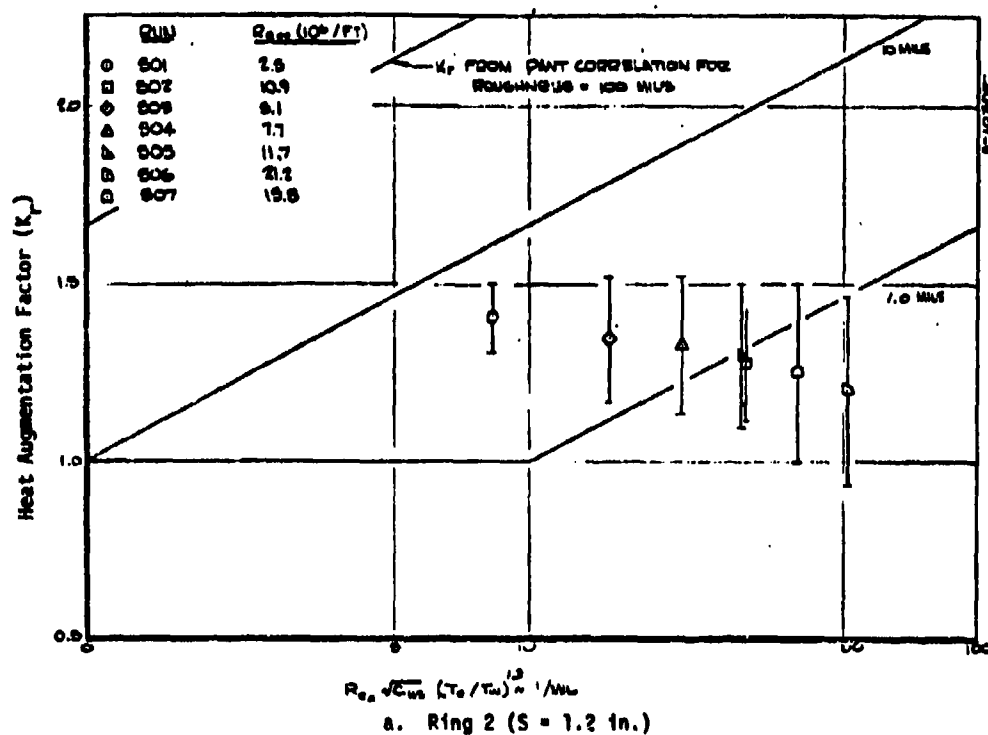
Figure 3-12. Comparison of the Series H Calorimeter Data
with the PANT Rough-Wall Heating Correlation

3-20
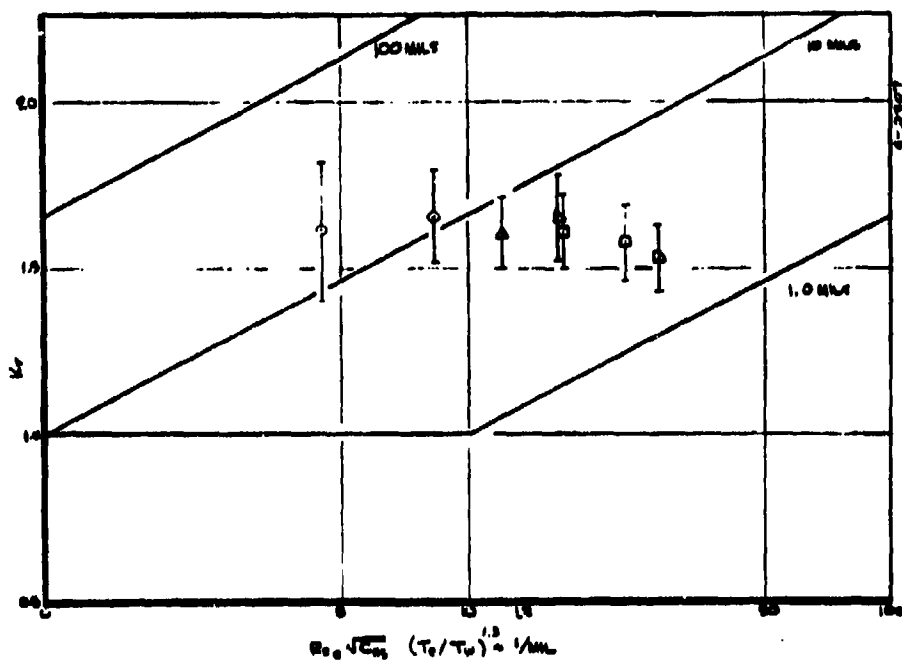
c. Ring 4 (S = 3.0 in.)
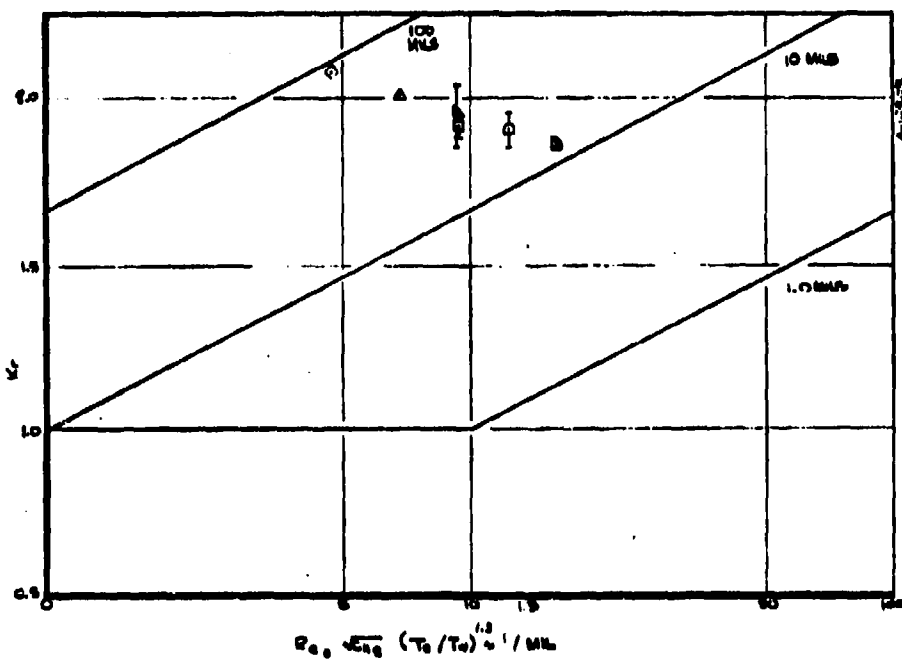
d. Ring 5 (S = 4.3 in.)

Figure 3-12. (Concluded)

3-21

scallops affect heat transfer in a different way than do sandgrain rough-
ness elements and tends to confirm the speculation stated in Reference
3-6 that the PANT roughness effects correlation is not directly applic-
able to scalloped surfaces. Indeed, since scallops form as a result of
flow/material ablation interactions, it would not be expected that a
correlation of sandgrain heating data would also correlate scallop heat-
ing data.

Since the augmentation is insensitive to Reynolds number condition,
one might conjecture that scallops affect heating mainly through changes
in the inviscid flow rather than through changes in the boundary layer.
The shadowgraphs shown in Figure 3-9 confirm that significant surface/
shock layer interactions did occur in the calorimeter tests. Similar
interactions were observed in shadowgraphs from the Series D and Series
I-LTA tests.

Another interesting point is that the scallop surface produces
less heating augmentation than a sandgrain surface having a similar
roughness height tested at the same Reynolds number condition. This
point is illustrated in Figure 3-13 where the sonic point augmentation
factor from the scallop calorimeter (Ring 2) is compared to correspond-
ing data from the Series A, 40 mil, sandgrain-type roughness calorimeter
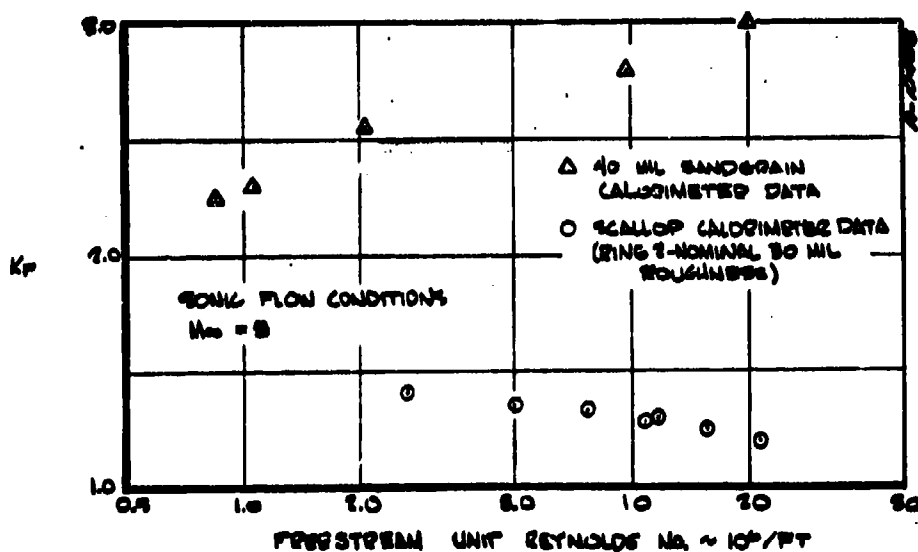
Figure 3-13. Comparison of the Scallop Calorimeter Data
With Sandgrain Type Calorimeter Data

3-22

model. The roughness measurements shown in Section 3.1.1 indicate a nominal roughness height of about 30 mils for the sonic region (i.e., forecone) of the scallop calorimeter. Although the roughness height is similar between the two models (30 mils versus 40 mils) the sandgrain heating factor is significantly higher than the comparable scallop calorimeter result. A technique described in Reference 3-7 to determine equivalent sandgrain roughness dimensions from scallop geometry data was investigated in an attempt to rationalize the differences shown in Figure 3-13. Although judicious specification of scallop geometry parameters can explain the relative values of heating factors, the different trends with Reynolds number condition could not be explained. To model the observed trend, the equivalent sandgrain would have to be a function of test condition.

3.3.3 Conclusions and Recommendations

3.3.3.1 Conclusions

The following conclusions are drawn from observation of the data and comparison with predictions.

- The heat transfer to the scalloped surface calorimeter was significantly greater than corresponding smooth wall predictions.

- The measured heat transfer rates agree generally with heating rates inferred from the corresponding LTA model; differences suggest possible effects of ablation on the inferred heat rates.

- The roughness augmentation factors (K_r) for each scallop calorimeter ring do not scale with the PANT sandgrain roughness effects correlation parameter

$$ Re_e \sqrt{C_{H_S}} \left(\frac{T_e}{T_w} \right)^{1.3} $$

- The roughness augmentation factor (K_r) distribution around the body is nearly independent of free stream Reynolds number, but K_r increases with increasing scallop roughness height.

- The scallop surface on the Series H calorimeter produces less heating augmentation than a sandgrain surface having a similar physical roughess height.

3-23

- The equivalent-sandgrain-roughness formulation of Reference 3-7 is not adequate to explain differences between sandgrain calorimeter and scallop calorimeter data.

3.3.3.2 Recommendations

The following recommendations result from the scallop studies performed under this program:

- Further assessment of the effects of upstream ablation on inferred heating rates should be performed to establish conclusively that LTA ablation data can be used to infer nosetip flow phenomena.

- Inferred heating rates should be derived from a large set of LTA test results to provide data for scallop effects studies.

- Correlations of scallop effects on heat transfer should be derived as functions of inviscid and/or viscous flow properties.

- The validity of the correlations derived from LTA wind tunnel data should be verified through comparisons to high pressure ablation data of actual nosetip materials

SECTION 3 REFERENCES

3-1. "Passive Nosetip Technology (PANT) Program, Interim Report, Volume II — Environmental and Material Response Procedures for Nosetip Design," SAMSO-TR-74-86, Aerotherm Report 74-90, Aerotherm Division, Acurex Corporation, January 1974. (SECRET)

3-2. Derbidge, T. C., Wool, M. R., and Baker, D. L., "Passive Nosetip Technology (PANT) Program, Interim Report, Volume V — Definition of Shape Change Phenomenology from Low Temperature Ablator Experiments, Part II — Experimental Data, Series D," SAMSO-TR-74-86, Aerotherm Report 74-90, Aerotherm Division, Acurex Corporation, January 1974.

3-3. White, C. O. and Grabow, R. M., "Influence of Scallop Roughness on Nosetip Shape Change Behavior," Final Technical Report, Nosetip Design Technology (NDT), SAMSO TR-73-88, Philco-Ford Corp. Aeronutronic Division, Newport Beach, California, January 1973.

3-4. Wool, M. R., Overly, P. T., and Derbidge, T. C., "Passive Nosetip Technology (PANT) Program, Interim Report, Volume VII — Computer User's Manual, Steady-State Analysis of Ablating Nosetips (SAANT) Program," SAMSO TR-74-86, Aerotherm Report 24-90, Aerotherm Division, Acurex Corporation, January 1974.

3-5. Jackson, M. D., Baker, D. L., and Powars, C. A., "Passive Nosetip Technology (PANT) Program, Interim Report, Volume III — Surface Roughness Effects, Part I — Experimental Data," SAMSO TR-74-86, Aerotherm Report 74-90, Aerotherm Division, Acurex Corporation, January 1974.

3-6. Powars, C. A., "Passive Nosetip Technology (PANT) Program, Interim Report, Volume III — Surface Roughness Effects, Part II — Roughness Augmented Heating Data Corrleation and Analysis," SAMSO TR-74-86, Aerotherm Report 74-90, Aerotherm Division, Acurex Corporation, January 1974. (Confidential)

3-7. Dirling, R. B., Jr., "A Method for Computing Rough Wall Heat Transfer Rates on Reentry Nosetips," AIAA Paper No. 73-763, presented at the AIAA Eighth Thermophysics Conference, Palm Springs, California, July 16-18, 1973.

SECTION 4

SERIES I WIND TUNNEL TESTS

The Series I Low-Temperature Ablator (LTA) wind tunnel tests were conducted in Tunnel No. 8 at the Naval Ordnance Laboratory (NOL) from March 27 to April 4, 1974. The general purpose of these tests was to generate LTA shape-change data to determine the effect of relevant nose-tip parameters on the formation and extent of irregular shapes. A summary of specific test objectives and approach is given in Section 4.1; samples of the resulting data are given in Section 4.2; and data trends are summarized in Section 4.3. A detailed presentation of the test data are also given in Volume XIV of this report series.

4.1 TEST OBJECTIVES AND APPROACH

The objectives of this experimental program were as follows:

- Evaluate the effects of

    - Reynolds number

    - Transition control

    - Surface roughness

    - Model size

    - Initial geometry

    - Blowing rate and wall temperature ratio

    on nosetip sharpening and the formation and extent of irregular shapes.

- Generate accurate recession data to evaluate heat transfer rates to scalloped surfaces.

- Generate shape-change and shock-shape data to evaluate the phenomena associated with the growth and degradation of small nose protuberances.

- Generate high-frequency acceleration data to evaluate the effects of oscillating shocks.

- Simulate flight shape-change response in a wind tunnel.

These objectives were addressed by exposing 30 camphor LTA models of
8 different initial geometries to various free stream conditions in the
NOL No. 8 hypersonic wind tunnel at a Mach number of 5. A typical model
geometry is shown in Figure 4-1, and the test matrix is given by Table
4-1. The large amount of data acquired to accomplish the test objective
included 16 mm and 35 mm shadowgraphs, 16 mm movies, 35 mm and 70 mm
photographs, and high-frequency acceleration measurements.

4.2   SAMPLE DATA RESULTS

The data of primary interest for this test series are the shape-
change histories of the LTA models. This information is available in
raw photographic data consisting of 16 mm sideview shadowgraph movies,
35 mm sideview shadowgraph pulsed photographs, 35 mm overhead pulsed
photographs, and 70 mm underside pulsed photographs. To reduce the
raw data to an easily usable form, tracings were made from the 35 mm
film to record model shape profile histories. An example of this, for
Run 805, is shown in Figure 4-2. In addition, further reduced data
related to shape-change history are typified by the stagnation point
axial recession history given for Run 805 in Figure 4-3.

Data of secondary interest for Series I included boundary layer
transition locations and subsequent sharpening phenomena. Initial transi-
tion locations were determined from tracings of 35 mm overhead and 70 mm
underside photographs, as shown in Figure 4-4, and were subsequently re-
duced to (S, ϕ) coordinates as shown by Figure 4-5. Both qualitative and
quantitative transition data are also available from the 70 mm front-
view photographs and 16 mm overhead high-speed movies, as demonstrated
by Figures 4-6 and 4-7, respectively. Information relative to sharpening
can be taken from most of the film sources, but is given most clearly
by the 70 mm underside photographs, of which examples are presented in
Figure 4-8.

Additional data of interest includes those related to unsteady
flow fields with oscillating shocks on irregular shapes. This area of
interest was addressed primarily through the usage of a very high speed
(20,000 frames/second) Hycam 16 mm camera taking shadowgraph movies, and
a three-axis high-frequency accelerometer system mounted on the sting.
The Hycam was triggered manually during the test when accelerometer
output increased. Figure 4-9 demonstrates typical accelerometer re-
sponses during periods of unsteady flow. Oscillating shocks during
these periods are also visible on the 16 mm and 35 mm shadowgraph film;
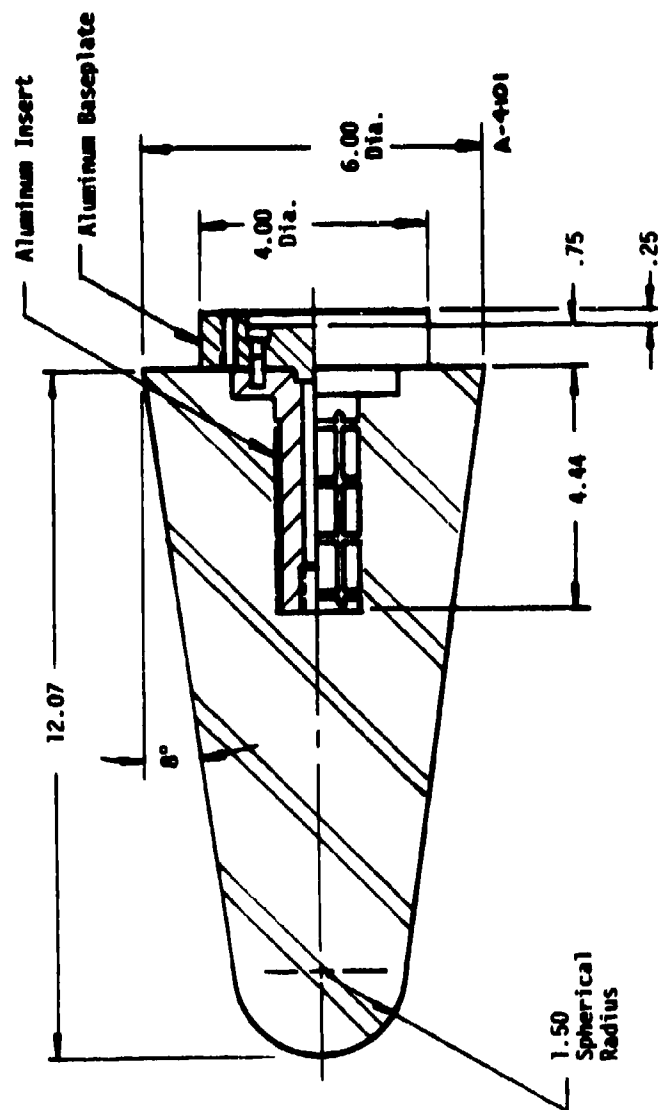an example of the latter is shown in Figure 4-10.

Figure 4-1.   Geometry for 1.5-Inch Nose Radius Camphor Model

TABLE 4-1

### TEST CONDITIONS FOR PANT SERIES I TESTS
MARCH/APRIL 1974

Run No.	Test Plan Point No.	Test Conditions				Camphor Model Configuration	Exposure Time (sec)
		Air Supply		Free Stream			
		P_0 (psia)	T_0 (°F)	Re_∞ (10^6/ft)	M_∞		
801	1	256	983	3.44	4.98	1.5" R_N Sphere-cone	186.33
802	3	311	970	4.09	4.98	1.5" R_N Sphere-cone	157.89
803	2	475	927	6.84	4.99	1.5" R_N Sphere-cone	115.80
804	8	190	983	2.51	4.96	1.5" R_N Sphere-cone, particle-loaded	178.91
805	4	507	987	6.56	5.00	1.5" R_N Sphere-cone	99.60
806	12	531	921	7.36	5.00	0.75" R_N Sphere-cone	87.19
807	5	323	1013	4.08	4.98	1.5" R_N Sphere-cone with groove	156.24
808	9	117	996	1.50	4.96	1.5" R_N Sphere-cone, particle-loaded	288[b]
809	13	713	971	9.38	5.00	0.75" R_N Sphere-cone	55.63
810	22	506	964	6.73	5.00	1.5" R_S/60°/8° Biconic	109.47
811[a]	10	58.8/ 88.3	972/ 972	0.77/ 1.12	4.95/ 4.95	1.5" R_N Sphere-cone, particle-loaded	172.83/ 305.43
812	14	996	807	15.70	5.01	0.75" R_N Sphere-cone	63.49
813	24	509	970	6.70	5.00	1.5" R_S/75°/8° Biconic	115.74
814	6	324	998	4.15	4.98	1.5" R_N Sphere-cone with 3 grooves	172.91
815	19	497	944	6.72	5.00	1.5" R_S Laminar-blunt	123.15
816	23	388	954	5.20	4.98	1.5" R_S/60°/8° Biconic	126.28
817	27	268	493	6.52	4.98	1.5" R_N Sphere-cone	325.48
818	28	403	508	9.56	4.99	1.5" R_N Sphere-cone	253.84
819[a]	15	360/ 821	812/ 804	5.69/ 12.96	4.98/ 5.01	0.75" R_N Sphere-cone	20.84/ 69.04
820	16	378	986	4.90	4.99	3.5" R_S Laminar-blunt	122.83
821	11A	569	973	7.47	5.00	2.5" R_N Sphere-cone	13.47
822	20	302	960	4.02	4.98	1.5" R_S Laminar-blunt	224[b]
823	25	400	986	5.18	4.99	1.5" R_S/75°/8° Biconic	130.48
824	7	416	535	9.44	4.99	1.5" R_N Sphere-cone	242.75
825	11B	558	990	7.20	5.00	2.5" R_N Sphere-cone	67.73
826	21	263	987	3.41	4.98	1.5" R_S Laminar-blunt	192.33
827	26	375	1008	4.76	4.99	2.5" R_S/55°/6° Biconic	139.04
828	30	v a r i a b l e			4.99	0.75" R_N Sphere-cone	91.11
829	29	v a r i a b l e			4.99	0.75" R_N Sphere-cone	116.03
830	17	268	985	3.47	4.98	3.5" R_S Laminar-blunt	153.52
831	18	197	998	2.52	4.97	3.5" R_S Laminar-blunt	231.08

[a]Dual Re_∞ test - values given are for first portion/second portion

[b]Approximate time only; film data incomplete
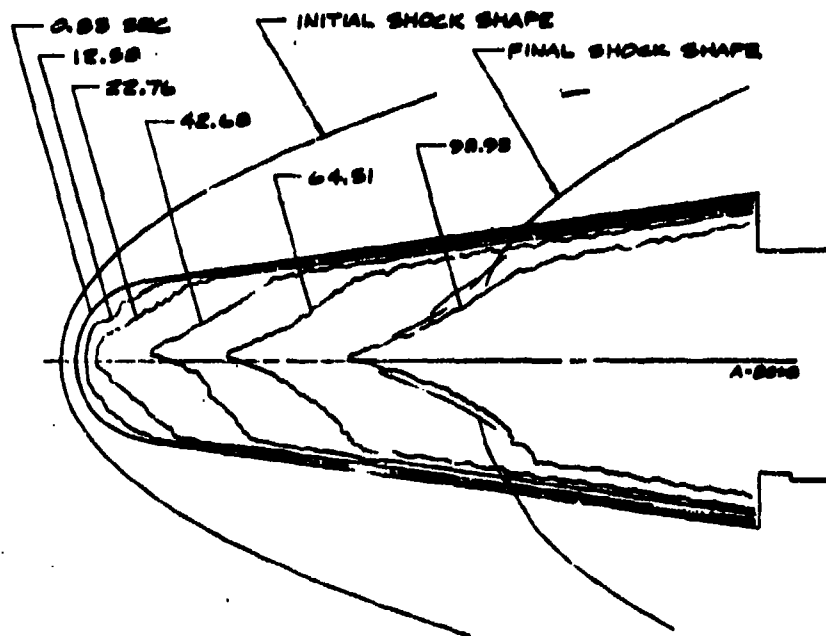
RUN 805, VERTICAL PLANE
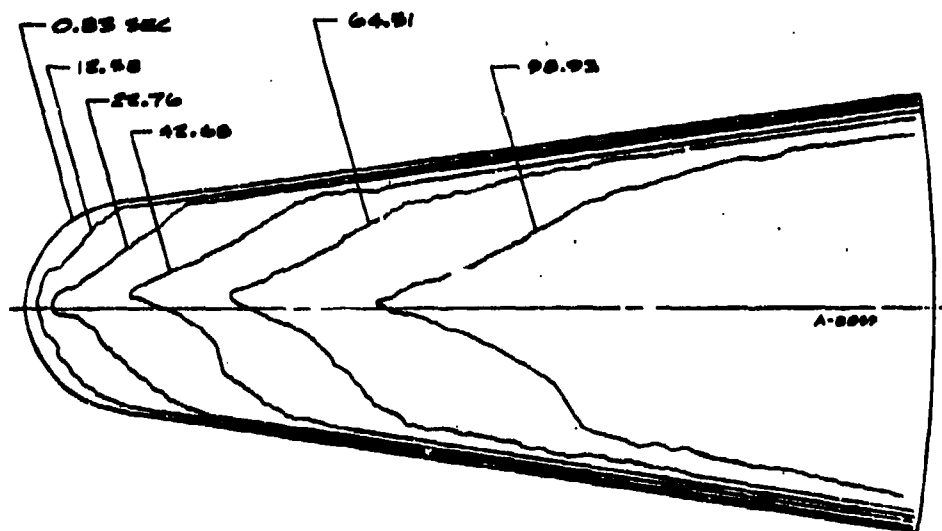
RUN 805, HORIZONTAL PLANE

Figure 4-2. Shape Profile History for Run 805
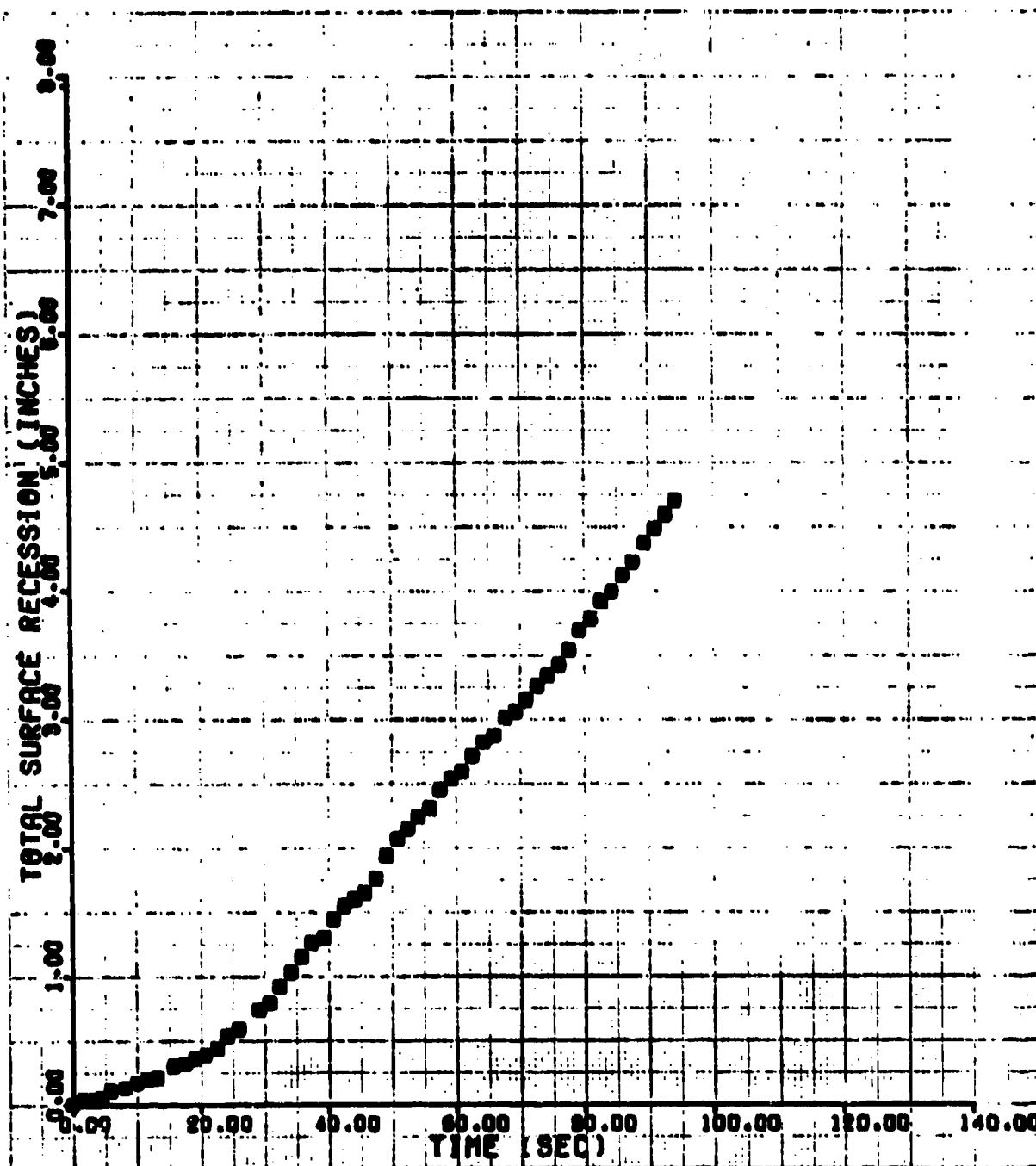
Figure 4-3.   Stagnation Point Axial Recession for Run 805
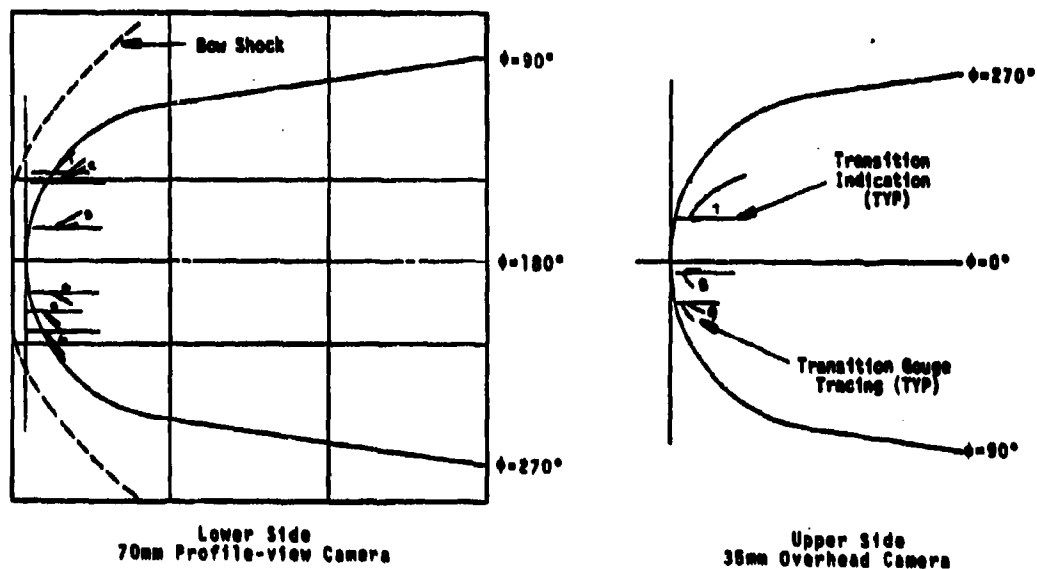
Figure 4-4.   Initial Transition Location Tracings for Run 805
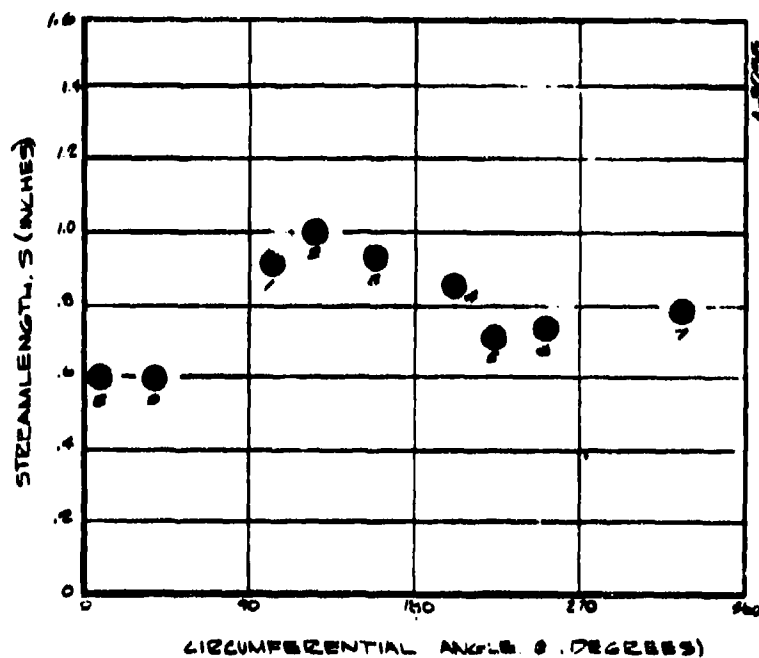
Figure 4-5.   Initial Transition Locations for Run 805
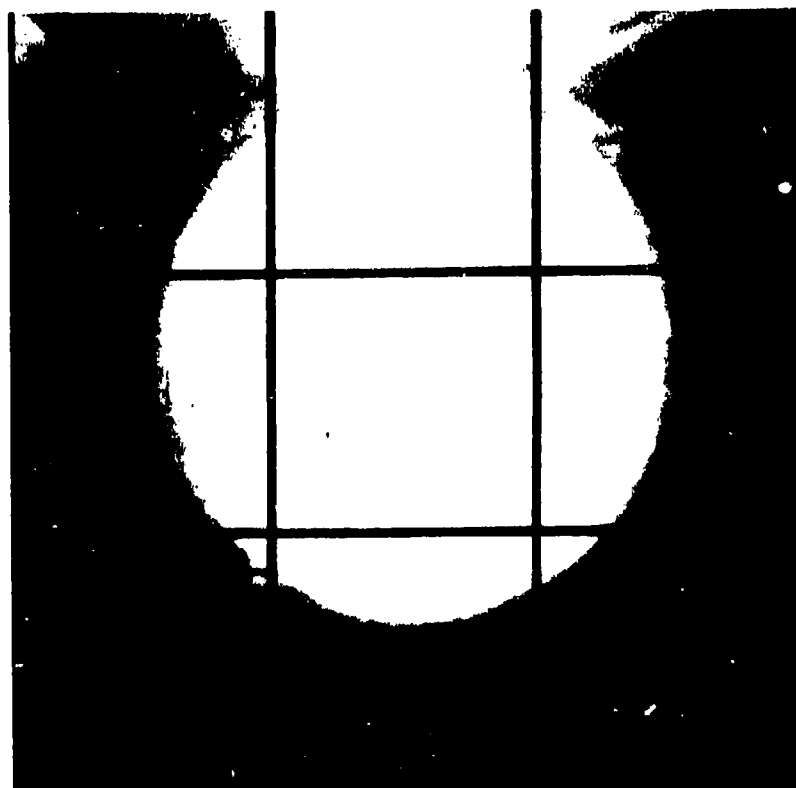
11.74 seconds
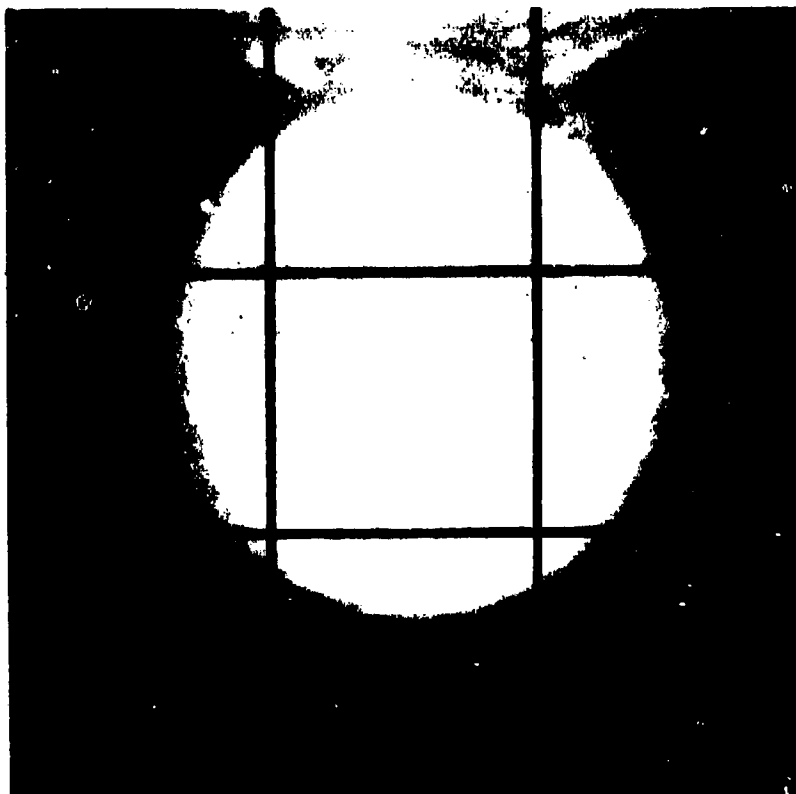
19.13 seconds

Figure 4-6. Typical 70mm frontview photographs (Run 805; 1.5-inch R_N sphere-cone; $Re_\infty = 6.56 \times 10^6/ft$, $T_o = 987°F$).

4-8
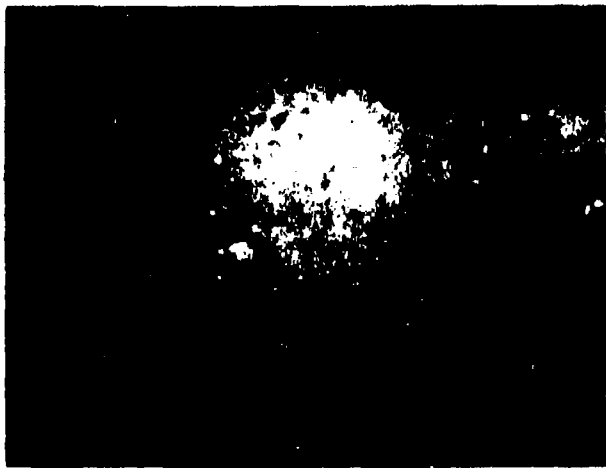
(a)
Model exposure time
approximately 0.5 second
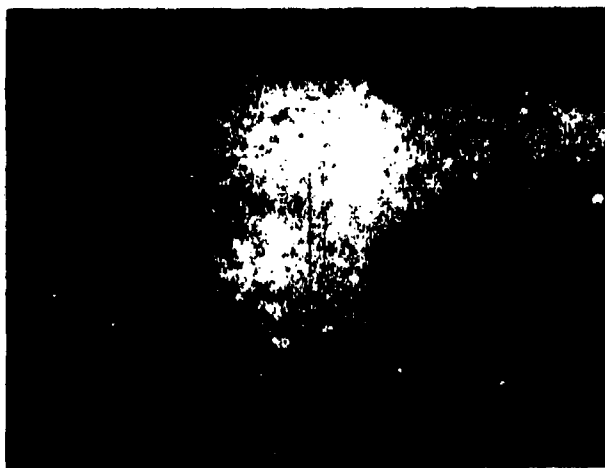
(b)
0.4 second after (a)
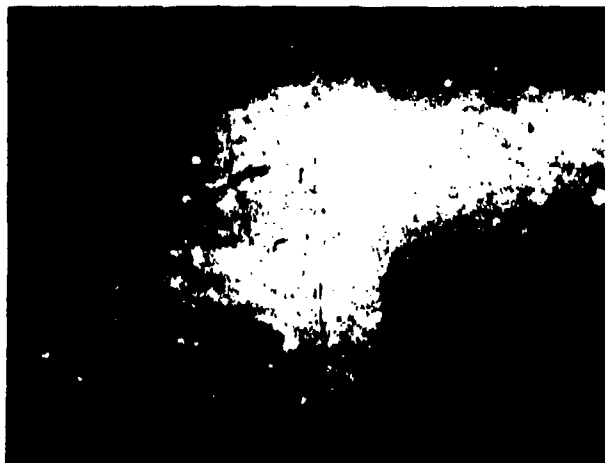
(c)
1.1 seconds after (a)

Figure 4-7. Example of Transitional Gouge Development from 16mm Overhead Camera. (Run 805; 1.5-inch R_N Sphere-Cone; Re_∞ = 6.56 x 10^6/ft, T_O = 987°F)
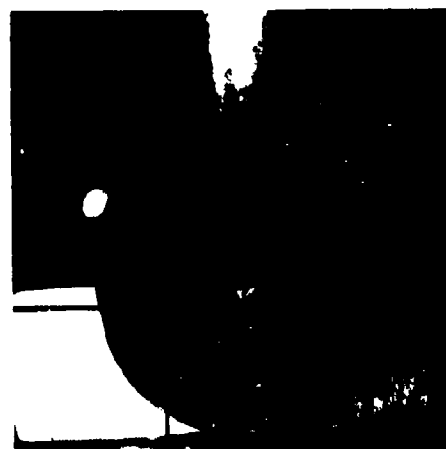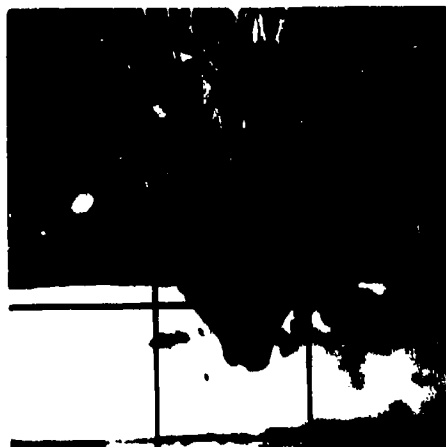
3.85 seconds   33.57 seconds   49.68 seconds

Figure 4-8. Typical 70mm sideview photographs (Run 805; 1.5-inch R_N sphere-cone; $Re_\infty = 6.56 \times 10^6/ft$, $T_0 = 987°F$).

(a)

1 second

(b)

Shock shape changes
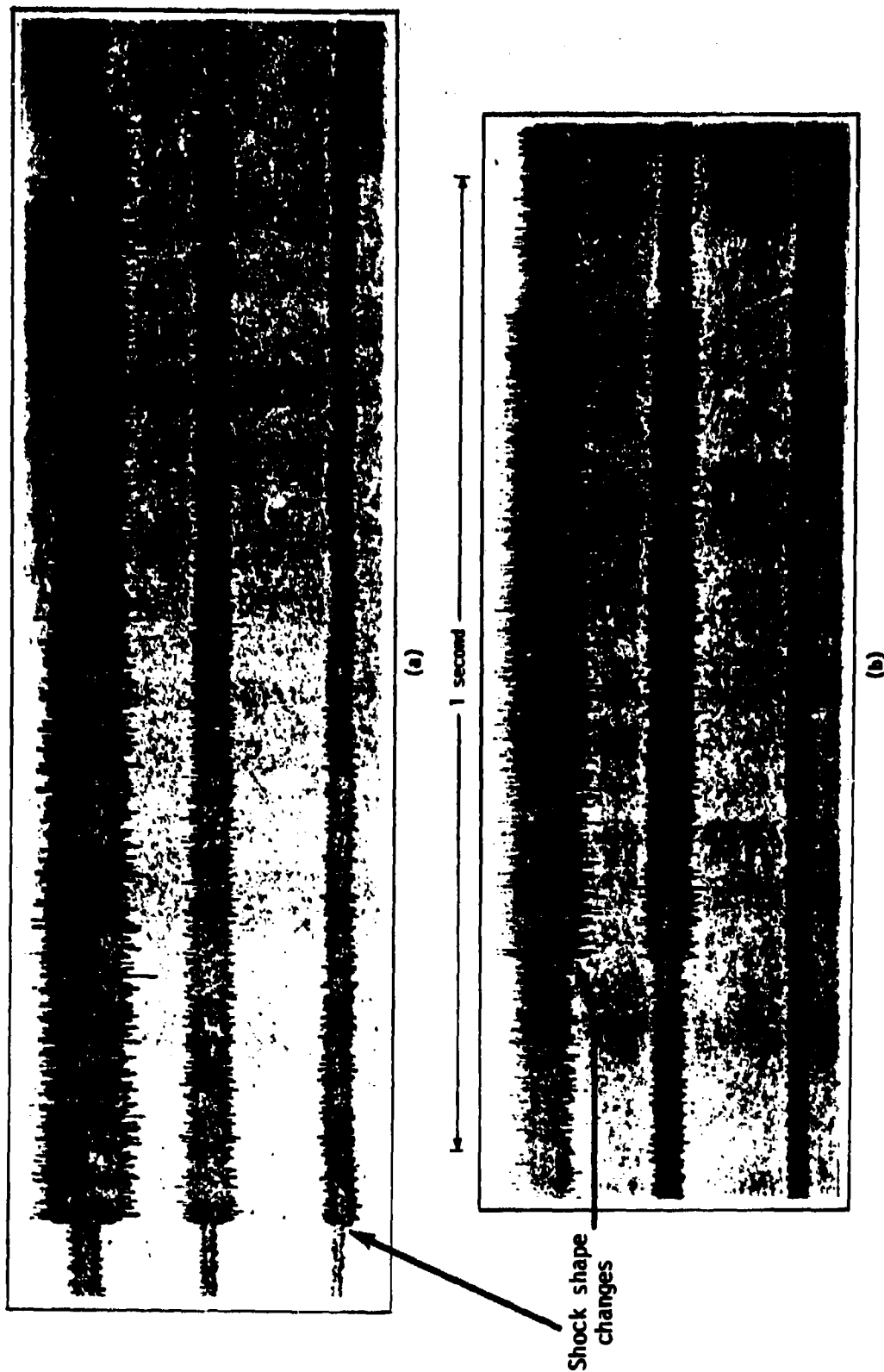
Figure 4-9. Example of Accelerometer Response for Run 805

(a)
43.80 seconds

(b)
43.84 seconds
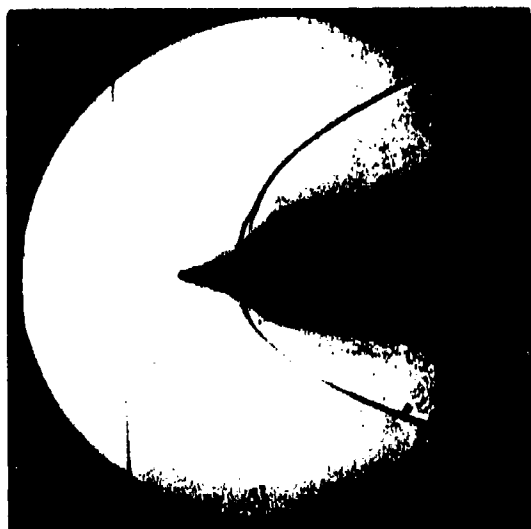
(c)
87.21 seconds
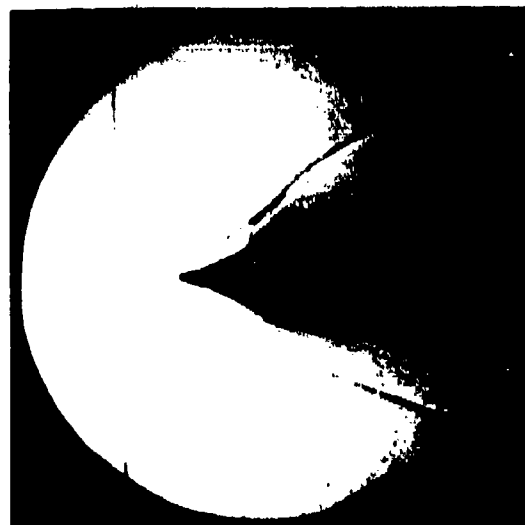
(d)
88.13 seconds

Figure 4-10.   Examples of Unsteady Flow Phenomena During
Run 805 (1.5-inch R_N Sphere-Cone; Re_∞ =
6.56×10^6/ft, T_0 = 987°F)

4.3   PRELIMINARY DATA TRENDS

The primary objective of this test series as described in Section 4.1, was to evaluate the effects of six significant parameters on the formation and extent of irregular shapes. Preliminary examination of the data leads to the following observations in regard to each parameter:

- **Reynolds number** — As shown in Figure 4-11, free stream Reynolds number has a strong effect on shape change..

- **Transition control** — Boundary layer trip grooves used on Runs 807 and 814 did not produce completely symmetric transition at the low Reynolds number conditions tested. However, shape profile development in these runs was different than exhibited by nongroved models.

- **Surface roughness** — Glass particles imbedded in the models for Runs 804, 808, and 811 had a strong effect on shape change, apparently impeding the formation of the irregular shape regime.

- **Model size** — Figure 4-12 illustrates that decreasing the model size (nose radius) causes an increase in the Reynolds number required to attain a given shape regime.

- **Initial geometry** — A comparison of post-sharpening and final shapes for models with various initial geometries is shown in Figure 4-13. It appears that there are only slight differences in final shape among the different initial geometry models. However, different shapes led to different times for sharpening.

- **Blowing rate (B') and wall temperature ratio (T_w/T_e)** — Tests run at low supply temperatures (T_o = 500°F compared to the baseline T_o = 1000°F) result in lower B' and higher T_w/T_e. The combined effect, as shown in Figure 4-14, is an increase in the Reynolds number required to attain a given shape regime.

An additional significant trend was noted in regard to unsteady flow fields; namely, unsteady flow phenomena existed for portions of about two-thirds of the runs, and for portions of virtually all runs which developed irregular shapes. Shape change after flow instabilities started tended to produce shapes which damped the instabilities. Cycles of steady to unsteady flow were observed.
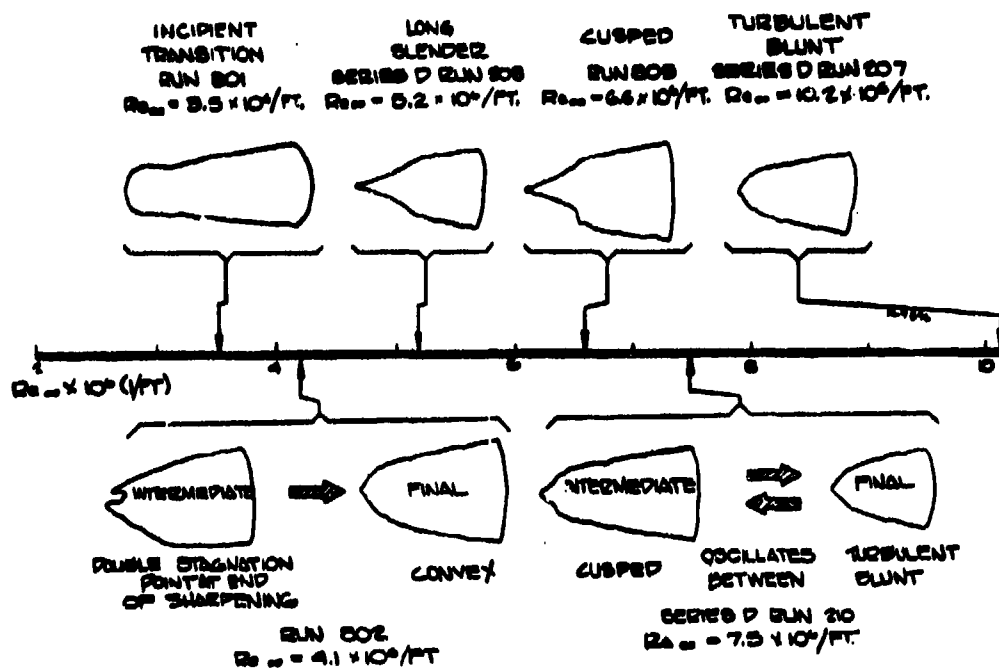
Figure 4-11.   Reynolds Number Effect on Model Final Shape
(All 1.5-Inch Sphere-Cones, Nominal T_O = 1000°F)
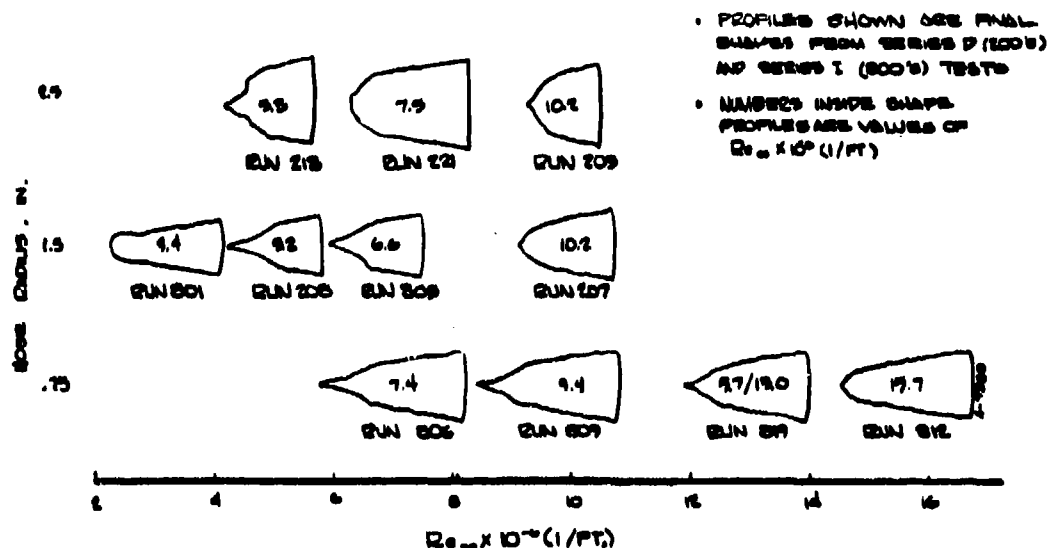
Figure 4-12.   Effect of Model Size on Shape Development

INITIAL GEOMETRY	RUN NO	Re_∞ (10^6/FT)	SHARPENING TIME (SEC)	POST-SHARPENED SHAPE	FINAL SHAPE
1.5° R_N SPHERE-CONE	002	4.09	60	96 SECONDS	127 SECONDS
1.5° $R_{SHOULDER}$ 60°/8° BICONIC					
1.5° $R_{SHOULDER}$ 75°/8° BICONIC					
1.5° $R_{SHOULDER}$ LAMINAR-BLUNT	822	4.03	40	48 SECONDS	98 SECONDS

(a)   Nominal Re_∞ = 4 x 10^6/ft

INITIAL GEOMETRY	RUN NO	Re_∞ (10^6/FT)	SHARPENING TIME (SEC)	POST-SHARPENING SHAPE	FINAL SHAPE
1.5° R_N SPHERE-CONE	208	5.25	40	48 SECONDS	128 SECONDS
1.5° R_S 60°/8° BICONIC	816	5.20	50	54 SECONDS	107 SECONDS
1.5° R_S 75°/8° BICONIC	823	5.18	60	78 SECONDS	128 SECONDS
1.5° R_S LAMINAR-BLUNT					

(b)   Nominal Re_∞ = 5 x 10^6/ft

Figure 4-13.   Comparison of Post-Sharpening and Final Shapes for Different
Initial Geometry Models

(c)   Nominal $Re_\infty = 6.7 \times 10^6$/ft

Figure 4-13.   Concluded

• PROFILES SHOWN ARE FINAL SHAPES FROM
  SERIES U (208) AND SERIES 1 (800 B) TESTS.
• NUMBERS INSIDE SHAPE PROFILES ARE
  VALUES OF $Re_\infty \times 10^{-6}$ (1/FT).
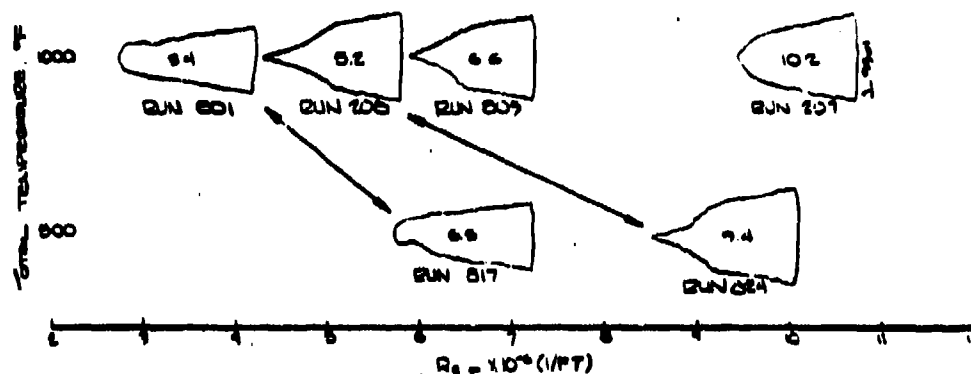
Figure 4-14.   Effect of Supply Temperature (T_o) on Shape Development

4-16

SECTION 5

SERIES J WIND TUNNEL TESTS

During the PANT program two calorimeter test series were performed to establish conditions required to promote boundary layer transition on rough axisymmetric blunt bodies. The first test program is referred to as Series A; the second as Series J. The results of Series A are documented in References 5-1, 5-2, and 5-3 which describe the test data, roughness augmented heating analysis, and boundary layer transition analysis, respectively. In this section a summary of the Series J test program is given. This includes a discussion of the experimental test objectives and approach (Section 5.1), as well as a brief overview of the significant test results (Section 5.2).

5.1 EXPERIMENT OBJECTIVES AND APPROACH

The test objectives were defined based on the data deficiencies which were noted at the completion of the Series A correlation efforts. The primary test objectives were:

- To evaluate the effect of body size on transition onset and location

- To evaluate the effect of body shape on transition onset and location

Secondary objectives were to obtain additional data on the effect of the wall temperature ratios, (T_w/T_e), on rough wall boundary layer transition and to obtain additional data relative to rough wall heating augmentation.

As can be inferred from the test objectives the primary deficiency of the Series A program was the lack of transition data on different size and shape bodies. Although the relative importance of these two parameters was not known, the Series A data did indicate the possibility of these parameters influencing boundary layer transition. This conclusion was primarily based on the experimental observation that transition on the roughened calorimeter models never occurred between the sonic point and tangency point. It was postulated that in this region transition is

5-1

suppressed by the independent or combined effects of the normal pressure gradient associated with centrifugal acceleration and/or the streamwise pressure gradient. For sphere cone models, both pressure gradients are proportional to the inverse of the nose radius. Hence, body size, in particular nose radius, was a parameter which deserved further consideration.

The Series A test program only partially addressed the importance of body shape on boundary layer transition. Differences in body shape reflect differences in the pressure gradients and, hence, could be expected to influence boundary layer transition. Furthermore, body shape could influence transition through the effects of boundary layer spreading.

Six models were selected to accomplish the above stated objectives. The model configurations are illustrated in Figures 5-1 and 5-2. Four of the models were sphere-cones having nose radii of 0.75, 1.5, 2.5[*], and 3.5 inches. The half cone angle for these models was 8°. The two remaining models were a 60° biconic model and a laminar ablated shape model.

The continuous thick skin calorimetry technique, used successfully during the Series A test program, was selected for obtaining heat transfer measurements. The Series J models were machined from Nickel 200 to a nominal wall thickness of 0.080 inch. The calorimeter shells were instrumented with 36 gauge (5 mil) Chromel-Alumel thermocouples. The number of thermocouples depended upon the size of the model; the larger models, such as the 3.5-inch sphere-cone model, had 78 thermocouples whereas the smallest model had 39 thermocouples. All of the models except for the Series A 2.5-inch nose radius model were grit blasted to obtain a uniformly distributed peak-to-valley roughness of 3.5 mils. The Series A model had a roughness of 3 mils. Additional details relative to the models may be found in Volume XV of this report.

The Series J test program was conducted in the Naval Ordnance Laboratory (NOL) Tunnel No. 8 from February 22, 1974 to February 26, 1974. This facility was chosen early in the PANT program based on its capability of providing hypersonic flow and high sonic point unit Reynolds numbers (Reference 5-4). The free stream Mach number for the Series J tests was 5.

---

*The 2.5-inch model was tested during Series A and was reused for Series J.

(b) 1.5-inch Nose Radius

(d) 3.5-inch Nose Radius

(a) 0.75-inch Nose Radius

(c) 2.5-inch Nose Radius

Figure 5-1. Series J Sphere-Cone Models

SAMPLE COORDINATES

X	Y
.030	.180
.120	.992
.270	1.405
.780	1.839
.745	2.239
1.079	2.584
1.494	2.822
1.939	2.991
2.396	3.133
2.860	3.260
3.325	3.379
3.794	3.497
4.856	3.609
5.05	3.742
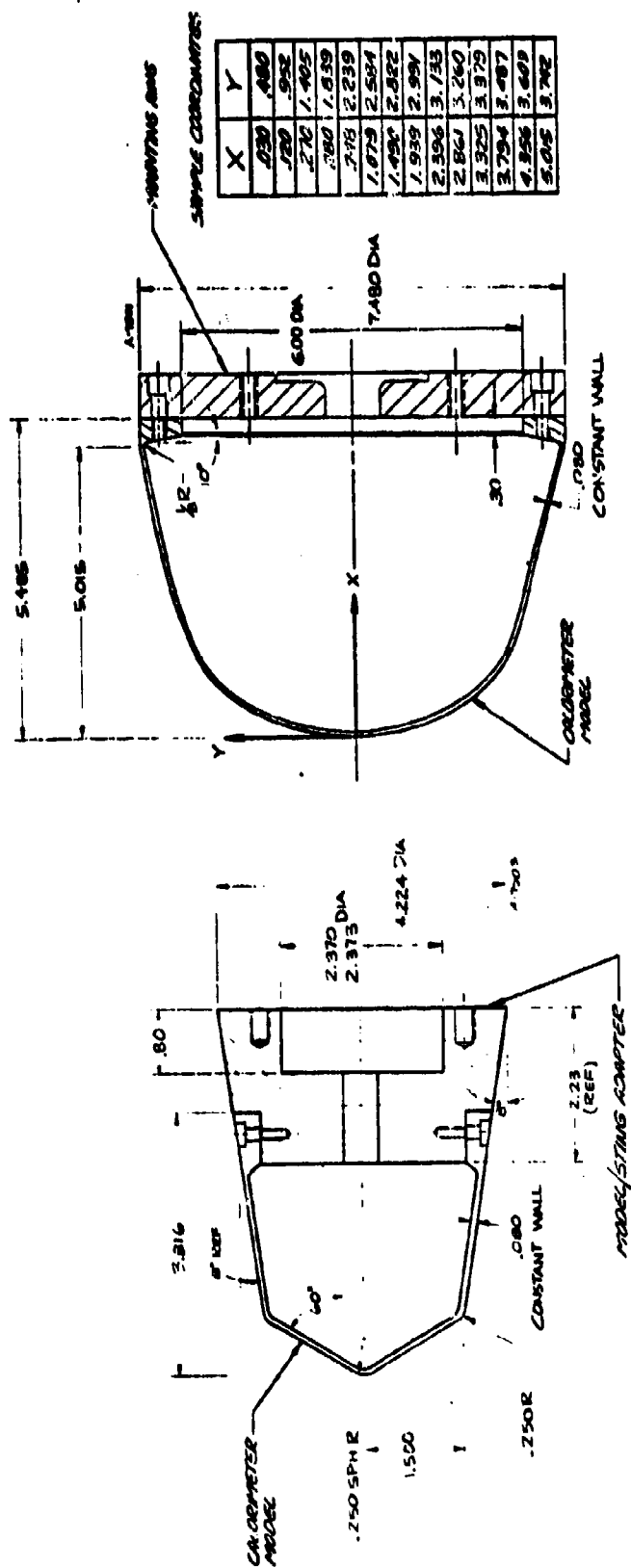
(b) Laminar Ablated Shape Model

(a) 60° Biconic Model

Figure 5-2. Series J Biconic and Laminar Ablated Shape Models

5.2   EXPERIMENTAL RESULTS

The Series J test program successfully accomplished all stated objectives. The effects of body size (nose radius) and body shape on boundary layer transition were adequately characterized. A total of 40 calorimeter model entries were made in the NOL wind tunnel, spanning a sonic point unit Reynolds number range from 0.42 x 10⁶/ft to 7.4 x 10⁶/ft. A summary of the Series J test conditions is given in Table 5-1. In this section, a brief summary is given of the data reduction procedures as well as some of the more salient results.

The Series J data were reduced using the techniques developed during the Series A test program. These techniques include temporal curve fitting of the individual thermocouple temperature data, calculation of the local incident heat flux accounting for streamwise conduction, and calculation of the local heat transfer coefficient based on recovery temperature. These techniques are documented in Reference 5-3 and Volume XV of this report.

Using these data reduction techniques, heat transfer coefficients can be presented either as a function of meridian location or as a function of time. For purposes of this report, heat transfer coefficient distributions presented as a function of meridian location will be referred to as early time data. This reflects the fact that the heat transfer coefficients are evaluated at one time, typically 1 second. Similarly, heat transfer coefficient distributions presented as a function of time will be referred to as late time data. In this case, the heat transfer coefficients are calculated at various times which correspond to various wall temperature ratios during the test. The handling of streamwise conduction is slightly different for early time as opposed to late time (refer to Reference 5-3 or Volume XV). As indicated in the Appendix of this report, late time data is used in correlating the transition data. This is necessary since rough wall boundary layer transition is a strong function of the wall temperature ratio.

Figure 5-3 illustrates typical early time heat transfer coefficient (HTC) values as a function of nondimensional streamwise length (S/R_N) for the 1.5-inch nose radius sphere cone model, the biconic model, and the laminar ablated shape model. Several interesting trends can be noted from this figure. First, the lack of data scatter at any streamwise location indicates the consistency and accuracy of the calorimeter data. Second, all of these runs to a certain extent show the existence of boundary layer

TABLE 5-1

ACTUAL TEST CONDITIONS FOR PANT SERIES J WIND TUNNEL TESTS

Run No.	Model No.	Model Description**	k (mils)	Supply Conditions			Free Stream Conditions		
				T_0 (°F)	P_0 (psia)	Film Cooling ΔP_f (psi)	M_∞	Re_∞ (10^6/ft)	$Re*$ (10^6/ft)
601	4	2.5 in. R_N Sphere/cone	3.0	843	127	20	4.97	1.94	.83
602				865	134	30	4.97	2.00	.85
603				847	129	20	4.98	1.96	.83
604				873	250	30	4.99	3.67	1.59
605	18	3.5 in. R_N Sphere/cone	3.5	878	142	20	4.98	2.08	.90
606				871	73	12	4.95	1.09	.45
607				879	107	15	4.96	1.58	.67
608				898	279	30	4.99	3.98	1.74
609				520	86	12	4.95	2.04	.78
610				526	117	15	4.96	2.74	1.05
611				505	181	20	4.97	4.31	1.67
612	16	.75 in. R_N Sphere/cone		911	283	30	4.99	3.98	1.75
613				898	155	20	4.98	2.22	.96
614				885	109	15	4.96	1.60	.67
615				889	130	30	4.97	1.89	.81
616				904	186	22	4.97	2.66	1.15
617				900	212	32	4.98	3.04	1.32
618	17	1.5 in. R_N Sphere/cone		844	122	17	4.97	1.87	.79
619				851	149	20	4.98	2.25	.96
620				859	272	30	4.99	4.05	1.76
621				845	181	20	4.98	2.75	1.18
622				555	103	10	4.96	2.31	.89
623				569	126	12	4.96	2.77	1.08
624				513	181	20	4.97	4.31	1.66
625				857	91	10	4.96	1.38	.58
626				859	89	30	4.95	1.35	.56
627				855	70	10	4.95	1.07	.44
628	20	Biconic, R_S = 1.5 in.		865	275	30	4.99	4.07	2.53
629				848	139	20	4.97	2.12	1.28
630				834	68	10	4.95	1.06	.52
631				839	101	10	4.97	1.55	.86
632				849	168	20	4.98	2.54	1.57
633				731	509	30	5.00	8.79	5.32
634	19	Laminar Ablated Shape, R_S = 3.5 in.		479	439	30	5.00	10.90	4.70
635				515	829	30	5.00	19.41	7.59
636				865	276	30	4.99	4.09	1.78
637				825	62	10	4.95	.98	.42
638				839	135	20	4.97	2.08	.90
639				819	101	10	4.97	1.59	.68
640				831	162	20	4.98	2.37	1.08

*All runs at zero angle-of-attack

**All model grit blasted
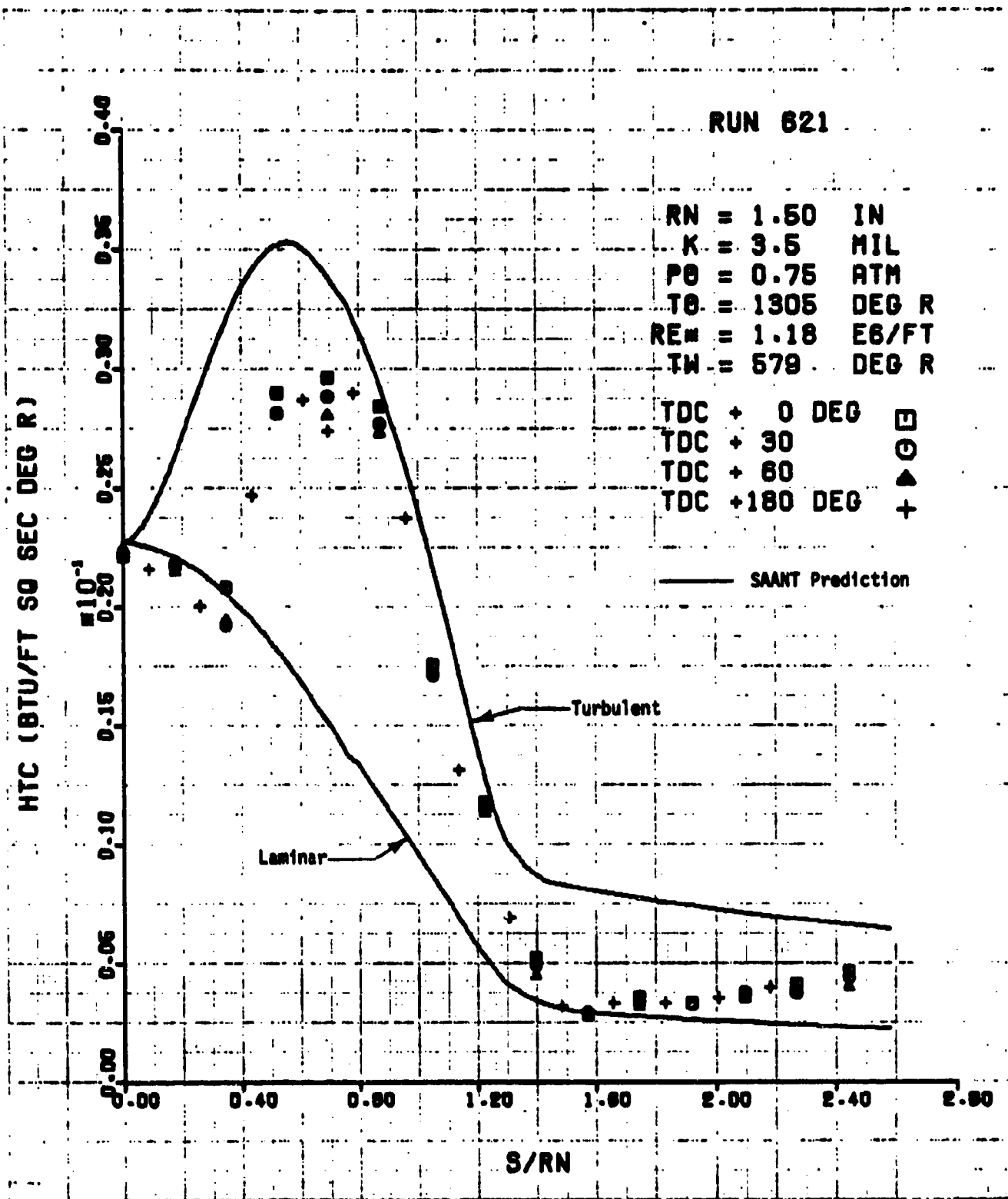
(a) 1.5-inch Sphere-Cone Model

Figure 5-3. Typical Early Time Heat Transfer
Coefficient Distributions
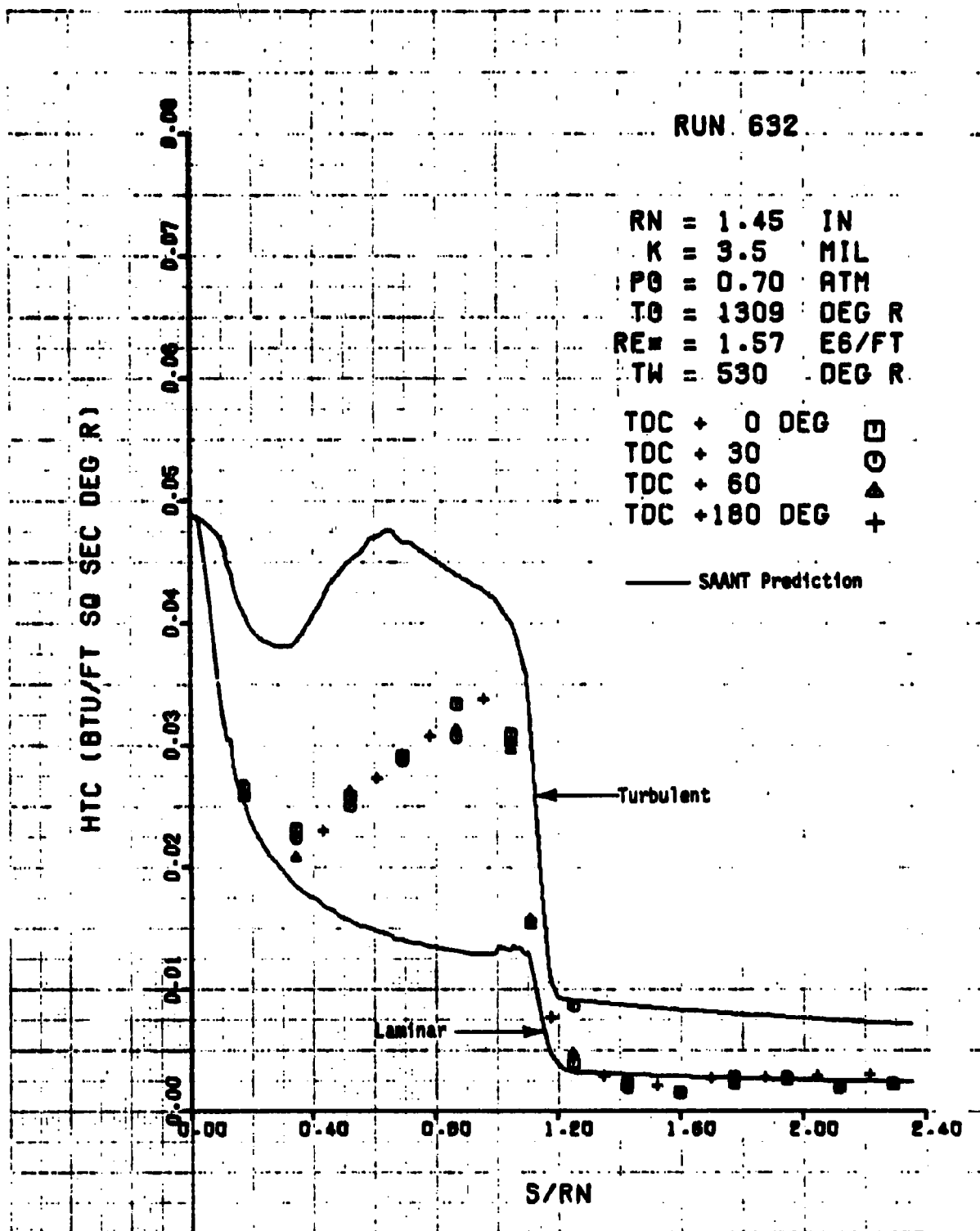
(b) 60° Biconic Model

Figure 5-3. Continued

(c) Laminar Ablated Shape Model

Figure 5-3. Concluded

relaminarization in the corner region of the models. This phenomena was also noted in the Series A tests, and has also been observed on graphitic models tested in the 50 MW AFFDL Arc Facility (Reference 5-5). Third, the transitional heat transfer coefficient distributions are similar for the sphere cone and laminar ablated shape model and quite different for the simple biconic model.

Figure 5-4 compares turbulent heat transfer coefficient distributions for three of the four sphere cone models tested during Series J. The nominal sonic point unit Reynolds number for these runs is 1.75 x 10^6/ft. This figure illustrates that boundary layer transition is affected by the size of the model; however, the effect is not large. Indeed, as is indicated in Section 6.1, the Series J transition data were found to correlate reasonably well using previously derived Series A transition criterion. This criterion indicates a nose radius dependency of $R_N^{0.15}$.

Figure 5-5 illustrates heat transfer coefficient distributions for the biconic model as a function of Reynolds number. The most interesting observation is the increasing trend of the heat transfer coefficient along the fore cone of the model. This trend was also observed in the Series A test program on the simple biconic model (Reference 5-6). Boundary layer solutions performed for both of these shapes indicate that the heat transfer on the fore cone is very sensitive to the boundary layer edge entropy.

Some examples of late time data reduction are shown in Figure 5-6 for the 3.5-inch sphere cone model, the biconic model, and the laminar ablated shape model. This figure presents heat transfer coefficient distributions at various times during the test. The models heat up during the test, and different times correspond to different wall temperature conditions. That is, wall temperature ratio increases as the time increases.

Laminar heat transfer coefficient distributions are shown as the solid line in Figure 5-6. These predictions were made using the PANT shape change code including the modification described in Section 6.2. The solutions were performed at a wall temperature corresponding to 1 second test time; however, laminar heat transfer is insensitive to the wall temperature ratio and, hence, these represent laminar heat transfer over the indicated test times.

Comparison of the data with the theoretical laminar distribution illustrates the strong dependency of boundary layer transition on wall temperature ratio. For all the models shown in Figure 5-6, the transition
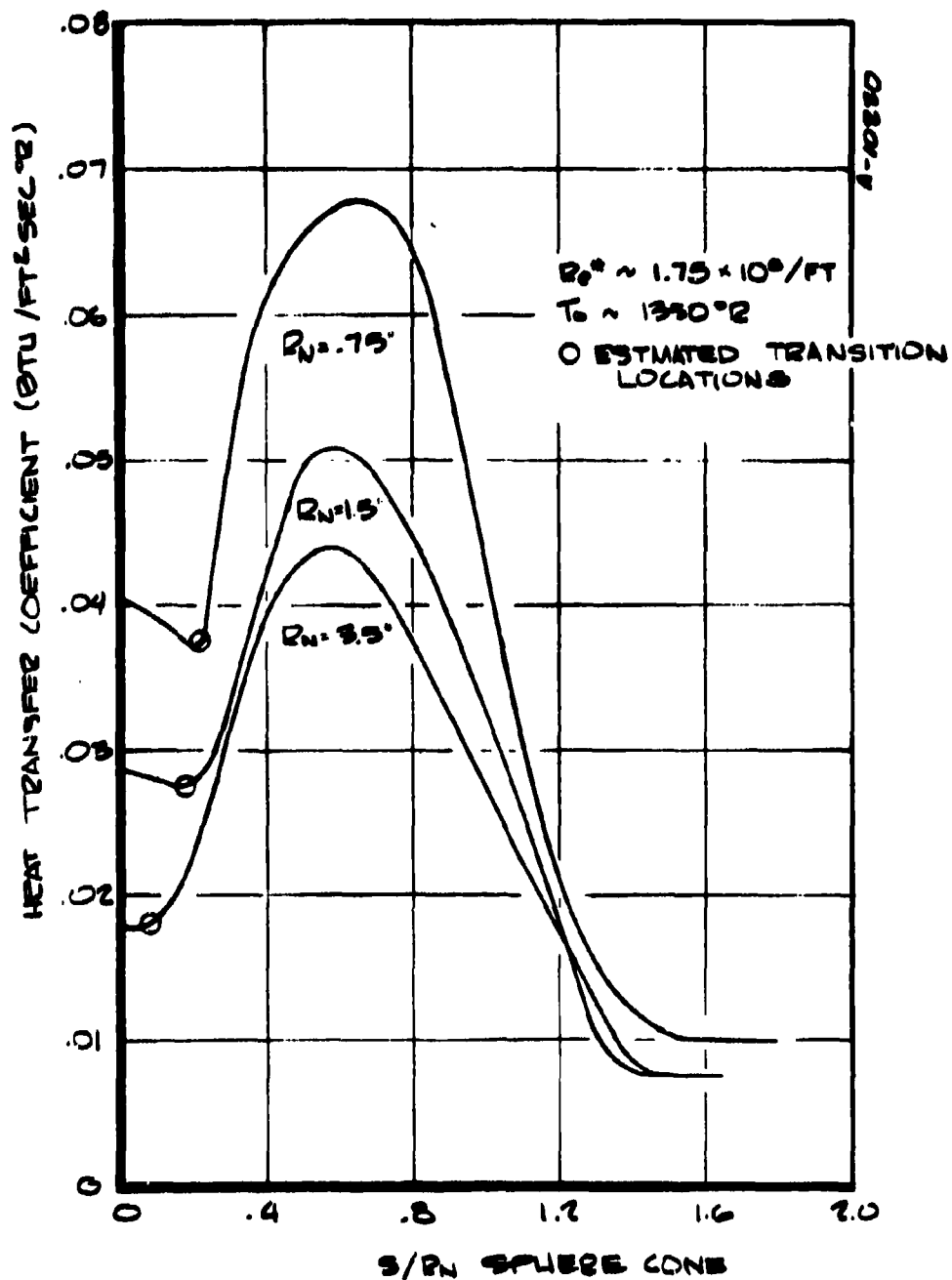
Figure 5-4.   Comparison of Sphere-Cone Turbulent Heat Transfer
Coefficient Distribution Data
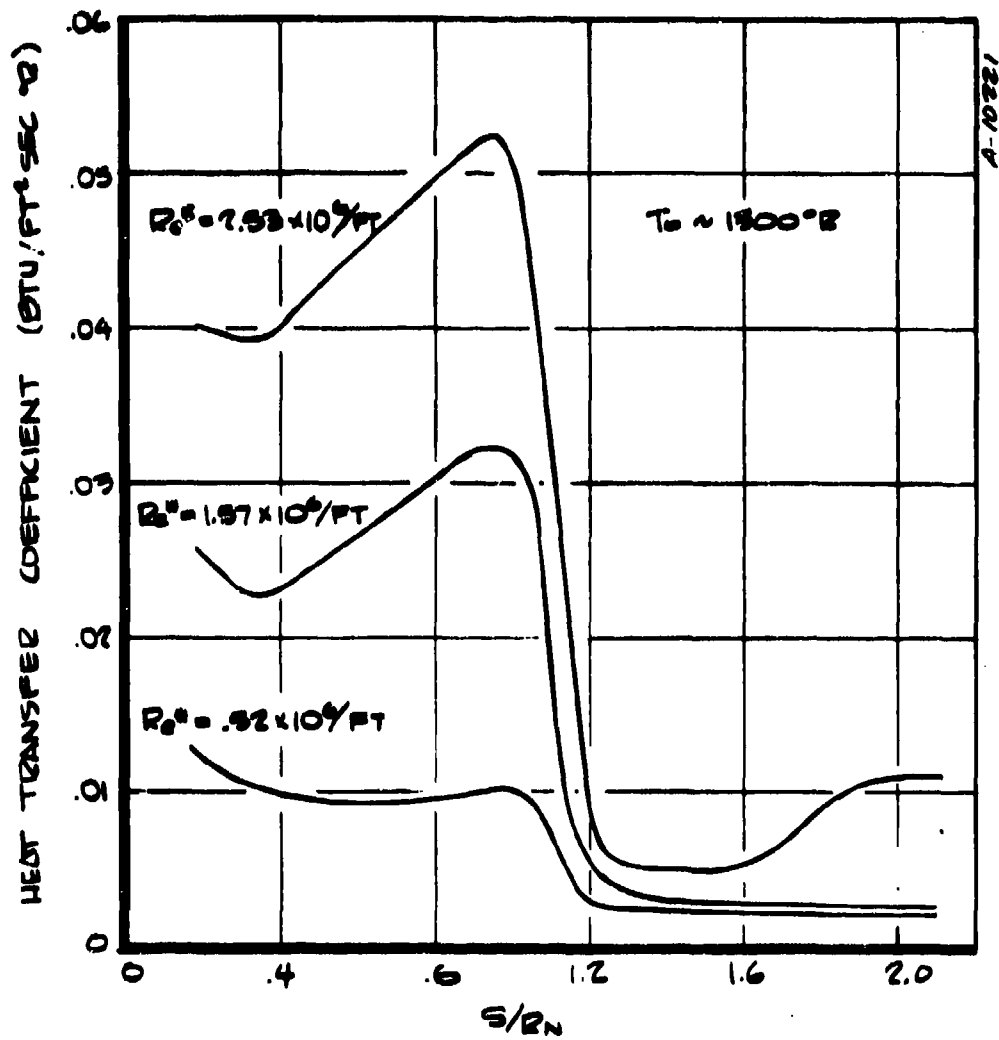
Figure 5-5.   Biconic Heat Transfer Coefficient Distribution Data

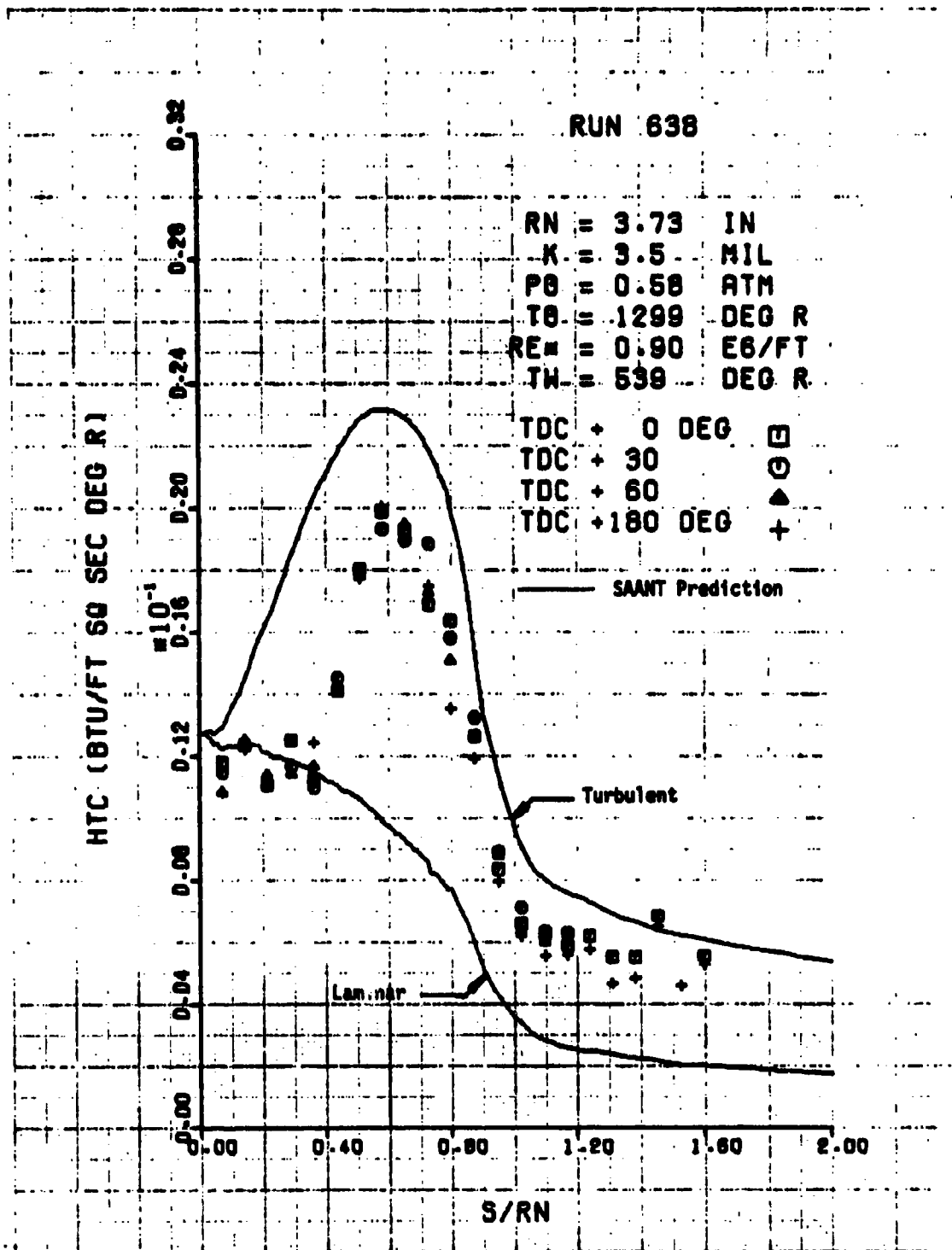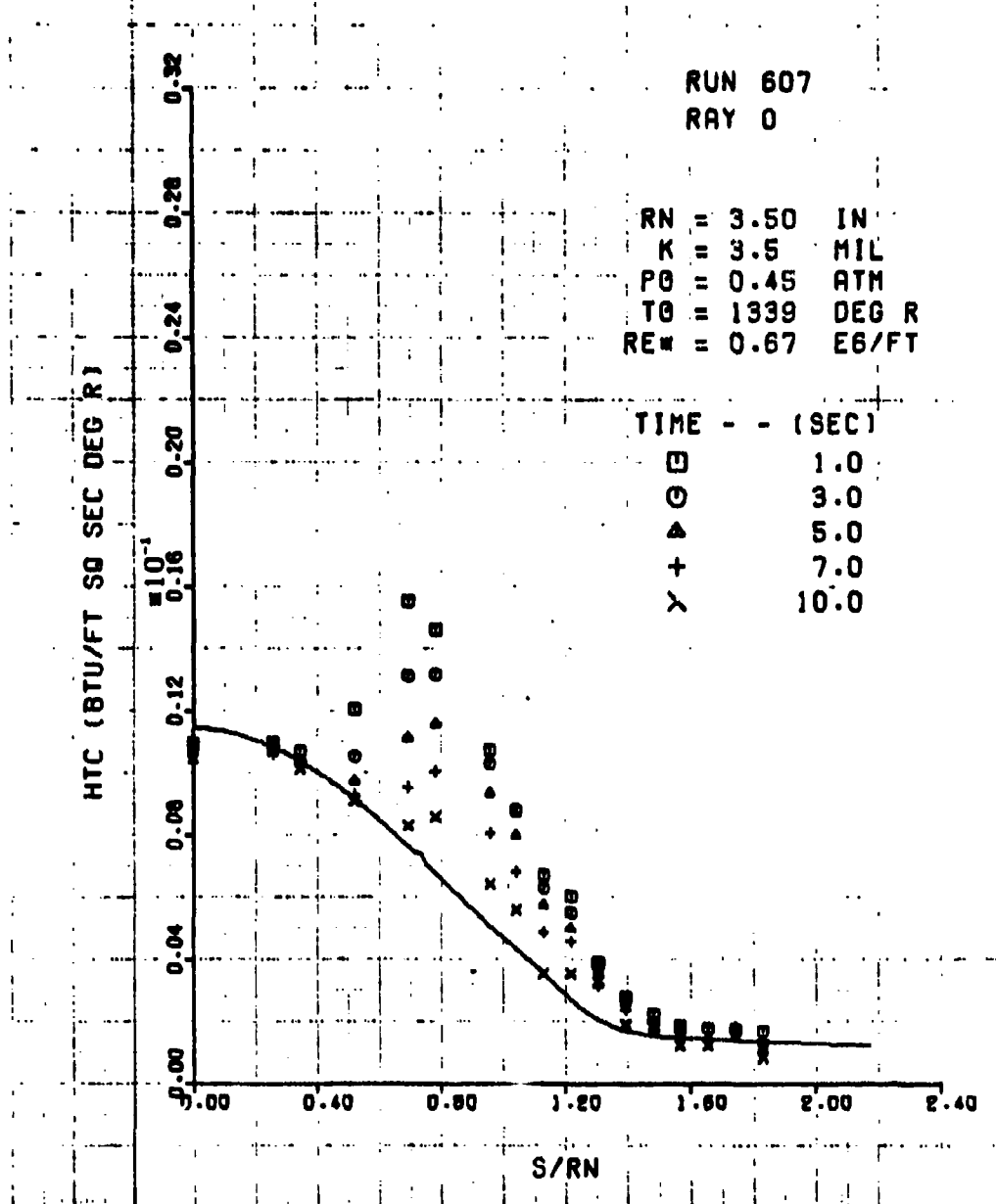(a)   3.5-inch Sphere Cone Model

Figure 5-6.   Typical Late Time Heat Transfer Coefficient Distributions
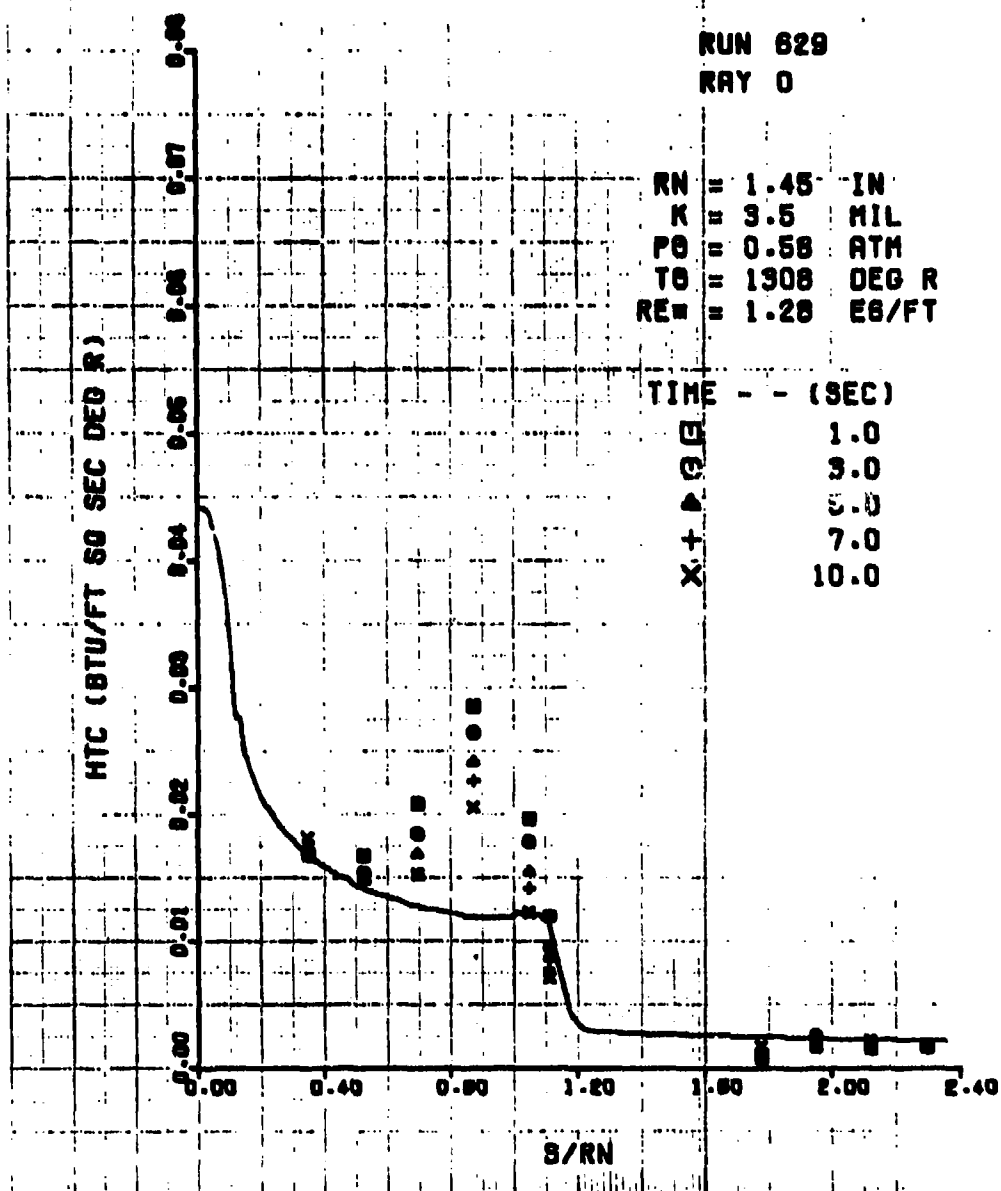
(b) Biconic Model

Figure 5-6. Continued

5-14
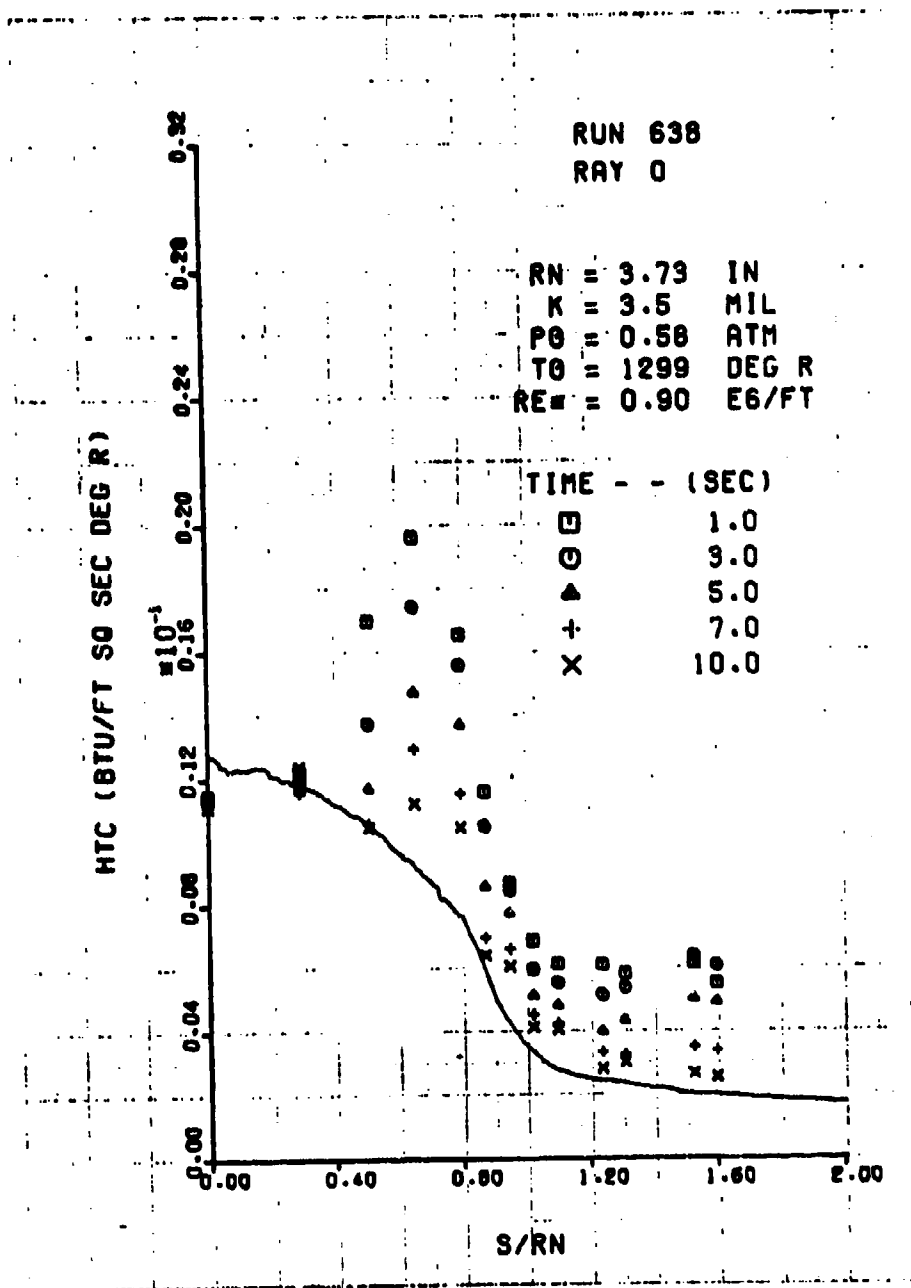
(c) Laminar Ablated Shape Model

Figure 5-6. Concluded

5-15

location clearly moves downstream as the test time increases or, more appropriately, as the wall temperature ratio increases. This result was adequately investigated in the Series A test program on sphere-cone models and the Series J test results confirm the effect of the wall temperature ratio for the sphere-cone models as well as for the biconic and laminar ablated shape model.

In summary, the Series J test program has provided a substantial data base from which the effects of body size and shape on rough wall boundary layer transition can be determined.

SECTION 5 REFERENCES

5-1. Jackson, M. D. and Baker, D. L., "Passive Nosetip Technology (PANT), Interim Report, Volume III — Surface Roughness Effects, Part I — Experimental Data," SAMSO TR-74-86, Aerotherm Report 74-90, Aerotherm Division, Acurex Corporation, January 1974.

5-2. Powars, C. A., "Passive Nosetip Technology (PANT), Interim Report, Volume III — Surface Roughness Effects, Part II — Roughness Augmented Heating Data Correlation and Analysis," SAMSO TR-74-86, Aerotherm Report 74-90, Aerotherm Division, Acurex Corporation, January 1974. (Confidential)

5-3. Anderson, A. D., "Passive Nosetip Technology (PANT), Interim Report, Volume III — Surface Roughness Effects, Part III — Boundary Layer Transition Data Correlation and Analysis," SAMSO TR-74-86, Aerotherm Report 74-90, Aerotherm Division, Acurex Corporation, January 1974. (Confidential)

5-4. "A Recommended Revised Wind Tunnel Test Plan for the PANT Program," Aerotherm Report TM-71-12, Aerotherm Division, Acurex Corporation, July 1971.

5-5. Anderson, A. D. and Jackson, M. D., "Study of Relaminarization on ATJ-S Graphite Thermostructural Models Tested in The AFFDL 50 MW Facility," AFML TR-74-147, July 1974.

5-6. Abbett, M. J. and Davis, J. E., "Passive Nosetip Technology (PANT), Interim Report, Volume IV — Heat Transfer and Pressure Distribution on Ablated Shapes, Part II — Data Correlation and Analysis," SAMSO TR-74-86, Aerotherm Report 74-90, Aerotherm Division, Acurex Corporation,

SECTION 6

IMPROVED NOSETIP PERFORMANCE ANALYSIS TECHNIQUES

At the completion of testing under PANT Task 4.2.5, several
analysis tasks were performed to upgrade the computer code developed
under previous PANT tasks (4.2.1 through 4.2.4). The efforts consisted
of either the correlation of PANT test data to determine shape change
response regimes or the evaluation of improved computational tools for
nosetip design analysis. Response trends from the respective test series
are presented in the test summary sections. In this section, improved
modeling procedures are presented and results, using the improvements,
are compared to results from previous calculations for seven baseline
flight environment cases. Section 6.1 summarizes recommended modifica-
tions to the PANT rough wall transition criterion. Section 6.2 describes
a modified technique for computing turbulent heat transfer on a reentry
vehicle nosetip. Section 6.3 discusses numerical techniques used to
calculate nosetip shape and shape change response. The comparative
calculation results are presented in Section 6.4.

6.1 UPDATED TRANSITION CRITERIA

A detailed discussion of the PANT rough wall transition studies
is presented in the appendix to this report. The primary results are
outlined in the following summary.

Two experimental programs (Series A and J) carried out at $M_\infty = 5$
in NOL wind tunnel No. 8, using roughened calorimeters, form the data
base for the rough wall transition correlation and analysis. In Series A,
the surface roughness varied over the range (0.6 to 80 mils) so that the
relative roughness, k/θ, spanned the values of interest for nosetip
materials in flight. Also, values of the wall cooling ratio (T_w/T_e)
and momentum thickness Reynolds number covered the range of primary
interest. In Series J, several additional calorimeter models of various
geometries were tested in order to evaluate nose radius and shape effects
on transition; all models had the same surface roughness (3.5 mils).

The data from Series A were correlated in terms of the momentum thickness Reynolds number (representing the ability of the boundary layer to amplify disturbances) versus a modified relative roughness, $(T_e/T_w)(k/\theta)$, (representing the strength of the disturbance). This correlation approach is illustrated on the sketch below:
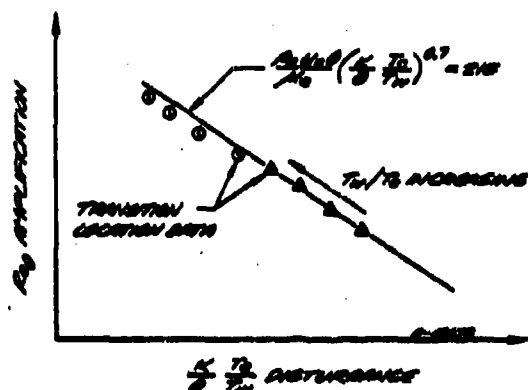
Two aspects of transition were correlated:

- Transition onset, describing when roughness induced transition occurs in the subsonic region.

- Transition location, describing the position of the beginning on transition when it occurs in the subsonic region.

These criteria may be stated in terms of critical values of the transition parameter,

$$Re_\theta \left(\frac{T_e}{T_w} \frac{k}{\theta} \right)^{0.7} = \left\{ \begin{array}{l} 255^*, \text{ onset} \\ 215 \ , \text{ location} \end{array} \right\} \tag{6-1}$$

Series J data substantiated both criteria developed from Series A data.

An analysis of exact smooth wall boundary layer profiles showed that the empirical disturbance parameter, $(T_e/T_w)(k/\theta)$, correlates very well with the relative kinetic energy at the top of the roughness elements, $\rho_k u_k^2/\rho_e u_e^2$. This, along with physical reasoning, suggests that the latter parameter is the proper physical measure of the disturbance. Using this concept, a function,

$$\psi = \frac{B'}{10} + \left(1 + \frac{B'}{4} \right) \frac{\rho_e}{\rho_w} \tag{6-2}$$

---

*Evaluated at the sonic point.

6-2

was developed to replace T_w/T_e in the empirical disturbance parameter, thereby accounting for the effects of blowing, ablation, wall cooling ratio, and/or dissociation. For low enthalpy, nonablating situations, the function ψ is the wall cooling ratio (T_w/T_e). For the high enthalpy, ablating case, Equation (6-2) indicates the effect of B' and ρ_e/ρ_w on the kinetic energy profile and, hence, on the roughness generated boundary layer disturbances. The transition criteria become

$$\mathrm{Re}_\theta \left(\frac{k}{\psi\delta} \right)^{0.7} = \begin{Bmatrix} 255^*, \text{ onset} \\ 215 \text{ , location} \end{Bmatrix} \qquad (6\text{-}3)$$

Because the above transition criteria are closely associated with physical roughness dimensions, accurate values of surface roughness in the particular flight or test being analyzed are essential. In clear air flight cases and some ground tests, this roughness would correspond to that associated with laminar ablation. In tests where a nosetip is rapidly exposed to a severe environment or is exposed to particle laden flows, other roughnesses such as machining marks, fabrication variations, or impact craters may be important. In the past, clear air predictions have been based on effective roughnesses inferred from shape change data. Effective roughness dimensions inferred using Equation (6-3) should agree with physical roughness dimensions measured from photomicrographs of laminar ablation models if roughness does not change during model cooldown.

For ATJ-S graphite, the roughness inferred using the criteria given by Equation (6-3) above is between 0.4 and 0.6 mil (Reference 6-1) ATJ-S photomicrograph data are reported in Reference 6-2 and shown in Figure 6-1. The two lines represent the best fit of measurements from high (50 to 170 atm) and low (0.05 to 25 atm) stagnation pressure test models. High pressure tests were most probably turbulent; whereas, low pressure tests were probably laminar. A peak-to-valley roughness height for use in the PANT correlations can be derived from Figure 6-1. This roughness is defined as the distance from the significant peaks to the significant valleys and could be represented as the distance between the 0.16 probability datum and the 0.84 probability datum. This would, therefore, include the middle 67 percent of all peaks or valleys. The peak-to-valley roughness (k_{pv}) is

$$k_{pv} = y_{16} - y_{84} = 0.67 - 0.18 \sim 0.5 \text{ mil} \quad \text{(laminar)}$$
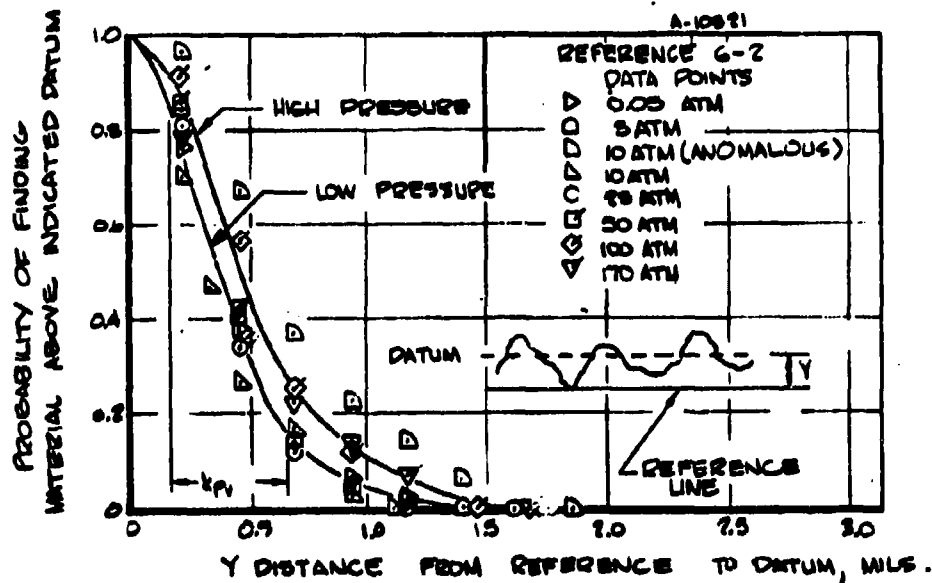
Figure 6-1. Microroughness Height Distributions for ATJ-S Graphite

For an upper limit (10 percent to 90 percent),

$$k_{pv} = y_{10} - y_{90} = 0.80 - 0.15 \sim 0.65 \text{ mils} \quad \text{(upper)}$$

For an estimate of turbulent microroughness, the high pressure curve
gives

$$k_t = y_{16} - y_{84} = 0.85 - 0.25 = 0.6 \text{ mils} \quad \text{(turbulent)}$$

It is encouraging that the roughness height inferred from the ablation
test data (0.4 to 0.6 mil) agrees with the results of the photomicrograph
measurements. An ATJ-S roughness height of 0.5 mil is therefore recom-
mended for use with the newly developed correlation in the absence of
data on a specific material sample.

It cannot be overemphasized, however, that for each flight or
ground test of graphite, a similarly-prepared specimen, which has been
subjected to laminar ablation should be used to determine the specific
roughness for that particular case. An accurate roughness height
measurement is particularly important because nosetip transition onset
is quite sensitive to laminar roughness. Figure 6-2 illustrates this
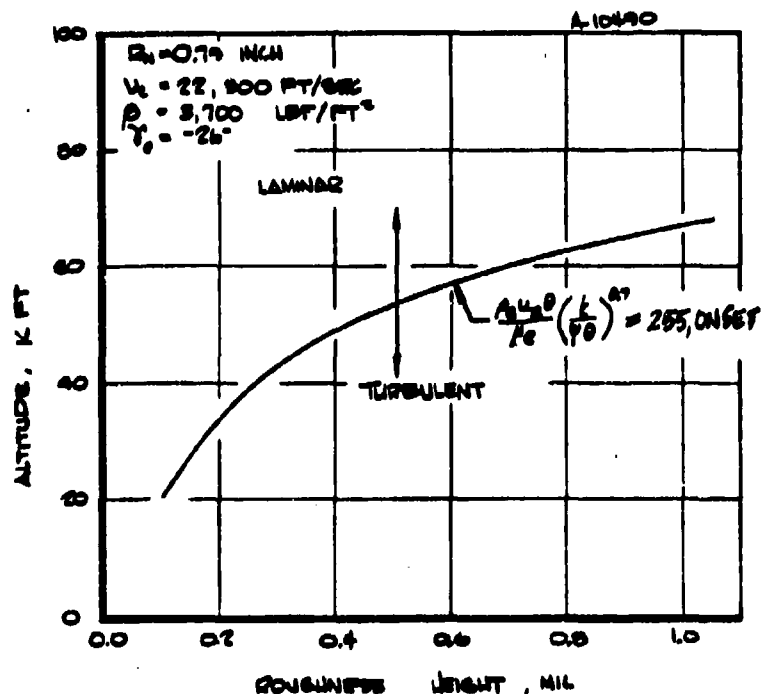
Figure 6-2. Transition Altitude as a Function of Roughness Height
for a Typical ICBM Trajectory

sensitivity for a typical ICBM trajectory and nosetip geometry. A
factor of 2 decrease in roughness will decrease the transition altitude
by approximately 15,000 feet. In general, this would significantly
reduce nosetip recession.

6.2   IMPROVED MODELING OF TURBULENT HEAT TRANSFER

Transitional and turbulent Stanton numbers are computed using
Reynolds analogy applied to the results of streamwise integrations of
the integral momentum equation. For rough surfaces, these heating
rates are modified to account for roughness augmentation. Ablation
effects are decoupled; that is, blowing corrections are computed after
the nonablating solution has been generated.

Two aspects of the technique used in the computation of turbu-
lent heat transfer are discussed in this section. In Section 6.2.1,
implementation of the Crowell composite heating model (Reference 6-3)
is described. This model provides a realistic low Reynolds number
limit to the turbulent heat transfer. Section 6.2.2 treats the transi-
tional heating model. In Section 6.2.3, rough wall, fully-turbulent
heat transfer predictions are compared to rough wall calorimeter data.

6-5

6.2.1 Crowell Composite Heating Modification

Previous to this modification, turbulent heat transfer was predicted to be zero at the stagnation point and less than laminar heat transfer for momentum thickness Reynolds numbers below about 50. Thus, for transition at low Reynolds numbers, turbulent heat transfer predictions were physically unrealistic. In Reference 6-3, Crowell developed a composite skin friction expression which, when used in the streamwise integration of the integral momentum equation (and with Reynolds analogy), eliminated the low Reynolds number anomaly. The Reference 6-3 treatment was restricted to the constant property smooth wall case. It is extended herein to include the effects of variable properties and augmentation of heating caused by surface roughness.

The integral momentum equation may be written as

$$\frac{d}{ds}\left(\rho_e u_e \theta\right) = \frac{\tau_w}{u_e} - \rho_e u_e \theta \left[\frac{(1 + H)}{u_e}\frac{du_e}{ds} + \frac{1}{r}\frac{dr}{ds}\right] \qquad (6\text{-}4)$$

With edge conditions, skin friction (τ_w), and boundary layer shape friction (H) defined in terms of the other variables, Equation (6-4) can be integrated to determine the momentum thickness as a function of streamwise length, $\theta(s)$.

Crowells composite expression for constant property smooth wall skin friction is

$$\frac{\tau_w}{\rho u_e^2} = \frac{0.222}{Re_\theta} + \left(\frac{Re_\theta}{100 + Re_\theta}\right)\frac{0.0128}{Re_\theta^{1/4}} \qquad (6\text{-}5)$$

This is shown in Figure 6-3 compared to the laminar and turbulent expressions to which it is asymptotic. For $Re_\theta \geq 200$, the composite expression is within 1 percent of the turbulent skin friction. However, the contribution of the first (laminar) term does not decrease as rapidly as it probably should, still being 10 percent at $Re_\theta = 1000$.

In the formulation used in nosetip analyses turbulent variable property effects are modeled via Eckert reference enthalpy properties (see Reference 6-4). The reference enthalpy is defined as

$$\bar{h} = 0.5\ h_w + 0.3\ h_e + 0.2\ h_o \qquad (6\text{-}6)$$
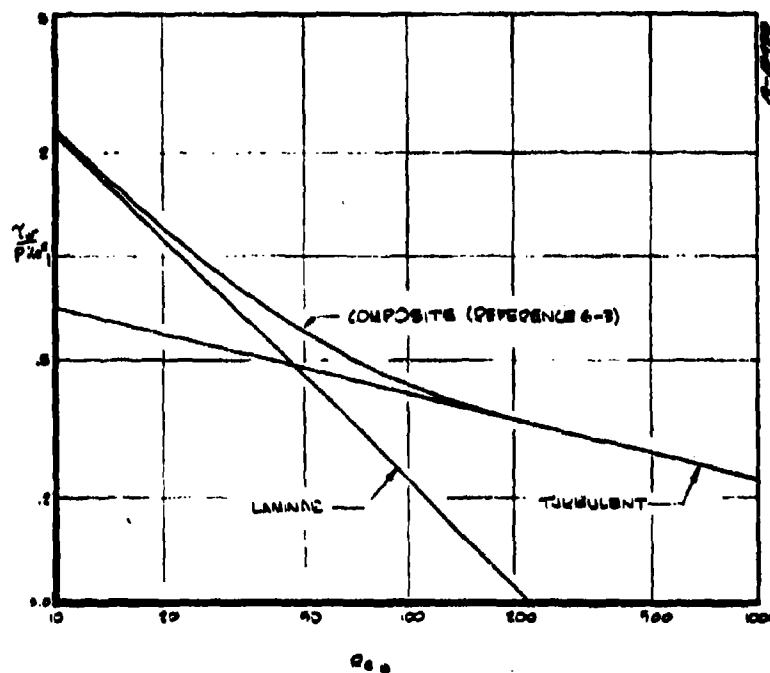
Figure 6-3. Composite Skin Friction

so that the reference properties are

$$\overline{\rho}(\overline{h},\ p) \quad \text{and} \quad \overline{\mu}(\overline{h},\ p)$$

with

$$\widetilde{Re}_\theta = \frac{\overline{\rho}u_e\theta}{\overline{\mu}}$$

In the dimensional form used in the momentum equation, the variable property composite skin friction is written as

$$\frac{\tau_{w,C}}{u_e} = \frac{0.222\ \mu_e}{\theta} + \frac{\widetilde{Re}_\theta}{100 + \widetilde{Re}_\theta}\ \frac{\tau_{w,T}}{u_e} \tag{6-7}$$

where

$$\frac{\tau_{w,T}}{u_e} = \frac{0.0128\ \overline{\rho}u_e}{\widetilde{Re}_\theta^{\,0.25}}$$

6-7

The reference viscosity is not used in the laminar term because use of
the edge viscosity yields a more accurate momentum thickness and heat
transfer prediction at the stagnation point.

The shape factor, $H = \delta^*/\theta$, remains to be specified before solu-
tion of the integral momentum equations can proceed. For wall cooling
ratios of greatest interest, $0.4 < T_w/T_e < 0.6$, the shape factor is in
the range, $0 < H < 1.0$. The solution of the integral momentum equation
is not particularly sensitive to variations in the shape factor and
previous versions of the code used $H = -1$ in order to allow closed form
integration. In addition to its direct influence in the integration of
the momentum equation, H affects the value of the composite momentum
thickness at the stagnation point, the composite momentum equation at
the stagnation point reduces to

$$\theta_C(0) = \frac{1}{3} \sqrt{\frac{2\mu_e}{(3 + H)\rho_e (du_e/ds)}} \qquad (6-8)$$

It is not possible to impose an initial condition, other than this, on
the momentum equation. Ideally, $\theta_C(0)$ should be the same as the laminar
momentum thickness calculated by the code, which is

$$\theta_L(0) = \frac{1}{3} \sqrt{\frac{\mu_e}{\rho_e (du_e/ds)}} \qquad (6-9)$$

The ratio of the two stagnation point momentum thicknesses is

$$\frac{\theta_C(0)}{\theta_L(0)} = \sqrt{\frac{2}{3 + H}} \qquad (6-10)$$

In order to have a realistic initial condition for the momentum thickness
and in keeping with previous versions of the code, a constant shape
factor, $H = -1$, is assumed in the integration of the composite momentum
equation.

Integration of the momentum equation using the above provides a fully turbulent, smooth wall solution for the momentum thickness distribution around the body. The composite smooth wall skin friction is also computed during the integration process, so that application of Reynolds analogy will determine the smooth wall heat transfer.

A laminar Reynolds analogy factor, R_L, is applied to the laminar contribution to the composite skin friction (Equation (6-7)). This factor is used to match the composite heat transfer at the stagnation point to the Fay and Riddell (Reference 6-5) prediction used in the laminar part of the code, so that

$$R_L = \frac{\rho_e u_e C_{H,L}(0)\,\theta(0)}{0.222\mu_e} \qquad (6\text{-}11)$$

The turbulent Reynolds analogy factor, R_T, is currently taken to be unity over the entire body. There is, however, some evidence from turbulent boundary layer solutions[*] that R_T is a function of pressure gradient, being about 0.95 on the nose and about 1.15 on the cone.

The smooth wall composite heat transfer becomes

$$\rho_e u_e C_{H,C,S} = R_L\,\frac{0.222\mu_e}{\theta} + R_T\,\frac{\overline{Re}_\theta}{100 + \overline{Re}_\theta}\,\tau_{w,T} \qquad (6\text{-}12)$$

Surface roughness, if sufficiently large, increases laminar as well as turbulent heat transfer. These effects are modeled using the augmentation factors developed in Reference 6-6. The laminar augmentation factor, F_L, is the ratio of laminar rough surface heat transfer to laminar smooth surface heat transfer, both for the same environmental and surface temperature conditions. The turbulent augmentation factor, F_T, is the ratio of heat transfer to rough and smooth walls in fully developed turbulent flow. In order to insure that the turbulent augmentation factor becomes dominant as the composite skin friction approaches turbulent skin friction the augmentation factors are applied as shown below.

$$\rho_e u_e C_{H,C,R} = F_L\left(R_L\,\frac{0.222\mu_e}{\theta} - \frac{R_T\,100}{100 + \overline{Re}_\theta}\,\tau_{w,T}\right) + F_T R_T \tau_{w,T} \qquad (6\text{-}13)$$

---

[*]Boundary Layer Integral Matrix Procedure (BLIMP) code.

If the augmentation factors were applied in the more obvious way, the influence of the laminar augmentation factor would persist past the $\overline{Re}_\theta$ where the flow would be turbulent. This is especially significant for very large roughness and for weather erosion calculations.

For very large roughnesses the rough wall composite heat transfer as computed from Equation (6-13) falls below the rough wall laminar prediction in a small region near the stagnation point. When this occurs, the composite heat transfer is set equal to the laminar heat transfer.

6.2.2 Transitional Heating Model

In the region downstream of the transition point, the heat transfer is calculated according to the Persh transitional heating model (see Reference 6-7). The transitional Stanton number is expressed as

$$C_{H,T,R} = C_{H,C,R} - \frac{A}{Re_\theta^2} \qquad (6-14)$$

The constant, A, is chosen so that the Stanton number is continuous.

This transitional heating model is somewhat simpler than the model which was in the code prior to the current effort. As will be seen from the examples in the next section, the present model yields quite reasonable predictions for rough wall calorimeters. These predictions are better than those made with the previous, more complicated, model. Further refinements would be justifiable only in conjunction with an improved understanding of rough surface heating augmentation.

6.2.3 Comparison of the Composite and Transitional Predictions to Rough Wall Calorimeter Data

Rough wall calorimeter data from Series A and Series J tests are shown compared to predictions in Figures 6-4a through 6-4f. These figures include examples for roughness heights of 0.6, 3.5, and 40.0 mils; nose radii of 1.5, 2.5, and 3.5 inches; with wall cooling ratios in the range $0.43 < T_w/T_e < 0.74$.

Figures 6-4a and 6-4b show two examples from Series A with small and large roughnesses. For Run 105, transition is predicted slightly aft of its actual position which results in a slight underprediction of peak heating. For Run 174, the actual roughness augmentation of peak turbulent heating is slightly larger than predicted. Some relaminarization (not modeled in the present code) is evident in the region of the cone tangent point. Both Series A examples show an accurate prediction of turbulent heating on the cone.
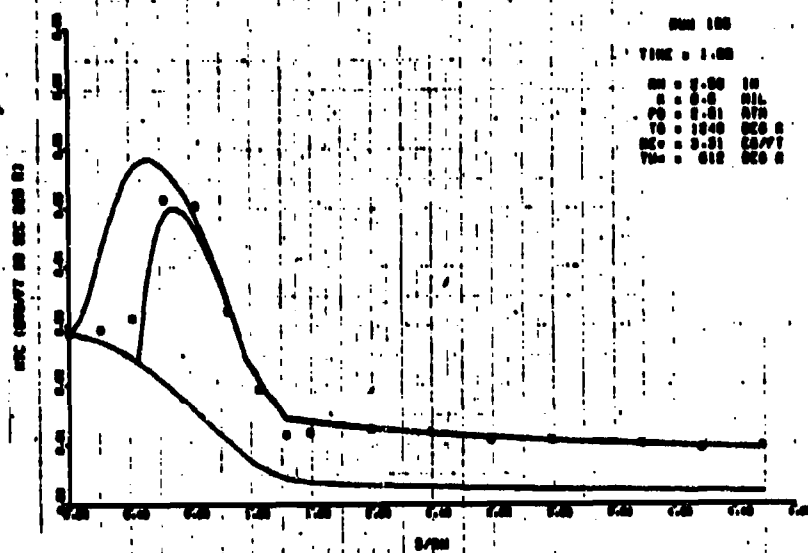
(a) Series A, Run 105
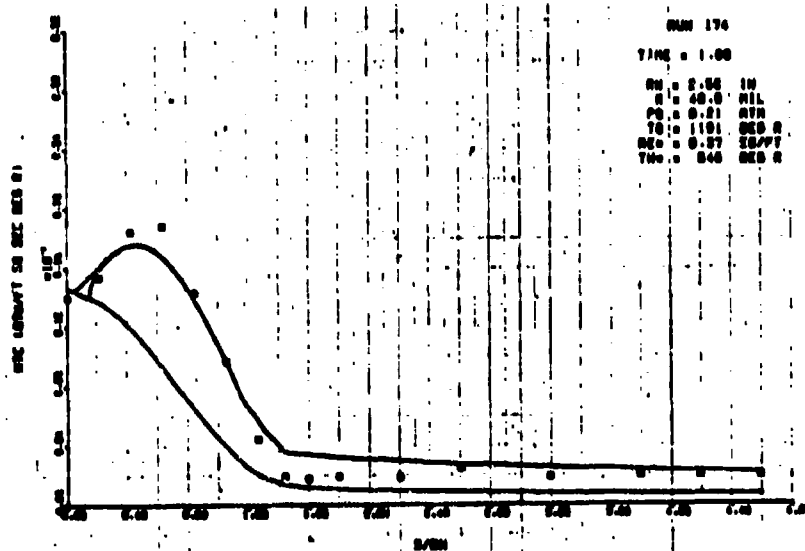
(b) Series A, Run 174

Figure 6-4. Turbulent and Transitional Heating Comparisons
Compared to Calorimeter Data

6-11
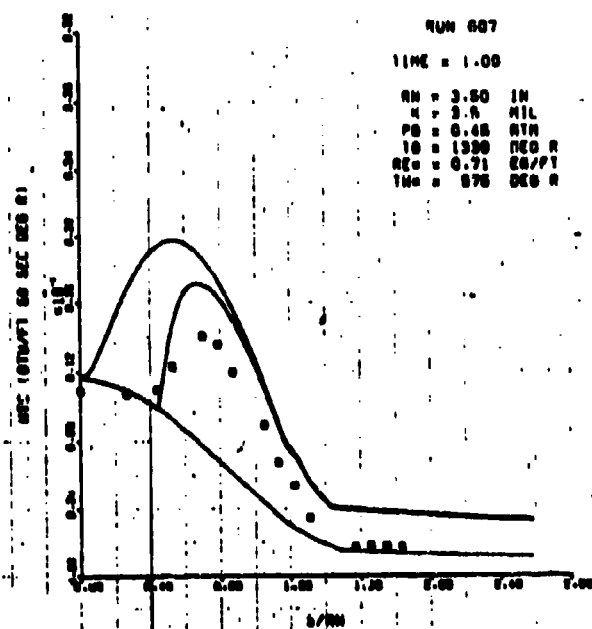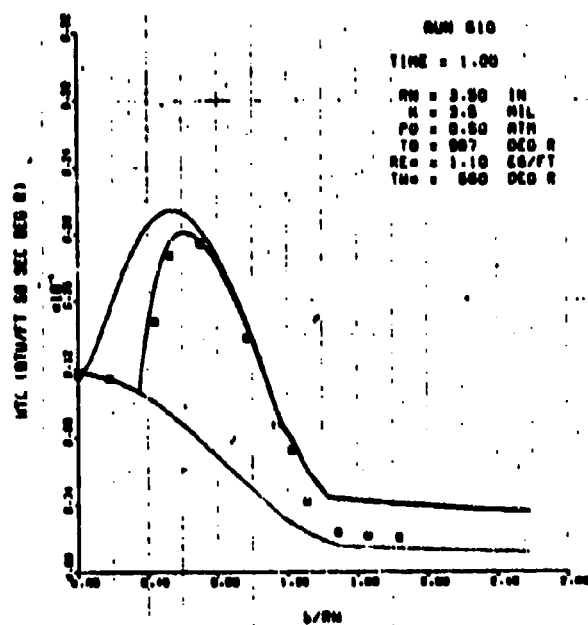
(c)   Series J, Run 607

(d)   Series J, Run 610

Figure 6-4.   Continued

6-12
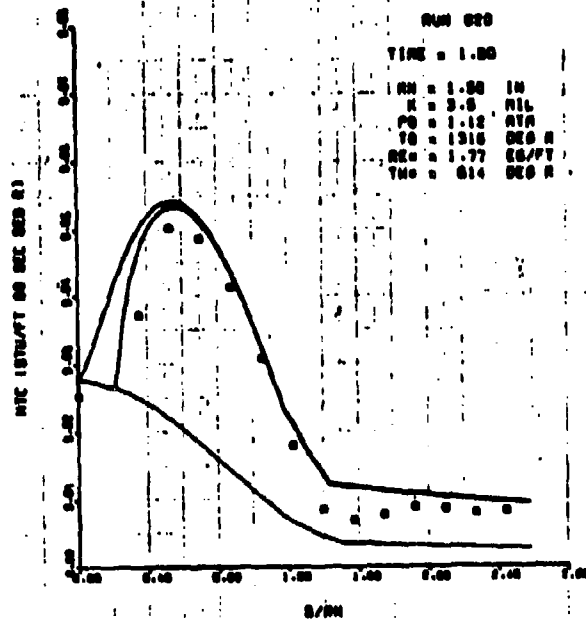
(e)   Series J, Run 620, Early Time
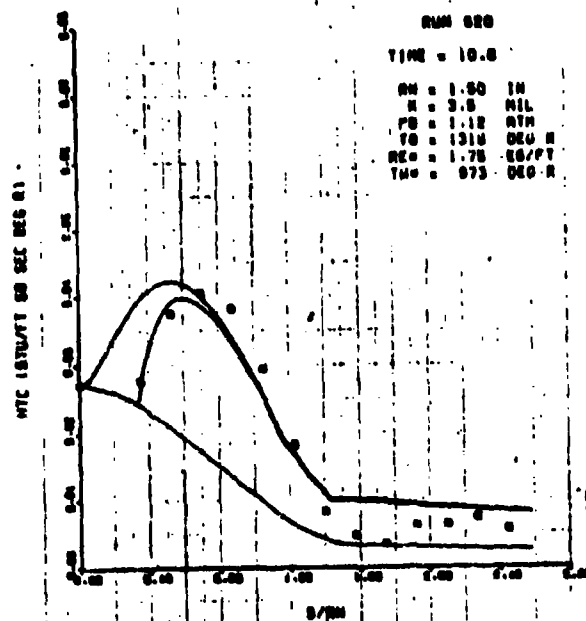
(f)   Series J, Run 620, Late Time

Figure 6-4.   Concluded

The next four figures show examples from Series J, all for a roughness height of 3.5 mils. Figures 6-4c and 6-4d are for the 3.5-inch nose radius model. The overprediction of transitional heating for Run 607 is not unique to this calorimeter. This was observed on several runs for which transition occurred downstream of $s/R_N > 0.4$. Evidently, the same forces which promote relaminiarization on the aft spherical surface inhibit turbulence growth. Run 610 is included as an example of the runs for which the total temperature was low. Agreement of the prediction with the data is quite good. Both Runs 607 and 610 show significant relaminarization.

Figures 6-4e and 6-4f show data and predictions for the 1.5-inch nose radius model. These examples are for Run 620 at test times of 1 and 10 seconds. At 1 second, transition is predicted slightly ahead of its actual position leading to a mild overprediction of peak heating. At 10 seconds, transition is accurately predicted but the composite model underpredicts peak heating. This is probably an indication that the dependence of the turbulent roughness augmentation factors upon wall cooling ratio is somewhat in error. Because of the small nose radius, significant relaminarization is present in spite of the relatively high unit Reynolds number of this example.

In general, transition location and transitional heating are quite well predicted for the rough wall calorimeters. Heating distributions for transition positions between $s/R_N = 0.4$ and the sonic point are not well predicted. Modeling of relaminarization is lacking.

6.3   SHAPE CHANGE MECHANICS

A critically important aspect of nosetip ablative response modeling is the technique used to numerically describe the instantaneous shape of the nosetip at any computational time step. The shape definition is most difficult in the stagnation region of shapes which exhibit a sharpened, biconic or slender cone stagnation region. During the PANT program numerous techniques for modeling the shape have been studied; but no totally satisfactory technique has been identified to date. In this section, the various techniques are described.

The problem is to represent the body shape (local surface coordinates, slope, and curvature) using information at finite nodal locations. The complexity of the interacting phenomena and associated equations means that many of the important response parameters at the nodal locations must be computed explicitly. That is, information from the previous time step must be used to compute current time results. For example, local ablation rates at a particular time are applied in most shape change codes over a finite computation time step. Since criteria for explicit extrapolation of instantaneous results are difficult

to establish, numerical instabilities and oscillations can result. Furthermore, the number of surface nodal points which can economically be used in a shape change calculation is limited. The numerical techniques which circumvent the difficulties of shape description are here termed shape change numerics.

Table 6-1 summarizes the various numerical techniques incorporated in the nosetip design computer codes modified or generated during the PANT program. Only minor changes to the modeling of surface coordinate evaluation have occurred during the development of the PANT codes. Major modifications have been associated with the evaluation of the local surface angle at the nodal coordinates. This aspect of the modeling is quite important because local pressures and, hence, heating rates are sensitive to the local surface inclination. The smoothing procedures incorporated in the SAANT and PAGAN computer codes provide analytically smooth surface angle distributions and eliminate coordinate location anomalies which develop from calculational inaccuracies. In the newly developed EROS computer code, nodal location adjustment is inconvenient because surface points are tied closely to the transient in-depth conduction grid. Thus, nodal point angles are determined so that numerical shape instabilities are suppressed. The technique is described in Reference 6-12.

Another area of shape change numerics which has been modified during the PANT program is the definition of body shape in the near stagnation region. During the PANT program nosetip recession was observed to produce nearly sharp biconic shapes. Modeling of such shapes required consideration of stagnation region shape details which were on a smaller dimensional scale than could be economically treated. Special nose geometry modeling procedures were developed to evaluate the instantaneous nose radius not from the nodal point locations, but from shape stability conditions. In the EROS code, the nose radius for sharp shapes is evaluated so that the stagnation point recession rate equals the axial recession rate of the first surface point which experiences turbulent flow.

6.4   BASELINE PREDICTION COMPARISONS

Current techniques for calculating the performance of a reentry vehicle nosetip require assumptions regarding various modeling techniques. The assumptions for which the predictions are sensitive are itemized below:

- The shock shape evaluation procedure affects the solution through the influence of vortical layer swallowing on the turbulent boundary layer.

- Local surface pressure modeling directly influences the heat transfer calculation.

TABLE 6-1

DEVELOPMENT OF SHAPE CHANGE NUMERICAL TECHNIQUES

Computer Code	Date	Surface Coordinate (R_i, Z_i) Definition	Surface Angle (θ_i) Definition	Special Stagnation Region Shape Modeling	Problems
COCAN (Ref. 6-8)	June 1971	Nodal points move normal to instantaneous surface $(-\Delta R_i = \Delta S_i \cos \theta_i, \Delta Z_i = \Delta S_i \sin \theta_i)$	Adjacent straight line angles averaged $\theta_i = (\theta_1 + \theta_2)/2$ $\theta_1 = \arctan(Z_i - Z_{i-1})/(R_i - R_{i-1})$ $\theta_2 = \arctan(Z_{i+1} - Z_i)/(R_{i+1} - R_i)$	None	Nodal points converge on centerline than slender or blunt biconic shapes occur
GRANT (Ref. 6-9)	Dec. 1971	Nodal points move on radial or axial grid lines $(-\Delta R_i = \Delta S_i/\cos \theta_i$ along Z_i, or $\Delta Z_i = \Delta S_i/\sin \theta_i$ along $R_i)$	Adjacent straight line angles averaged	None	Insufficient detail along stagnation line node overall prediction sensitive to grid spacing for biconic and slender shapes
SANT (Ref. 6-10)	June 1973	Nodal points move on axial grid lines only, with least squares adjustment to Z_i values each time step	Least-squares, splined quadratic curve fit of surface nodes	Nose radius computed from heating conditions to achieve stable shapes consistent with curve fit result	Least squares smoothing of nodal points violates mass and energy conservation; and stable nose radius calculation is sensitive to nose geometry assumptions and boundary layer inaccuracies
PAGAN (Ref. 6-11)	Jan. 1974	Nodal points move on axial or radial grid lines with least squares adjustments to coordinates (R_i, Z_i)	Least-squares, splined quadratic curve fit of surface nodes	Nose radius computed from heating conditions to achieve stable shapes consistent with curve fit result	Same as SANT; plus results sensitive to explicit grid front node dropping conduction scheme
ERDS (Ref. 6-12)	Mar. 1975	Nodal points move on rays emanating from fixed origin (origin in body for transient origin at ∞ for steady state solutions)	Angles defined from circle fits of adjacent points with adjustments to maintain shape stability	Radius of curvature computed so stagnation point recession equal to axial recession of adjacent body point	Overall response prediction may be sensitive to surface angle and stagnation region shape adjustments

- The assumed skin friction law used in the boundary layer momentum
  integral equation affects the heat transfer calculation.

- Assumed transition modeling including material assumptions such as
  the effective surface roughness is important.

- The correlation or correlations used to model the effects of surface
  micro- and macro-roughness on heat transfer significantly affect
  the response prediction.

- Current techniques employ relatively arbitrary specification of
  macro-roughness height and growth rate.

- Assumptions regarding heterogeneous surface reactions and surface
  sublimation are important because the thermochemistry models deter-
  mine the modeling of surface particulate removal that is required to
  match ablation data.

- The definition of the nosetip shape profile (i.e., point location
  and local slope) affects all subsequent calculations.

The above list represents those aspects of nosetip modeling which are less
than completely understood. Various theoretical and semi-empirical techniques
have provided valuable modeling guidance; however. Comparisons to available
flight data provide the ultimate validation of the analysis procedure. There-
fore, seven flight cases have been selected by SAMSO for evaluation of the
PANT developed computer code predictive techniques. These flight test cases
provide a wide range of reentry environments against which the merit of model-
ing assumptions may be assessed. Section 6.4.1 describes the baseline modeling
and corresponding flight predictions obtained at the start of the effort re-
ported herein, while Section 6.4.2 presents similar results obtained using
the current modeling updates.

6.4.1 SAANT Code Predictions

The SAANT computer code predictions were performed including the shock
shape, pressure, and skin friction correlations documented in Reference 6-10.
Also, the body curve-fit, smoothing option described in this reference was
used for the baseline predictions. The PANT rough wall nosetip transition
model based on displacement thickness was used; that is,

$$Re_k \left(\frac{s}{\delta^*} \right)^{1/3} = \begin{cases} 2000 \text{ location} \\ 2300 \text{ onset} \end{cases}$$

Since the transition criterion is roughness dependent, the correct microroughness must be specified in order to accurately predict transition onset and location. For the graphitic materials of interest, the appropriate effective microroughness for use with the above transition criterion is 0.4 mil (Reference 6-1). A different transition criterion was applied for locations aft of the nosetip shoulder. This cone transition criterion is described as:

$$Re_\theta = 275e^{0.114M_e} \quad \text{at transition}$$

where

M_e = edge Mach number

Both turbulent and laminar heating are augmented due to wall roughness by the technique described in Reference 6-6. In laminar flow, the material microroughness is utilized with the heating augmentation correlation. In turbulent flow regimes, it has been observed that scallops develop on homogeneous materials. The effective macroroughness (k) for scallops has been modeled in the baseline predictions as

$$k = 0.93P_{T_2}^{-0.77} \quad \text{inch}$$

where

P_{T_2} = stagnation pressure (psi)

Macroroughness growth is not modeled in the baseline predictions. However, downstream of the nosetip shoulder, the macroroughness is reduced to the microroughness value.

The thermochemical ablation response for the graphitic materials of interest was shown in Reference 6-1 to be accurately modeled by assuming equilibrium diffusion controlled oxidation and sublimation. The important species generated by heterogeneous surface reactions include CN, C_2N, C_2N_2, CO, and CO_2, NO, and N_2O, although the chemical species allowed in the modeling of carbon/air reactions are not restricted to these. Ground test evaluations using the equilibrium assumption have demonstrated that graphite ablation is accurately modeled assuming no mechanical mass removal. Consequently, the baseline flight predictions do not incorporate any particulate mass removal.

The trajectory and geometry parameters for the seven cases are presented in normalized form in Table 6-2. Stagnation point recession and shape profile histories are given in Figures 6-5a through 6-5g.

TABLE 6-2

TRAJECTORY AND GEOMETRY PARAMETERS

Case	R/R_{REF}	γ_e/γ_{REF}	V_e/V_{REF}	t_e^* (sec)	P_{max} (atm)
A	0.75	1.00	1.00	12.2	159
B	1.50	1.35	1.04	8.2	146
C	0.75	0.77	0.90	16.0	123
D	1.25	1.46	1.04	8.7	138
E	2.04	0.81	1.05	17.0	73
F	0.25	1.23	0.95	11.0	94
G	0.50	0.27	1.13	26.0**	110

*Time from 100 kft to LOS.

**LOS at 30 kft, all others at impact.

ALTITUDE
1. 150,000 FT
2. 42,600 FT
3. 24,500 FT
4. 15,400 FT
5. 6,600 FT

LENGTH/R$_{REF}$

RADIUS (R$_{REF}$)

Shape Profiles

(a) Case A

ALTITUDE (KFT)
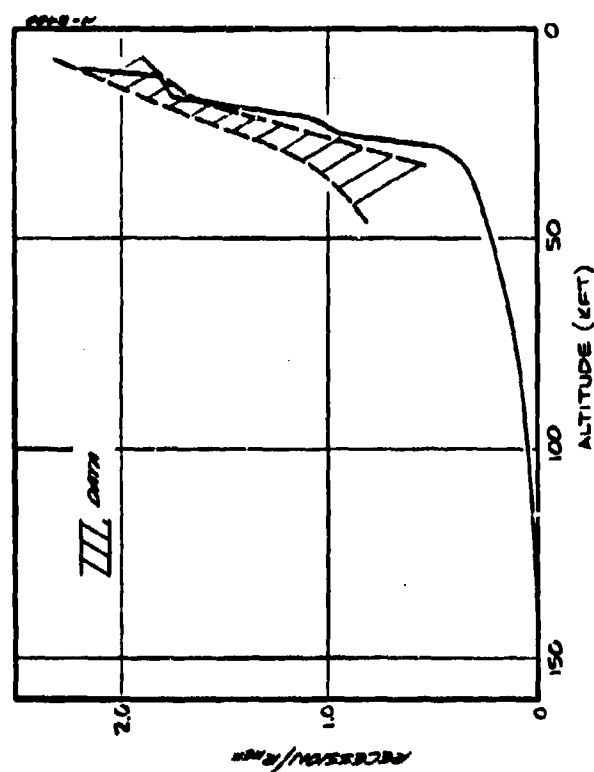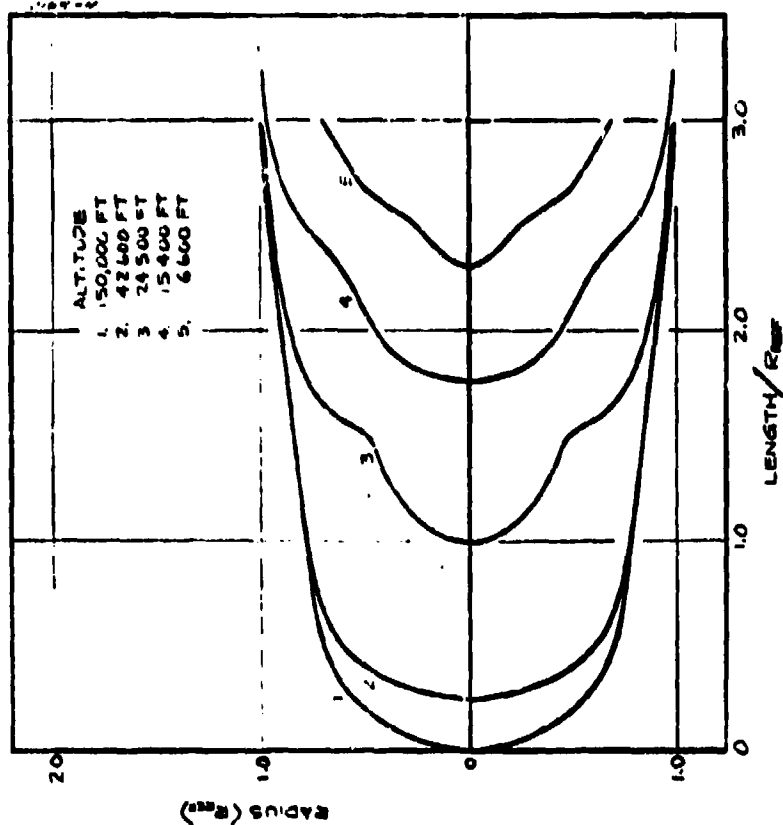
RECESSION/R$_{REF}$

Recession

Figure 6-5. Baseline SAANT Recession and Shape Predictions

Shape Profiles

Recession

(b) Case B

Figure 6-5. Cont'd

Shape Profiles

ALTITUDE
1 150,000 FT
2 41,400 FT
3 25,300 FT
4 15,700 FT
5 6,400 FT

LENGTH / R_{ref}

RADIUS / R_{ref}

Recession

ALTITUDE (KFT)

RECESSION / R_{ref}

ID DATA
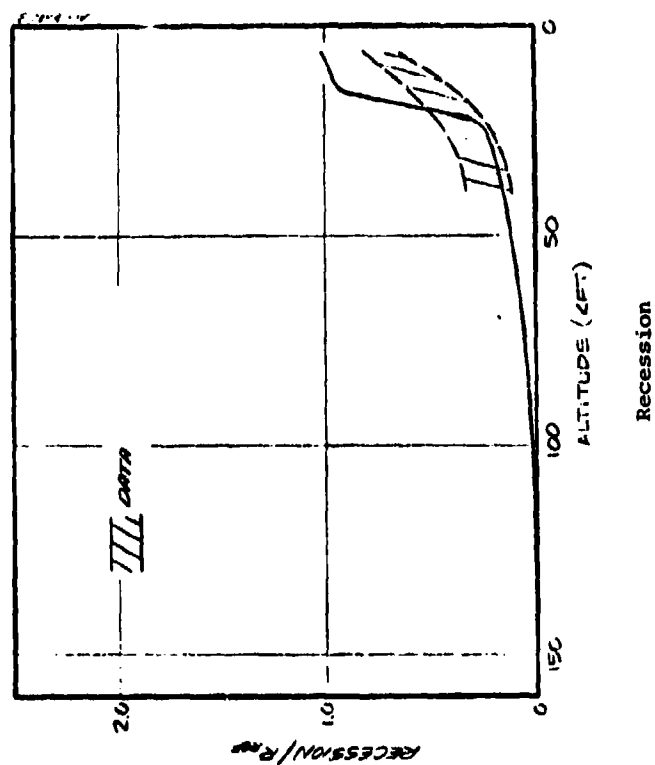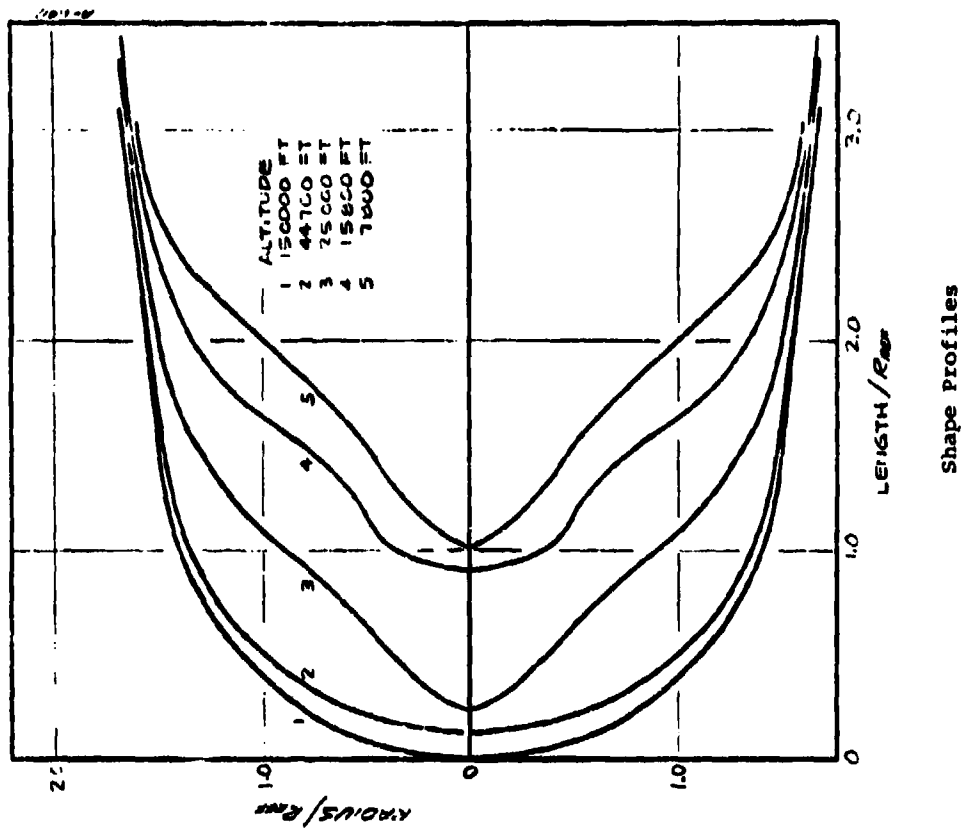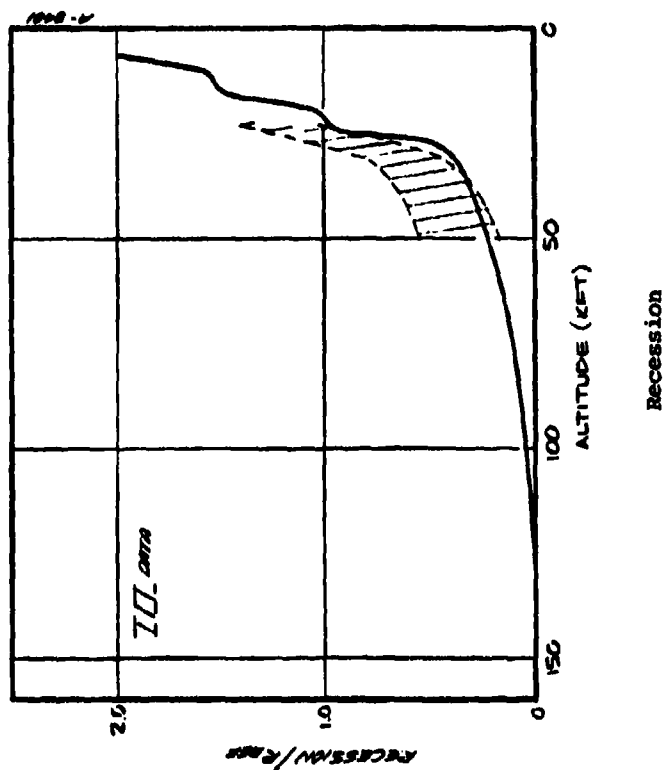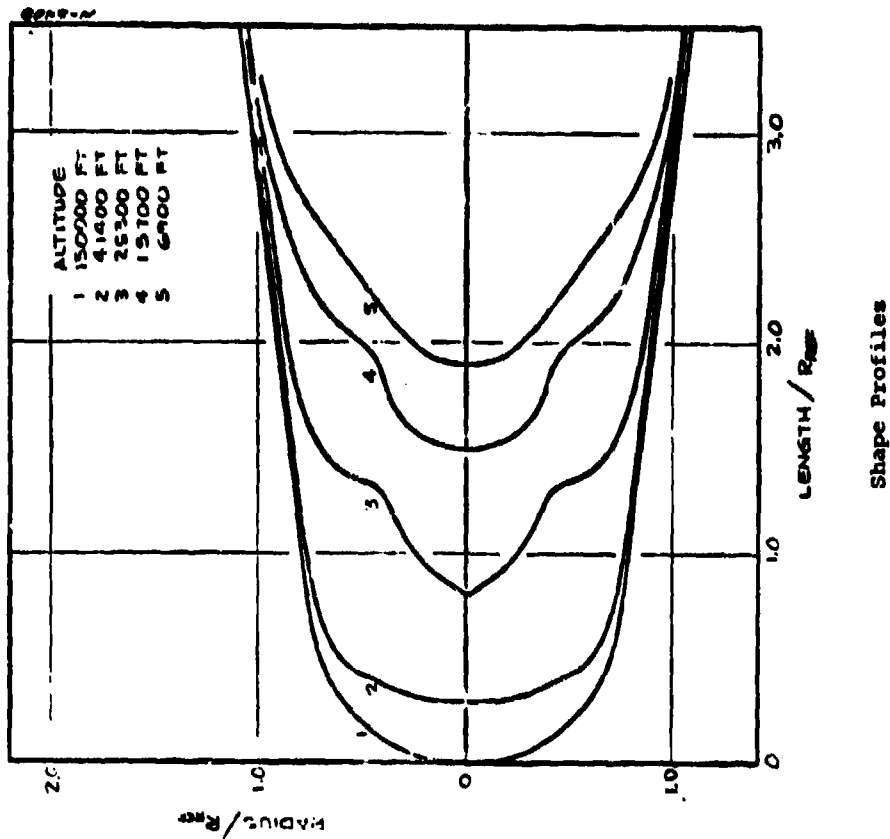
(c) Case C

Figure 6-5. Continued

Shape Profiles

Recession
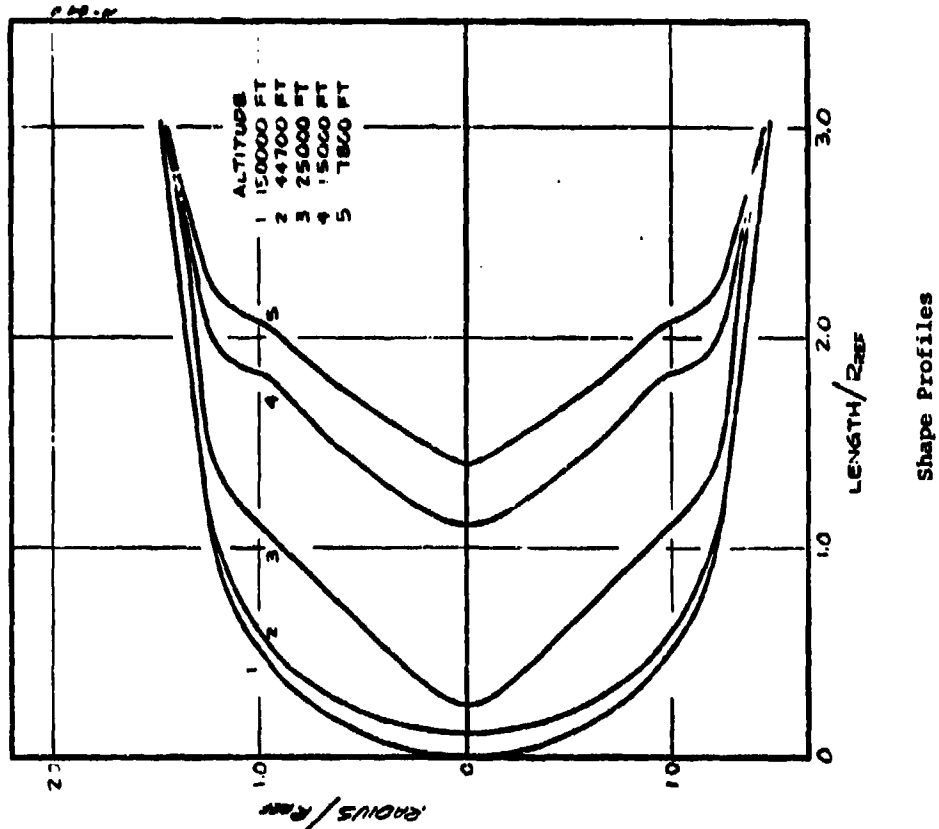
(d) Case D

Figure 6-5. Continued

Shape Profiles

Recession
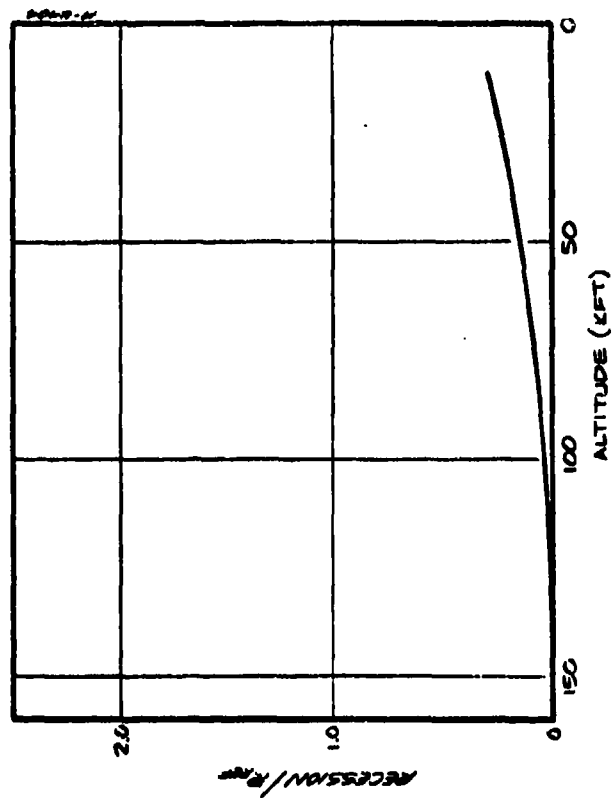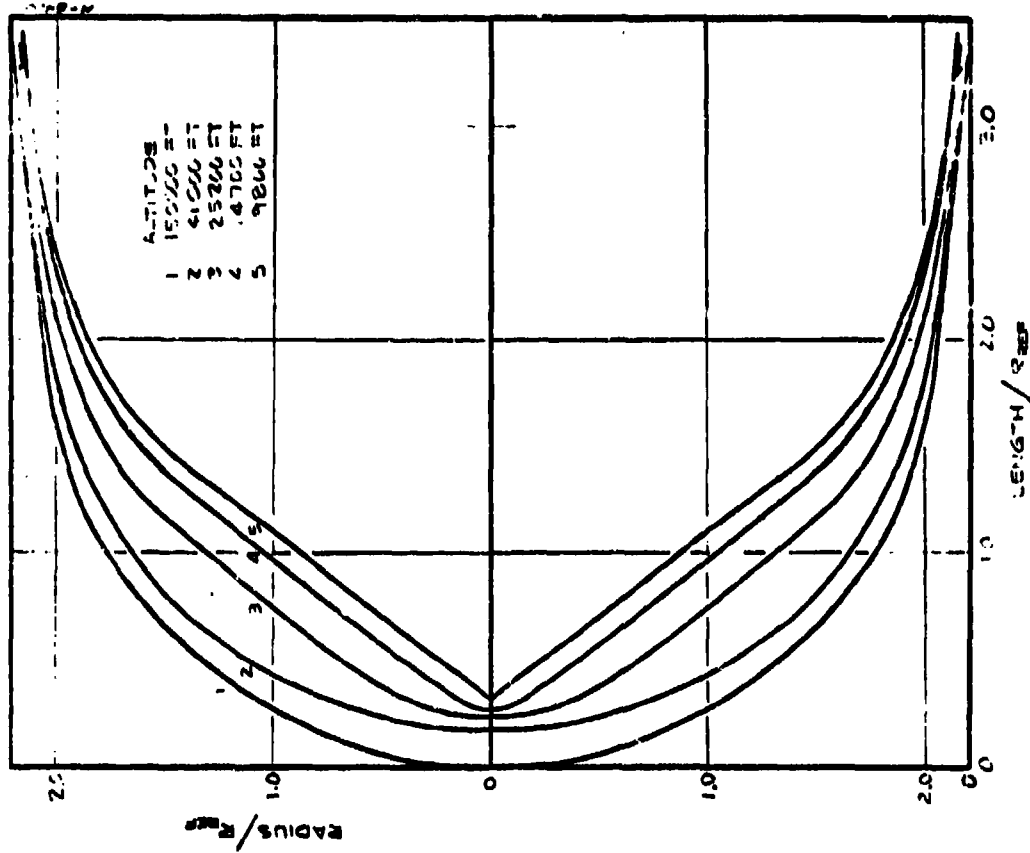
(e) Case E

Figure 6-5. Continued

6-24

Shape Profiles

Recession
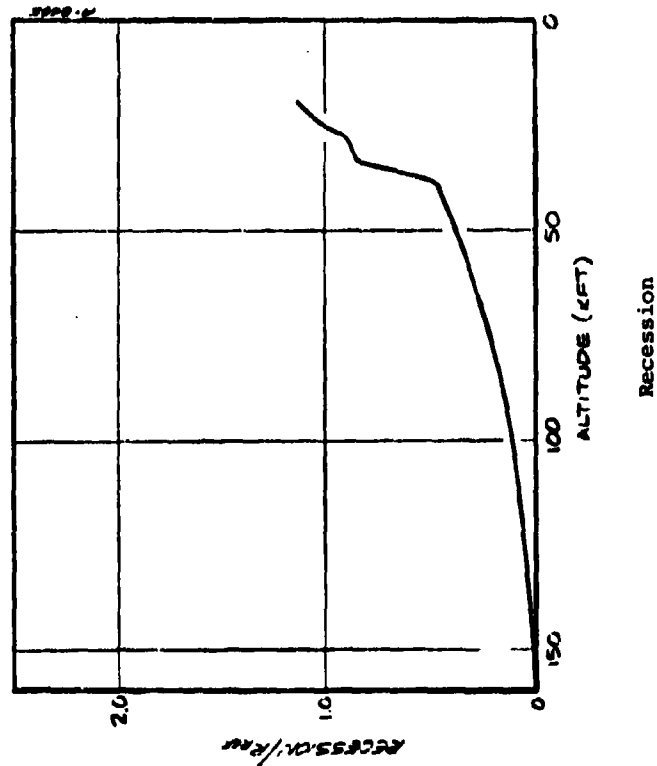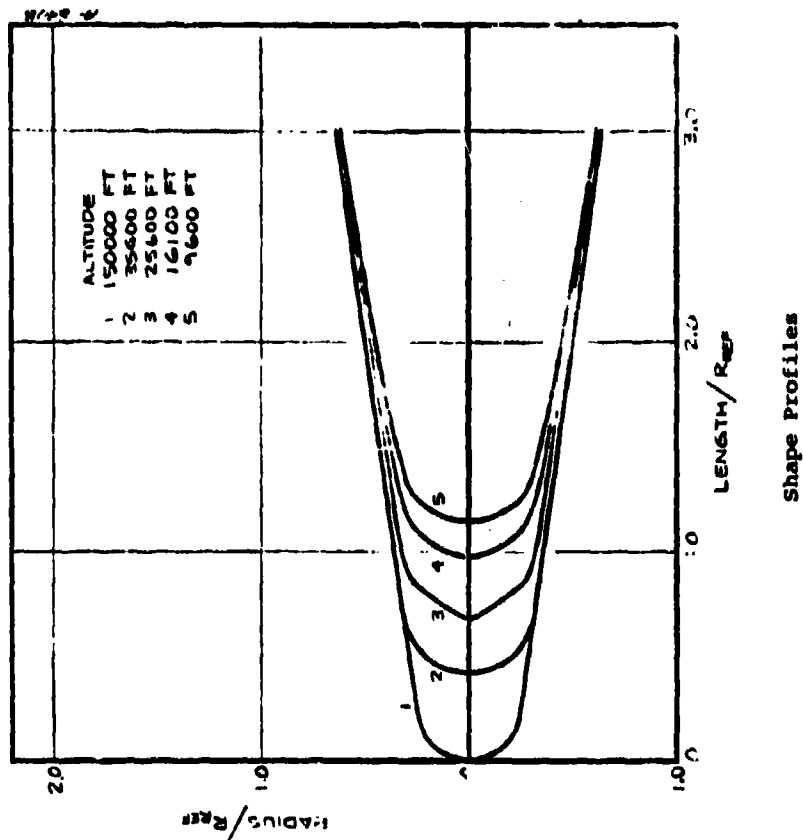
(f) Case F

Figure 6-5. Continued

Shape Profiles
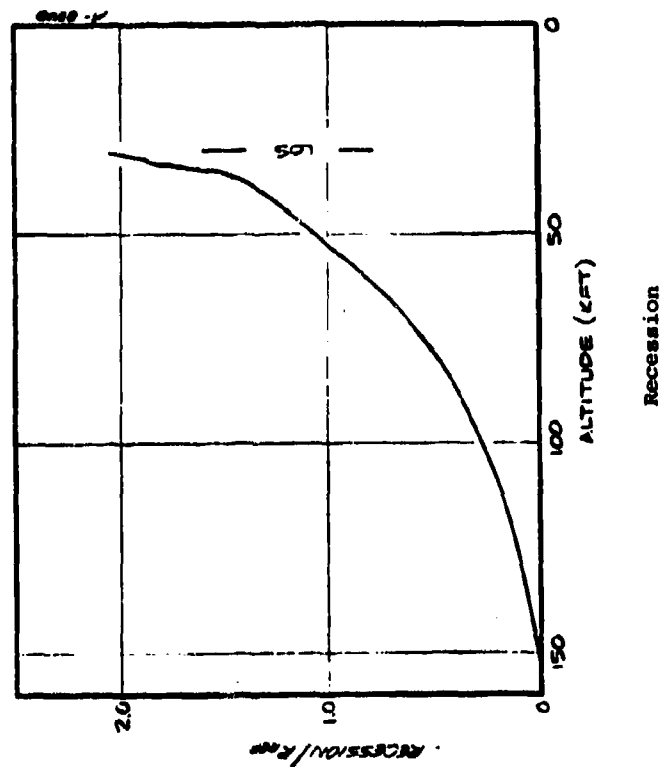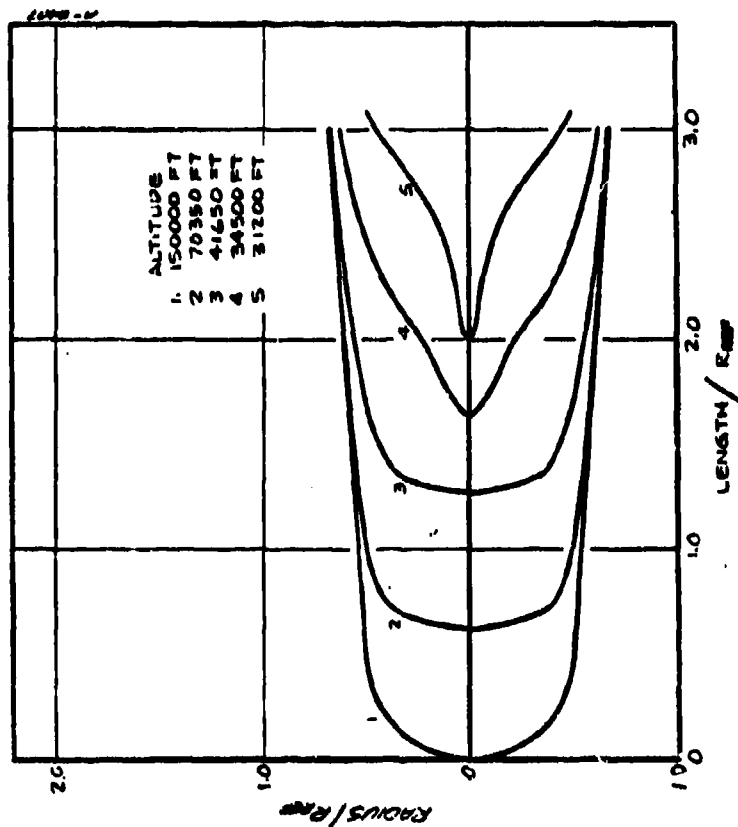
(g) Case G

Figure 6-5. Concluded

Recession

6.4.2 EROS Code Predictions

The EROS (Erosion Shape-Change) code was developed and documented under SAMSO/ABRES direction partially through a supplemental agreement to another contract effort. Code modifications described in Sections 6.1, 6.2, and 6.3 were included. The code changes defined under the supplemental tasks allowed modeling of the following:

- Continuum erosion mass loss
- Heating augmentation in erosive environments
- Shock layer effects on hydrometeor particle breakup and demise.
- Improved shock shape evaluation techniques
- Transient heat conduction via DuFort-Frankel scheme

Of these changes only the shock shape modeling would affect the clear air, steady-state ablation solutions for the seven baseline cases. The upgraded shock shape model is described in Reference 6-13.

The modeling changes described in Sections 6.1, 6.2, and 6.3, which affect clear air recession, may be summarized as follows:

- Transition onset and location as affected by blowing and dissociation (6.1)
- Turbulent heat transfer formulation (6.2)
- Shape change numerics (6.3)

Note that to assess the effect of the transition model change, the EROS solutions were obtained using the same microroughness for transition that was used in the SAANT solutions (0.4 mil). Thus, transition altitude changes are directly related to the criterion formulation change.

The only additional difference between the SAANT baseline solutions and the baseline solutions generated using the EROS code was associated with the selection of the turbulent macroroughness (scallop effect on heat transfer). The Series H data presented in Section 3 showed that the use of actual scallop dimensions in the sandgrain heating correlation significantly overpredicted data. In the absence of definitive data for the material of interest at flight conditions, a single turbulent region roughness was selected. The value for macroroughness (k_t) was taken to be

$$k_t = 0.001 \text{ inch}$$

For a stagnation pressure condition of 100 atm, the pressure dependent model used in the SAANT predictions gives

$$k_t = 0.003 \text{ inch}$$

The corresponding reduction in the rough wall turbulent heating factor is consistent with the Series H result.

Recession and shape profile histories from the EROS code predictions are given in Figure 6-6a through 6-6g. The SAANT baseline recession predictions are also shown in the respective figures. Table 6-3 presents a comparison of predicted nosetip transition onset altitudes using several transition criteria. Conclusions from the baseline predictions may be summarized as follows:

- Transition altitude is predicted slightly higher using the modified transition criterion.

- Transition altitudes are predicted lower than data from cases A, B (slightly), and C; higher than data from case D.

- Turbulent regime recession rate is predicted to be somewhat lower, consistent with the modified turbulent heating model and scallop effects modeling.

- Turbulent regime recession rates are in better agreement with data using EROS modeling.

- Stagnation point recession histories are more monotonic and realistic because of improved nose region numerics.

- EROS code shape profiles do not exhibit drastic inflection points and are generally more uniform with time than the SAANT results.
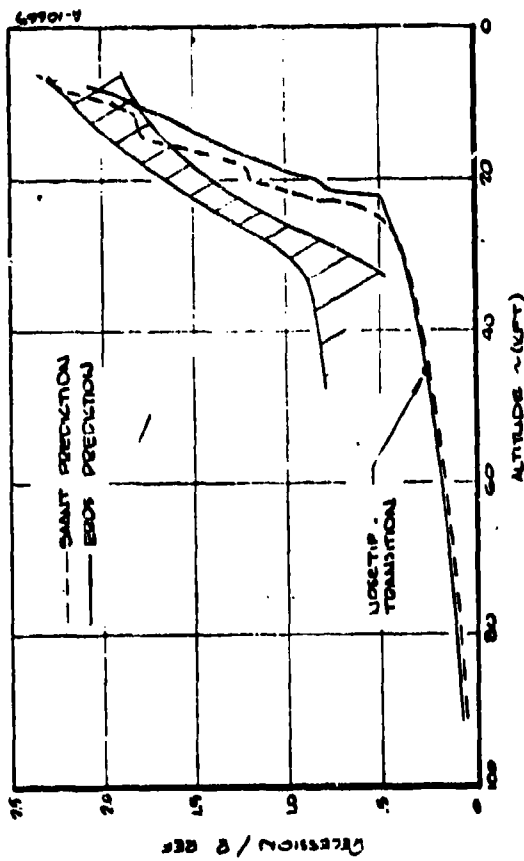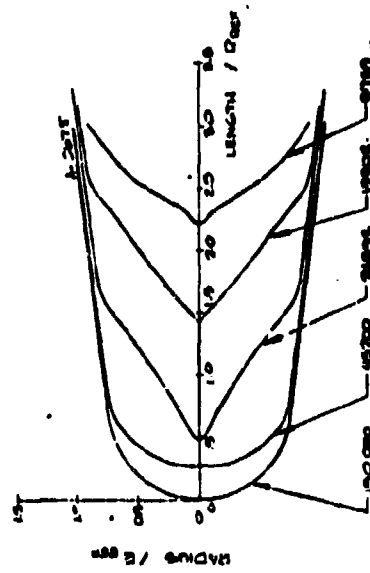
Shape Profiles

Recession

(a) Case A

Figure 6-6. Updated Shape Profile and Recession Histories
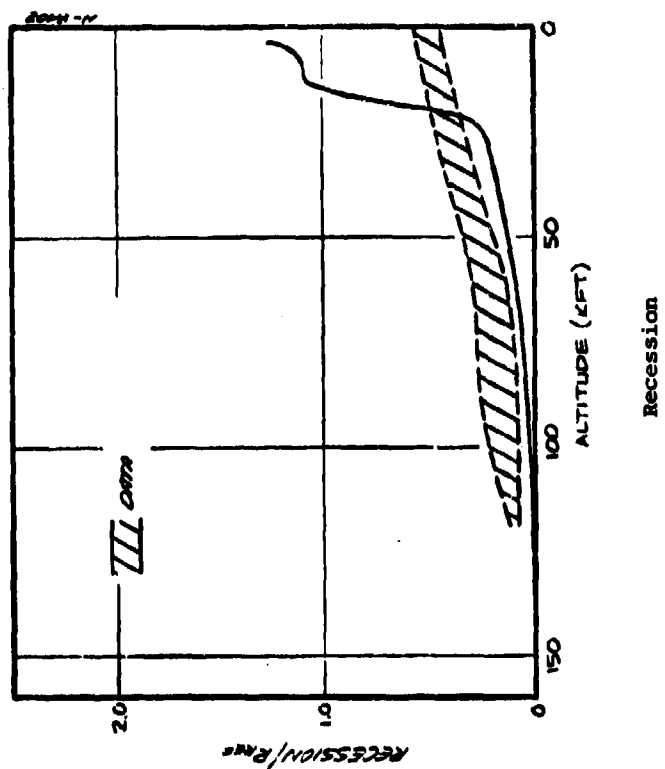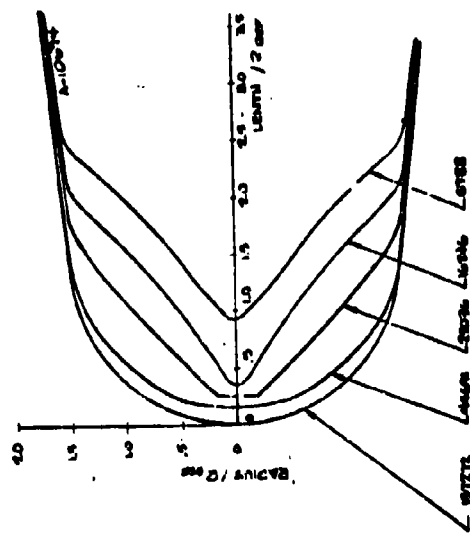
Shape Profiles
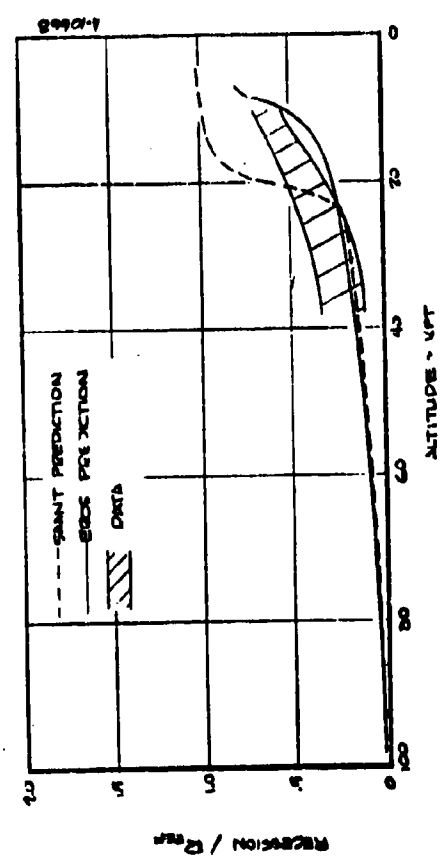
Recession

(b) Case B

Figure 6-6. Continued
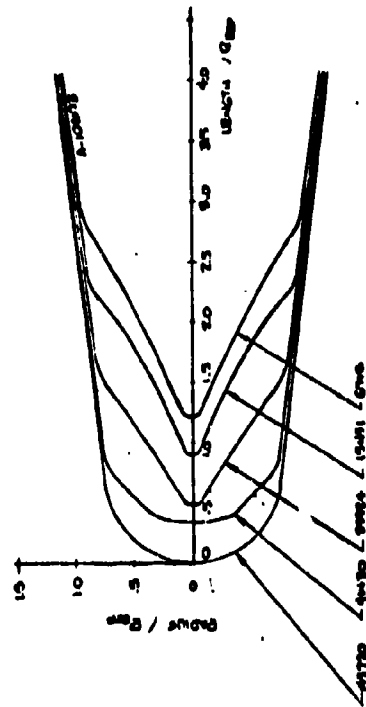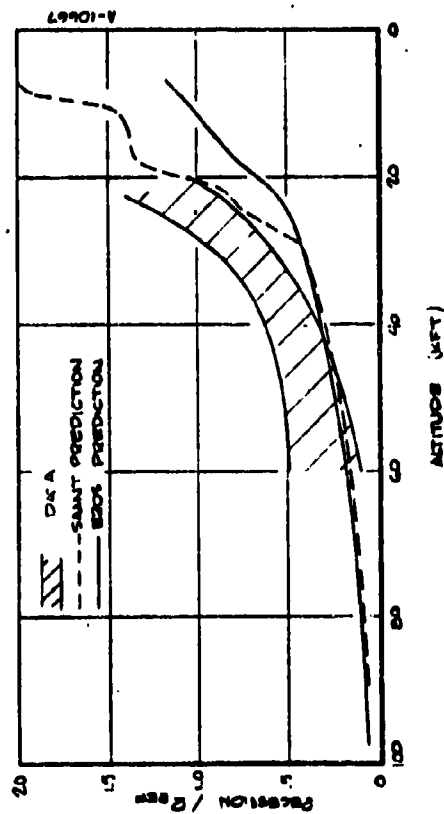
Shape Profiles

Recession

(c) Case C

Figure 6-6. Continued
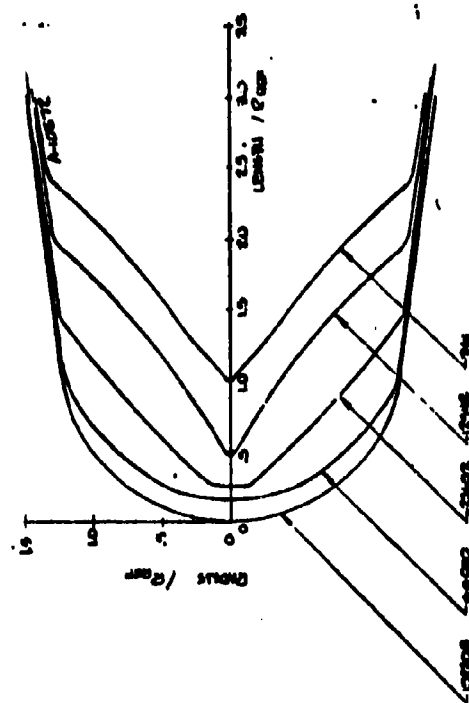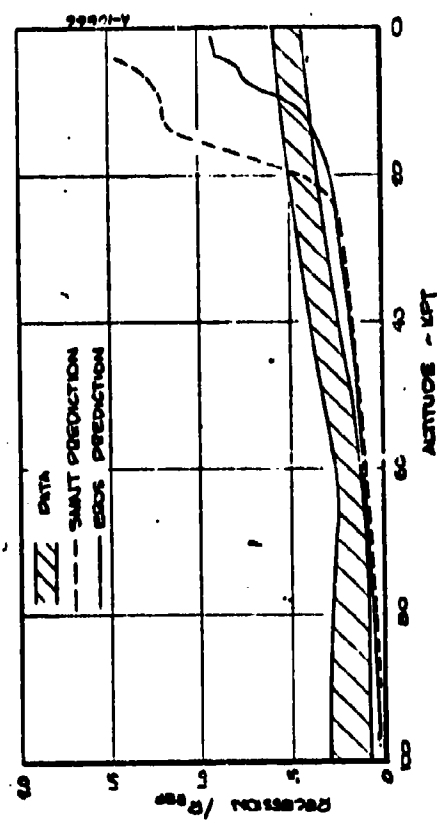
Shape Profiles

Recession

(d) Case D

Figure 6-6. Continued

Shape Profiles

Recession

(e) Case E

Figure 6-6. Continued

6-33
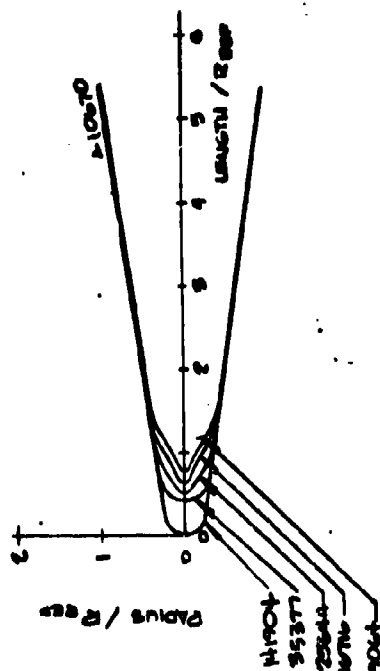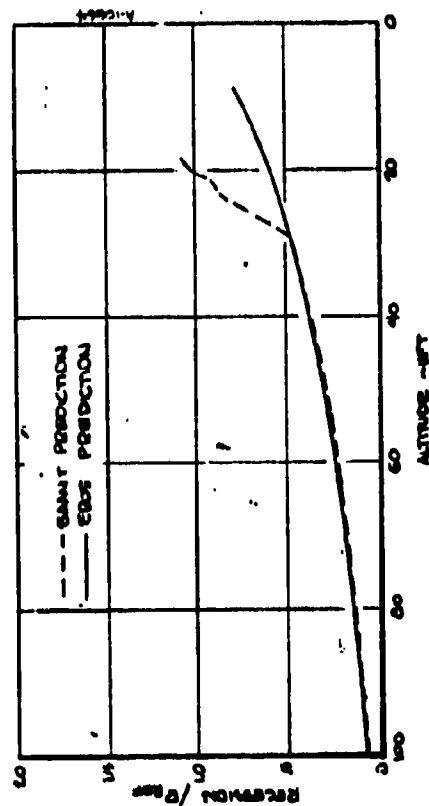
Shape Profiles

Recession

(f) Case F

Figure 6-6. Continued

Shape Profiles

Recession
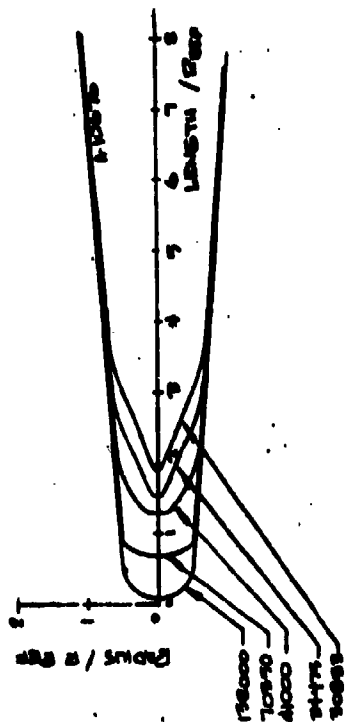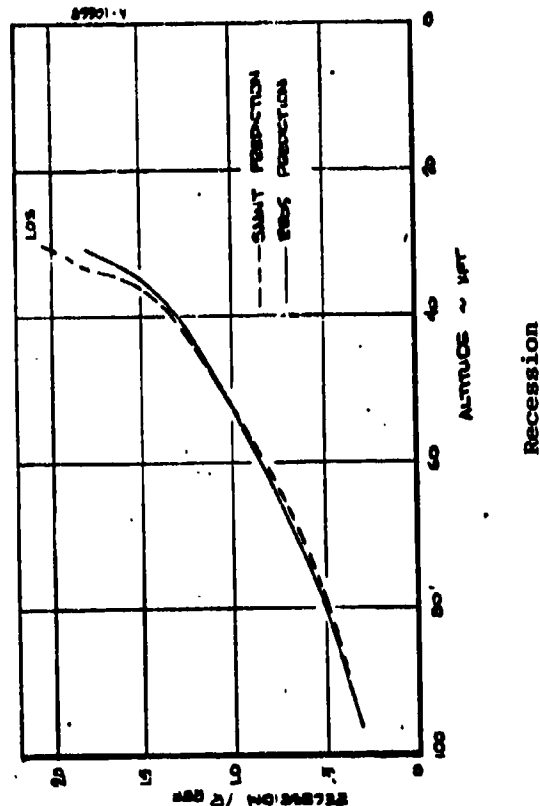
(g) Case G

Figure 6-6. Concluded

TABLE 6-3

SENSITIVITY TO TRANSITION CORRELATION

Sonic Point Transition Correlation	Predicted Sonic Point Transition* Onset Altitude (Kft)						
	A	B	C	D	E	F	G
$Re_k \left(\frac{S}{\delta^*}\right)^{1/2} = 2300$	43	45	41	44	43	36	42
$Re_\theta \left(\frac{k}{\theta} \frac{T_e}{T_w}\right)^{0.7} = 255$	47	51	44	49	48	37	44
$Re_\theta \left(\frac{k}{\psi\theta}\right)^{0.7} = 255$	45	49	45	49	48	48	45
$Re_k^* = 150$	49	49	48	49	48	48	49
$Re_\theta^* = 315^\dagger$	Lam	36	Lam	26	38	Lam	Lam

*$k = 0.4$ mil in all cases

$\dagger Re_\theta = 275e^{0.134M_e}$ for $M_e = 1.0$ (no rough wall effect)

SECTION 6 REFERENCES

6-1. Maurer, R. E., et al., "Passive Nosetip Technology (PANT) Program, Interim Report, Vol. VI — Graphite Ablation Data Correlation and Analysis," SAMSO TR-74-86, Aerotherm Report 74-90, Aerotherm Division/Acurex Corporation, January 1974.

6-2. Kratsch, K. M., et al., "Erosion Mechanisms and Improvement of Graphitic Materials, Vol. II — Hyperthermal Erosion Tests and Surface Roughness Characterization," AFML TR-70-307, McDonnell Douglas Astronautics Company-West, June 1972.

6-3. Crowell, P., "Turbulent Heating Near a Stagnation Point," Interoffice Correspondence, 73-5134.5-010, The Aerospace Corporation, March 19, 1973.

6-4. Eckert, E. R. G., "Survey on Heat Transfer at High Speeds," Report of Univ. of Minnesota, Minneapolis, Minn., 1961.

6-5. Fay, J. A. and Riddell, F. R., "Theory of Stagnation Point Heat Transfer in Dissociated Air," J. Aero. Sci., Vol. 25, 73-85, 121 (1958).

6-6. Powars, C. A., "Passive Nosetip Technology (PANT) Program, Interim Report, Vol. III — Surface Roughness Effects, Part II — Roughness Augmented Heating Data Correlation and Analysis," SAMSO TR-74-86, Aerotherm Report 74-90, Aerotherm Division/Acurex Corporation, January 1974.

6-7. Persh, J. R., "A Procedure for Calculating the Boundary Layer Development in the Region of Transition from Laminar to Turbulent Flow," NAVORD Report 4438, March 1957.

6-8. "Advanced Composites II (RESEP II), Vol. I, Computer User's Manual, Response of Charring Ablator Nosetips, Version 2," SAMSO TR-70-16, September 1969.

6-9. Nosetip Design Analysis and Test Program (NDAT), Computer User's Manual, GRANT-PLUG," SAMSO TR-71-147, June 1971.

6-10. Wool, M. R., Overly, P. T., and Derbidge, T. C., "Passive Nosetip Technology (PANT) Program, Interim Report, Vol. III — Computer User's Manual, Steady-State Analysis of Ablating Nosetips (SAANT) Program," SAMSO TR-74-86, Aerotherm Report 74-90, Aerotherm Division/Acurex Corporation, January 1974.

6-11. Wool, M. R., Overly, P. T., and Neuner, G. J., "Passive Nosetip Technology (PANT) Program, Interim Report, Vol. VIII — Computer User's Manual, Passive Graphite Ablating Nosetip (PAGAN) Program," SAMSO TR-74-86, Aerotherm Report 74-90, Aerotherm Divison/Acurex Corporation, January 1974.

6-12. Rafinejad, D. A. and Derbidge, T. C., "Passive Nosetip Technology (PANT) Program, Interim Report, Volume XVII - Computer User's Manual, EROsion Shape (EROS) Computer Code," SAMSO-TR-74-86, Aerotherm Report UM-74-57, Aerotherm Division, Acurex Corporation, Contract F04701-74-C-0069, CDRL B002, December 1974.

6-13. Berry, R. A., Lee, K. C., Kriebel, A. R., Nardo, C. T., and Wool, M. R., "Passive Nosetip Technology (PANT) Program, Interim Report, Volume XVI, Investigation of Erosion Mechanics on Reentry Materials (U)," SAMSO-TR-74-86, Aerotherm Report 75-139, Aerotherm Division/Acurex Corporation, Contract F04701-74-C-0069, CDRL B002, March 1975 (SECRET)

SECTION 7

CONCLUSIONS

The conclusions from the efforts summarized in this volume of the Interim Report for the Passive Nosetip Technology (PANT) program are itemized below:

1. The AFFDL 50 MW arc jet ablation tests of various size and shape nosetip models provided useful shape change and boundary layer transition data. The shape change response of the models was consistent with shape change events observed in numerous low-temperature ablator (LTA), wind tunnel tests.

2. In the AFFDL 50 MW arc tests, initial model configurations significantly affected the early time shape change and recession; however, once fully-turbulent profiles establaihed, recession rates equalised.

3. Heat transfer measurements from the nosetip replica calorimeter, which was tested in PANT wind tunnel Series H, provided useful data on the effects of surface scallops on nosetip response. Analysis of the data indicated the following:

    ●   Heat transfer rates to the scalloped surface calorimeter are significantly higher than the corresponding smooth surface predictions.

    ●   The measured heat transfer rates generally agree with heating rates inferred from the ablation rates of the replicated LTA model.

    ●   The roughness agumentation factor (ratio of actual to smooth wall) does not scale as indicated by the PANT sandgrain roughness effects correlation, as anticipated.

    ●   The augmentation factor at specific nosetip locations is nearly independent of free stream Reynolds number. Locations with larger roughness indicate greater augmentation.

- The scallop surface on the Series H calorimeter produces less heating augmentation than a sandgrain surface having a similar roughness height. Current equivalent-sandgrain models do not explain the differences.

4. The effects of nosetip configuration variations and trajectory dependent flow conditions on nosetip shape change were enumerated in the Series I Low-Temperature-Ablator (LTA) wind tunnel tests. These constant Reynolds number tests indicated that the Reynolds number condition for the irregular shape formation varies significantly with stream total temperature, initial nose radius, and surface roughness.

5. In the Series I tests, the formation of irregular shapes was accompanied by a significant increase in the vibrational accelerations associated with unstable or quasi-unsteady flow phenomena.

6. In the Series J wind tunnel tests, heat transfer data from roughened calorimeters, indicated the effects of body size and shape on boundary layer transition. Analysis showed that the transition data agreed with the PANT correlation developed earlier during the analysis of Series A, 2.5-inch nose radius, sphere/cone calorimeter data.

7. Detailed study of boundary layer profile calculations indicated that the boundary disturbance which initiates transition correlates with the relative flow kinetic energy at the top of a roughness element. Using this observation, the transition criterion was analytically extended to flight condition by including the dependence on ablation and species dissociation. Allowing for material surface roughness uncertainty, the upgraded transition model agrees with available flight nosetip transition data.

8. The turbulent heat transfer model in the PANT codes was upgraded to include a unified skin friction formulation which successfully eliminated low Reynolds number turbulent heat transfer prediction anomolies.

9. Seven flight test cases were analyzed to determine the effects of recent shape change modeling on calculated shape profiles and recession. It is concluded that the transition, heat transfer, and code numerics modeling changes improved the prediction capability, but the prediction of the irregular shape regime remains uncertain.

APPENDIX

**BOUNDARY LAYER TRANSITION ON NOSETIPS
WITH ROUGH SURFACES**

by
Aemer D. Anderson

February 15, 1975

LIST OF SYMBOLS

B'	dimensionless blowing rate
C_H	Stanton number
HTC	heat transfer coefficient
k	roughness height
M	Mach number or molecular weight
P	pressure
R_N	nose radius
r	normal distance from axis
Re_k	$\rho_e u_e k / \mu_e$
Re_θ	$\rho_e u_e \theta / \mu_e$
s	streamwise distance from the stagnation point
T	temperature
u	streamwise velocity component
v	normal velocity component
V	entry spped
y	normal distance from the surface
β	dimensionless velocity gradient or ballistic coefficient
γ	entry angle
δ^*	displacement thickness

LIST OF SYMBOLS (Concluded)

η	Levy-Lees normal coordinate
θ	momentum thickness
μ	dynamic viscosity
ν	kinematic viscosity
ξ	Levy-Lees streamwise coordinate
ρ	mass density
ψ	effective wall cooling ratio

Subscripts

e	boundary layer edge
k	top of roughness element
o	model stagnation condition or incompressible n
w	wall

Superscripts

*	sonic condition
'	fluctuation quantity
‒	average

A.1   INTRODUCTION

Rough wall transition studies were undertaken as part of the PANT program
in order to obtain a better understanding of boundary layer transition on graphitic
nosetips during reentry. Previous uncertainties in predicting when boundary layer
transition occurs ahead of the sonic point resulted in a factor of two uncertainty
in predicted nosetip recession. Nosetip shape change (and total recession) is very
sensitive to the onset of transition in the subsonic nose region but it also depends
on the location of transition in this region at lower altitudes.

This appendix is a summary of the experimental and theoretical program carried
out to address the problem of predicting rough wall transition in the subsonic region
of a graphitic nosetip.

In the remainder of this section, the flight transition environment and its
simulation in ground test facilities is discussed. Section A.2 summarizes the experi-
mental program which was comprised of two hypersonic wind tunnel test series utilizing
rough, nonporous, thin wall calorimeters. Transition data from these two series are
listed in Tables A-1 and A-2. Section A.3 treats the correlation of rough wall transi-
tion data. A modified relative roughness, $(T_e/T_w)(k/\theta)$, is identified as the distur-
bance parameter which correlates with the momentum thickness Reynolds number at transi-
tion. A separate correlation, utilizing the same parameters evalauted at the sonic
point, is presented for transition onset, that is, the condition for which transition
is incipient in the subsonic region of a rough nosetip. Section A.4 is concerned with
a theoretical extension of the experimental results to include the effects of mass
transfer and chemical reactions. The empirically established disturbance parameter,
$(T_e/T_w)(k/\theta)$, is shown to correlate with the relative kinetic energy at the top of
the roughness elements, $\rho_k u_k^2/\rho_e u_e^2$, which is hypothesized to be the key physical
measure of the disturbance.* The influence of blowing and chemical reaction on this
physical disturbance parameter, $\rho_k u_k^2/\rho_e u_e^2$, is then used to infer a modification of
the empirical disturbance parameter, $(T_e/T_w)(k/\theta)$, to account for these effects. This
modified empirical disturbance parameter replaces $(T_e/T_w)(k/\theta)$ in the transition cri-
terion.

A.1.1   Flight Transition Environment

Surface roughness may be expected to influence boundary layer transition unless
the roughness height is small in comparison to the boundary layer thickness. Current

---

*The ratio $\rho_k u_k^2/\rho_e u_e^2$ is the smooth wall kinetic energy at a distance of one roughness
height from the wall divided by the kinetic energy at the boundary layer edge. The
empirical disturbance parameter, $(T_e/T_w)(k/\theta)$, is retained in the prediction procedure
since knowledge of the values ρ_k and u_k requires detailed boundary layer profiles which
are not available in the shape change codes.

nosetip graphites have peak to valley surface roughnesses in the range 0.1 mil < k < 1.0 mil. For comparison with these roughnesses, the laminar sonic point momentum thickness distribution with altitude is shown in Figure A-1 for a 0.75-inch R_N sphere-cone nosetip during a typical ballistic reentry. Since the roughness is of the same order of magnitude as the momentum thickness, the influence of roughness must be taken into account when predicting boundary layer transition on graphite nosetips.

The momentum thickness Reynolds number, $Re_\theta = u_e\theta/\nu_e$, is the parameter usually considered to reflect the tendency of disturbances in a boundary layer to be ampli-fied into turbulence. This parameter, evaluated at the sonic point, is shown as a function of altitude in Figure A-1. If the nosetip had a perfectly smooth wall, boundary layer transition would be expected to occur ahead of the sonic point for $Re_\theta^* \approx 300$. Although this level is not attained on the "typical" 0.75-inch nose radius reentry body, roughness reduces the critical value of the momentum thickness Reynolds number required for transition. The results detailed in later sections indicate roughness induced transition on this nosetip for $k \geq 0.1$ mil.

Two other parameters are expected to influence nosetip boundary layer transi-tion; the wall cooling ratio, T_w/T_e, and the dimensionless blowing rate, $B' = \rho_w v_w/\rho_e u_e C_H$. Sonic point values of these parameters are shown in Figure A-1. The indicated levels of these parameters are typical of graphite ablation in flight.

A.1.2 Previous Data Base

Prior to the PANT program most sources of data on roughness induced transition were restricted to two-dimensional adiabatic flows with isolated roughness elements. These data sources are described by Anderson and Bartlett in a survey of the state of the art at the beginning of the PANT program (Reference A-1). There were a few sources which reported calorimeter data for the situation of primary interest, that is, uniform distributed roughness on a blunt axisymmetric body. Data from these sources were included in the analysis reported by Anderson (Reference A-2).

The paucity of pertinent data indicated a need for a comprehensive experimental program to provide an adequate collection of data on which to base nosetip transition criteria. Ideally, the parameters discussed in connection with Figure A-1 (i.e., k/θ, Re_θ, T_w/T_e, and B'), together with enthalpy and pressure levels typical of reentry would be closely approximated. Since all appropriate parameter variations cannot be simulated simultaneously in any ground test facility, some compromises were necessary. Three types of facilities were considered and these are discussed in the following section.

A.1.3 Candidate Ground Test Facilities

The ballistic range offers the closest simulation of the flight environment as graphitic models can be flown at reentry speeds and pressures. Because of the high
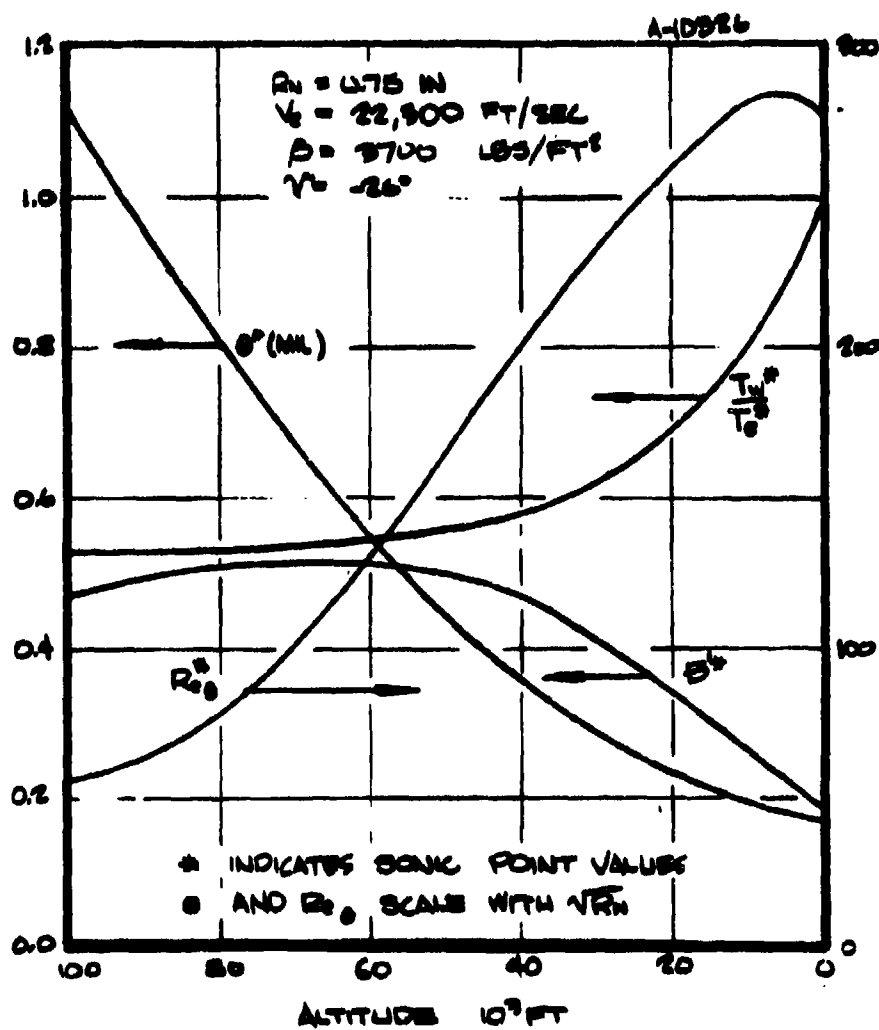
Figure A-1. Parameters influential to transition evaluated at
the sonic point (*) for a typical trajectory.
Laminar boundary layer flow assumed.

velocities and short test times, instrumentation is difficult; however, optical techniques are being developed. Model preheating and model recovery techniques are also being developed.

High power (50 MW) arcjets provide simulation of flight pressure levels and fairly high enthalpy levels in which to test graphite models. Tests may be run for several seconds at constant conditions. The primary shortcomings of this type of facility are the nonuniform enthalpy and entropy distributions in the stream and the high level of free-stream turbulence and contamination.

The hypersonic wind tunnel, although it operates at low pressure and enthalpy in comparison to flight, allows simulation of several of the most important dimensionless transition parameters. Using nonporous, thin wall, metal calorimeters with roughness heights of the order of 1 to 10 mils, the ranges of interest of the momentum thickness Reynolds number, the ratio of roughness height to momentum thickness (relative roughness) and the wall cooling ratio can all be simulated. The test stream is clean and well defined. Also, instrumentation is relatively straightforward and test times are conveniently long. For these reasons the hypersonic wind tunnel was chosen for the rough wall transition experiments. The effects of high enthalpy level and ablation are not simulated; however, as discussed in Section A.4, these effects may be treated theoretically.

After a survey of available wind tunnels, NOL tunnel number 8 was selected as the facility which provided the best transition testing environment (see Reference A-3). Operating at Mach 5, the tunnel unit Reynolds number range was more than adequate to ensure the capability of obtaining both laminar and turbulent flows in the subsonic region of models with roughnesses in the range of 0.6 to 40 mils. At the same time, the momentum thicknesses were such that the relative roughness , k/θ, covered the range of interest for flight. The tunnel may be run at stagnation temperature up to at least 1400°R so that with the model initially at room temperature, wall cooling ratios in the range of 0.4 to 0.8 are experienced as the model is heated. In summary, this facility allows the close approximation of flight values of the dimensionless parameters which have the greatest influence on transition.

A.2   EXPERIMENTAL PROGRAM

Two series of rough wall calorimeter transition experiments were executed. The first of these, Series A, had a second objective, namely to determine heating augmentation due to roughness (see Reference A-4). In that series several sphere cones and one blunt cone were tested. All were nominally the same size with a wide variation in roughness height. In the second series, Series J, several new models of various sizes and shapes were utilized. All of these had the same roughness height.

A.2.1 Test Series A

A.2.1.1 Model Fabrication and Instrumentation

The model geometries for this test series are shown in Figure A-2. Seven rough wall sphere cones were tested, all with R_N = 2.5 inches and cone half angles of 8°. The eighth rough wall model was a blunt cone, nominally the same size, with R_N = 5.0 inches, a 0.5-inch shoulder radius and a cone half angle of 8°. The models were machined from electroformed nickel.

Surface roughnesses on four models were generated using a grit blasting technique; three sphere cones with peak to valley roughnesses of 0.6, 1.6, and 3.0 mils and the blunt cone with a roughness of 3.0 mils. The remaining four sphere cones had copper particles furnace brazed to their surface with resulting roughness heights of 3.0, 10.0, 40.0 and 80.0 mils. The two roughest models were primarily intended to provide data on the effects of roughness on turbulent heat transfer.

Figure A-3 shows photomicrographs of a sample 3-mil grit blasted surface and a sample 3-mil brazed particle surface. The peak to valley roughness height is the distance between the significant peaks and the significant valleys, but is not the distance from the very highest peak to the lowest valley. The character of an ablated graphite surface is probably best represented by the grit blasted surface.

In order to provide an evaluation of the subjective determination of roughness height described above, samples of all surfaces with $k \leq 10$ mil were analyzed using a Talysurf profilometer.* The RMS roughness determined in this way is shown compared to the peak to valley roughness heights in Figure A-4. One sample from Series J is included. Apparently the peak to valley measure is equal to four times the RMS roughness.

The models were instrumented with chromel-alumel thermocouples spot welded to the interior surface. Two or three primary rays on each model had thermocouples located at every 0.5-inch of the streamwise dimension. Other thermocouples, less closely spaced, were placed on other rays in order to assess asymmetries in the heat transfer to the models.

Further details of model fabrication and instrumentation can be found in Reference A-2 or Reference A-5.

A.2.1.2 Data Reduction

During the tests thermocouple outputs were recorded at the rate of about 18 times per second. These temperature data were temporally smoothed using a quadratic

---

*The results of these measurements were provided by Mr. Gary Denman of AFML/MXS.
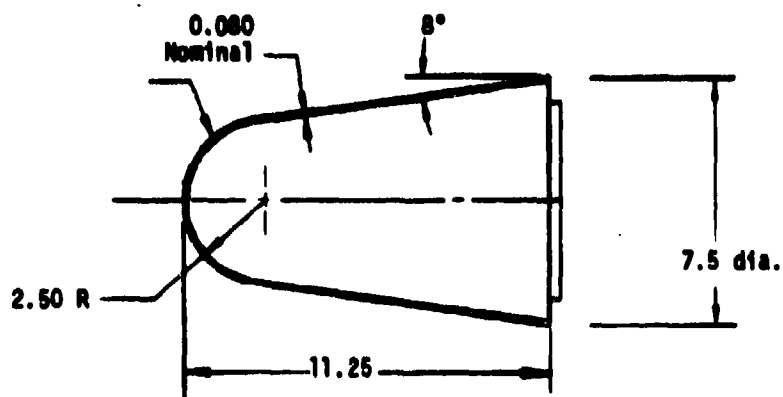
(a) Sphere cone.
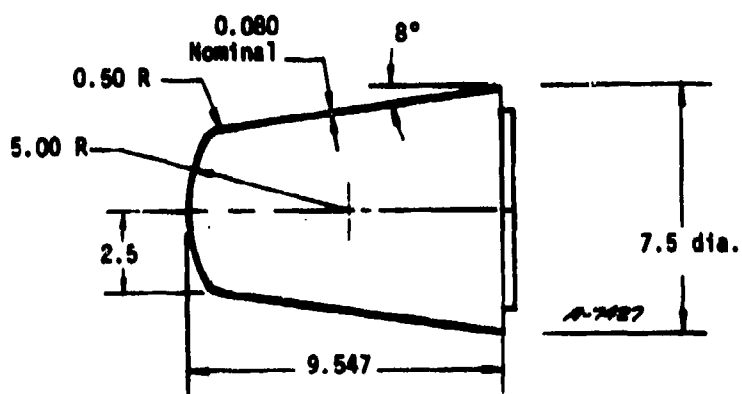
(b) Blunt cone.

Figure A-2. Series A rough wall calorimeters.

a. Nominal 3.0 mil Roughness, 50X

   Grit Blasted Using G-18 Steel Grit,
   Pressure Fed Gun, Supersonic Nozzle, 100 psi
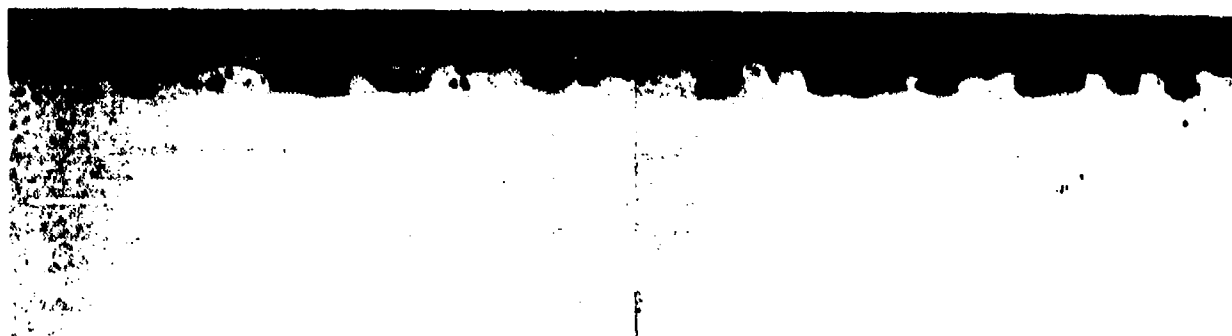
b. Nominal 3.0 mil Roughness, 50X

   140/200 Spherical Copper Particles Furnace
   Brazed to Nickel Surface

Figure A-3.   Photomicrographs of sample surfaces.

A-10
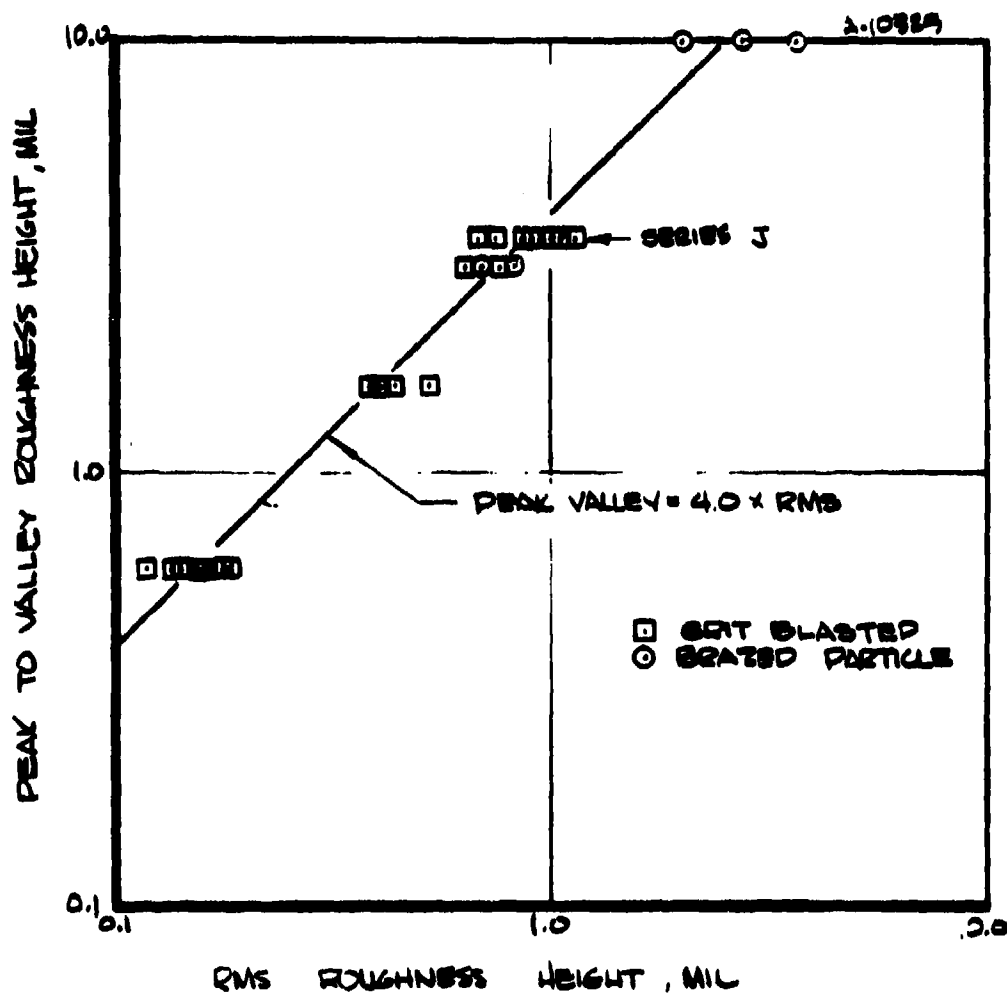
Figure A-4. Summary of profilometer roughness height measurements.

spline fit procedure. After an initial response time which is less than 0.5 second, front and back wall temperature rise rates are essentially equal. Therefore, heat transfer to the calorimeter was calculated considering only energy storage associated with the temperature rise rate and streamwise conduction. Details of the data reduction procedures are given in Reference A-2.

For the purpose of determining transition locations, distributions of experimental heat transfer coefficients were plotted at several test times for comparison with the laminar distribution. The laminar distribution is nearly independent of wall temperature and, therefore, test time. The transition location was defined as the point where the experimental distribution departed from the laminar distribution; see Section A.2.2.2 and Figure A-6. Several examples are shown in Reference A-2.

Information describing the test conditions for the runs yielding transition data is presented in Table A-1. Transition locations at three (or sometimes two) test times along with other pertinent data are also shown. Correlations of exact smooth wall laminar boundary layer solutions were used to calculate the boundary layer parameters θ and δ^*. The details of these methods are given in Reference A-2.

The correlation of this data is described in Section A.3. In order to determine whether any important physics associated with body size and shape were lacking from the correlation, a second set of experiments, Series J, described below, was performed.

A.2.2 Test Series J

A.2.2.1 Model Fabrication and Instrumentation

The model geometries for this test series are shown in Figure A-5. Three new sphere cone models were fabricated. These had nose radii of 0.75, 1.5, and 3.5 inches, all with an 8° cone half angle. The two other models were a 60° biconic and a laminar ablated shape. All of the Series J models were machined from cold rolled nickel and were grit blasted to a peak to valley roughness height of 3.5 mils (see Figure A-4).

Backface chromel-alumel thermocouples were again used. Thermocouple locations varied from model to model but were roughly similar to the installation on the Series A models.

For more detailed information regarding the Series J models and instrumentation, see Reference A-6.

A.2.2.2 Data Reduction

Data recording and smoothing techniques as well as the computation of heat transfer coefficients were essentially the same as they were for Series A. An example plot of heat transfer coefficient distributions is shown in Figure A-6. Transition

TABLE A-1

SERIES A TRANSITION LOCATION DATA

Run	R_N (in)	k (mil)	P_0 (atm)	T_0 (°R)	u^*/ν^* (10^6/ft)	Time (sec)	s/R_N	T_w/T_e	u_e/ν_e (10^6/ft)	θ (mil)	δ^* (mil)	M_e
104	2.5	0.6	2.60	1240	4.21	1	0.33	0.47	2.54	0.61	0.42	0.43
						3	0.38	0.58	2.86	0.60	0.60	0.50
						5	0.47	0.68	3.35	0.61	0.78	0.62
105	2.5	0.6	2.01	1245	3.24	1	0.42	0.48	2.38	0.72	0.53	0.56
						5	0.49	0.66	2.66	0.71	0.88	0.65
						7	0.56	0.74	2.88	0.72	1.06	0.75
113	2.5	1.6	1.54	1240	2.50	1	0.23	0.46	1.08	0.78	0.53	0.30
						5	0.36	0.65	1.62	0.76	0.91	0.48
						9	0.42	0.77	1.84	0.74	1.15	0.56
115	2.5	1.6	1.03	1210	1.72	1	0.40	0.48	1.22	0.98	0.70	0.53
						3	0.45	0.56	1.33	0.98	0.94	0.60
129	2.5	3.0	0.53	1220	0.88	1	0.40	0.45	0.63	1.39	0.88	0.53
						5	0.44	0.54	0.67	1.38	1.22	0.58
						9	0.50	0.62	0.74	1.38	1.55	0.66
130	2.5	3.0	1.06	1250	1.70	1	0.22	0.44	0.71	0.96	0.56	0.29
						5	0.26	0.58	0.83	0.91	0.91	0.34
						9	0.33	0.69	1.02	0.90	1.18	0.43
132	2.5	3.0	0.66	1445	0.90	1	0.38	0.39	0.61	1.40	0.64	0.50
						5	0.42	0.50	0.66	1.38	1.06	0.56
						9	0.49	0.59	0.74	1.38	1.44	0.56
162	2.5	3.0	0.53	1200	0.88	1	0.43	0.48	0.66	1.40	1.01	0.57
						3	0.52	0.53	0.75	1.44	1.27	0.69
163	2.5	3.0	1.05	1200	1.75	1	0.17	0.47	0.57	0.92	0.64	0.22
						5	0.22	0.59	0.73	0.89	0.92	0.29
						9	0.29	0.69	0.95	0.86	1.15	0.38
165	2.5	10.0	0.21	1200	0.35	1	0.30	0.46	0.20	2.10	1.42	0.39
						3	0.31	0.49	0.20	2.09	1.57	0.41
						5	0.54	0.55	0.31	2.29	2.12	0.72
169	2.5	10.0	0.39	1200	0.66	1	0.20	0.46	0.25	1.51	1.01	0.25
						9	0.23	0.54	0.28	1.48	1.33	0.30
						17	0.26	0.61	0.32	1.44	1.60	0.34

Run	R_N (in)	k (mil)	P_0 (atm)	T_0 (°R)	u^*/ν^* (10^6/ft)	Time (sec)	s/R_N	T_w/T_e	u_e/ν_e (10^6/ft)	θ (mil)	δ^* (mil)	M_e
171	2.5	40.0	0.52	1215	0.87	1	0.14	0.47	0.23	1.32	0.91	0.19
						5	0.17	0.59	0.28	1.26	1.33	0.22
						9	0.20	0.69	0.33	1.22	1.62	0.25
174	2.5	40.0	0.21	1190	0.35	1	0.22	0.47	0.15	2.06	1.42	0.29
						5	0.26	0.53	0.17	2.04	1.78	0.34
						9	0.30	0.59	0.20	2.00	2.09	0.39
180	5.0	3.0	1.03	1200	1.61	1	0.18	0.46	0.64	1.26	0.64	0.25
						9	0.22	0.61	0.77	1.21	0.97	0.30
						17	0.26	0.73	0.90	1.18	1.25	0.36
181	5.0	3.0	0.52	1200	0.89	1	0.34	0.47	0.58	1.76	1.01	0.48
						3	0.36	0.50	0.61	1.74	1.18	0.51

(a) 1.5-inch sphere/8° cone
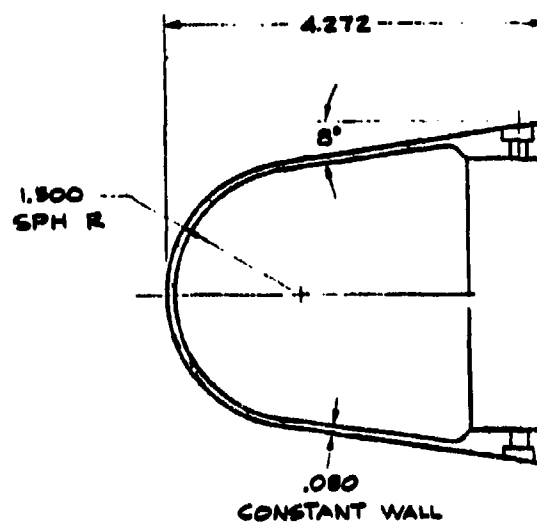
(b) 60° biconic
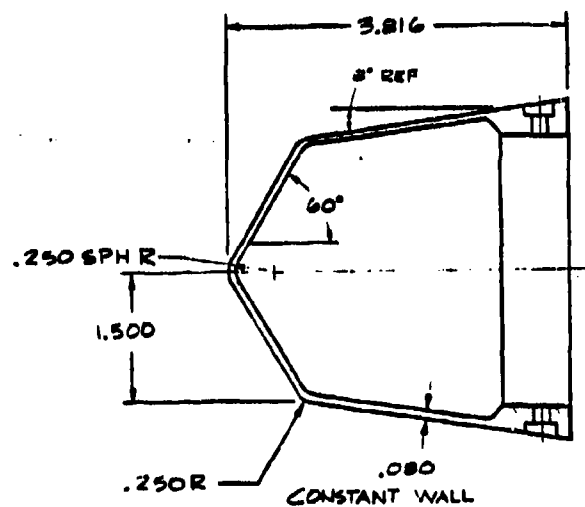
(c) Laminar blunt
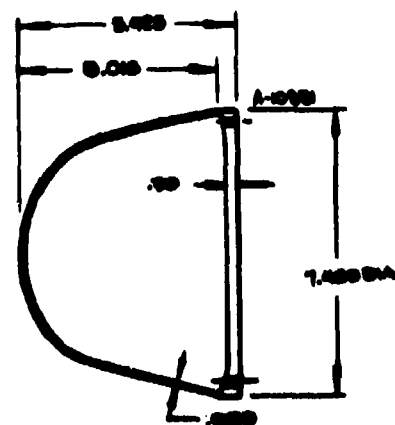
Figure A-5. Series J rough wall calorimeters.
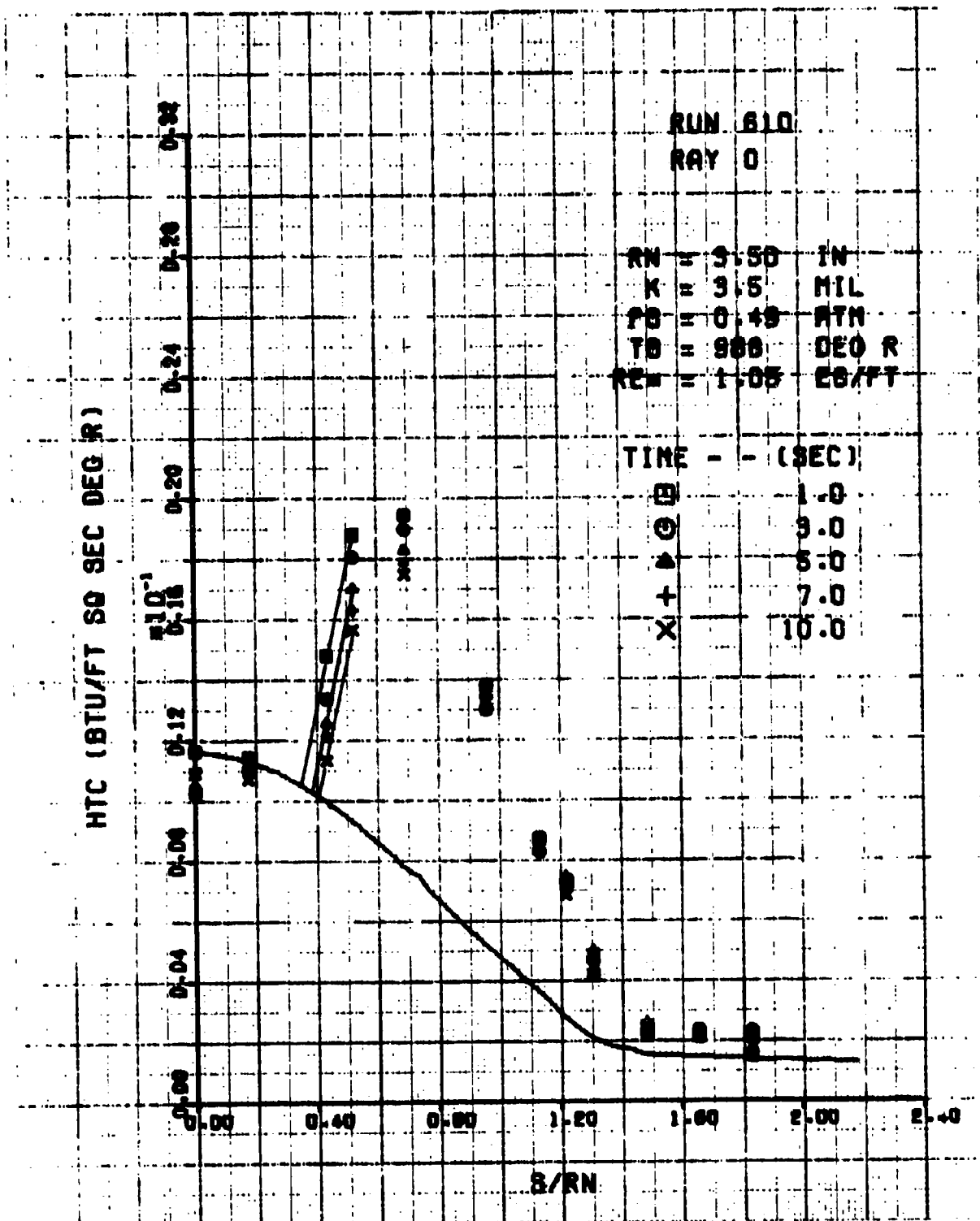
Figure A-6. Example heat transfer coefficient distributions showing selected transition locations.

locations for 1, 5, and 10 second test times are indicated by the intersection of the straight lines with the laminar distribution. Run conditions and transition location data for Series J are listed in Table A-2. Data from the 0.75-inch nose radius model were not used here but were used in the onset correlation (see Section A.3.3).

A.3   ROUGHNESS INDUCED TRANSITION CORRELATION

A.3.1   Modeling of Roughness Induced Transition

In the present analysis it is assumed that the response of a laminar boundary layer to a disturbance will depend primarily upon the magnitude of the disturbance and the potential of the boundary layer to amplify disturbances. With proper identification of the disturbance and the amplification potential, the boundary layer would be expected to respond as indicated in the sketch. Small disturbances would require
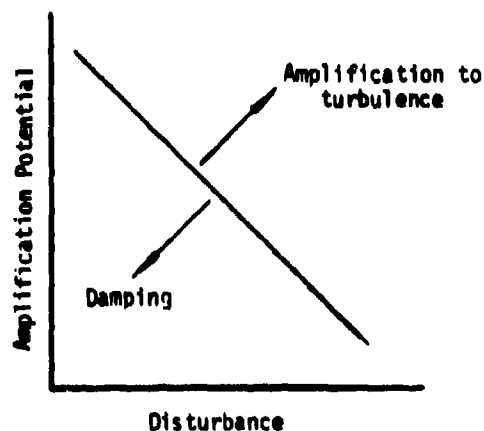
larger amplification potential to initiate transition than would large disturbances.

This sort of idea was used to correlate transition data from low speed boundary layers on adiabatic flat plates which are subject to distrubance from the wind tunnel free stream turbulence. The data, which were taken from Schlichting (Reference A-7) are from experiments carried out by several investigators. These data are shown in Figure A-7. For this case, the free stream turbulence intensity is taken to be the measure of the disturbance, and it apparently determines the value of Re_θ (amplification potential) at which transition occurs.

The turbulence intensity (abscissa in Figure A-7) is the square root of the relative kinetic energy of the turbulent fluctuations. This is perhaps an indication

A-17

Run	R_N (in)	k (mil)	P_0 (atm)	T_0 (°R)	u^*/ν^* (10⁶/ft)	Time (sec)	s/R_N	T_w/T_e	u_e/ν_e (10⁶/ft)	θ (mil)	δ^* (mil)	M_e
601	2.5	3.0	0.56	1310	0.86	1	0.36	0.44	0.56	1.40	0.86	0.47
						5	0.42	0.53	0.63	1.39	1.21	0.56
						10	0.51	0.63	0.72	1.41	1.62	0.68
604	2.5	3.0	1.06	1335	1.58	1	0.22	0.44	0.66	0.99	0.59	0.29
						5	0.26	0.56	0.77	0.95	0.92	0.34
						10	0.32	0.69	0.93	0.93	1.22	0.42
607	3.5	3.5	0.46	1340	0.68	1	0.37	0.44	0.45	1.86	1.16	0.49
						5	0.42	0.50	0.50	1.86	1.48	0.56
						10	0.46	0.57	0.54	1.86	1.82	0.61
608	3.5	3.5	1.18	1360	1.72	1	0.16	0.44	0.53	1.12	0.67	0.21
						5	0.18	0.48	0.59	1.10	0.81	0.23
						10	0.22	0.63	0.72	1.05	1.21	0.29
610	3.5	3.5	0.49	985	1.05	1	0.35	0.58	0.69	1.38	1.40	0.46
						5	0.38	0.63	0.73	1.37	1.58	0.50
						10	0.41	0.69	0.78	1.36	1.79	0.54
611	3.5	3.5	0.78	965	1.70	1	0.19	0.58	0.61	1.05	1.07	0.24
						5	0.22	0.64	0.71	1.04	1.22	0.29
						10	0.24	0.71	0.77	1.01	1.38	0.31
619	1.5	3.5	0.64	1315	0.97	1	0.39	0.46	0.68	1.02	0.68	0.51
						5	0.44	0.59	C 74	1.00	1.03	0.58
						10	0.46	0.69	0.76	0.98	1.29	0.61
620	1.5	3.5	1.15	1320	1.74	1	0.23	0.45	0.75	0.73	0.47	0.30
						5	0.27	0.63	0.88	0.69	0.79	0.35
						10	0.32	0.77	1.02	0.66	1.02	0.42
621	1.5	3.5	0.77	1310	1.18	1	0.29	0.46	0.64	0.89	0.60	0.38
						5	0.33	0.59	0.71	0.86	0.90	0.43
						10	0.37	0.71	0.78	0.84	1.16	0.49
623	1.5	3.5	0.55	1030	1.11	1	0.36	0.56	0.72	0.90	0.85	0.48
						5	0.40	0.66	0.79	0.89	1.08	0.53
						10	0.42	0.74	0.82	0.87	1.27	0.56

| Run	R_N (in)	k (mil)	P_o (atm)	T_o (°R)	u^*/ν^* (10^6/ft)	Time (sec)	s/R_N	T_w/T_e	u_e/ν_e (10^6/ft)	θ (mil)	δ^* (mil)	M_e
624	1.5	3.5	0.78	975	1.68	1	0.26	0.58	0.82	0.70	0.71	0.34
						5	0.30	0.69	0.94	0.68	0.90	0.39
						10	0.33	0.79	1.02	0.66	1.07	0.43
629	0.25	3.5	0.60	1310	0.92	1	3.07	0.45	0.57	1.60	1.02	0.44
						5	3.60	0.54	0.58	1.63	1.47	0.45
						10	3.89	0.63	0.59	1.62	1.85	0.46
631	0.25	3.5	0.43	1300	0.66	1	4.99	0.46	0.46	1.91	1.27	0.51
						5	5.16	0.54	0.47	1.84	1.62	0.51
						10	5.39	0.61	0.51	1.71	1.89	0.62
632	0.25	3.5	0.72	1310	1.10	1	1.97	0.47	0.65	1.25	0.86	0.41
						5	2.15	0.58	0.65	1.23	1.24	0.41
						10	2.44	0.67	0.66	1.24	1.58	0.42
636	3.73	3.5	1.16	1330	1.74	1	0.17	0.42	0.58	1.12	0.63	0.23
						3	0.19	0.49	0.65	1.10	0.82	0.25
						7	0.23	0.60	0.78	1.06	1.13	0.31
638	3.73	3.5	0.58	1300	0.89	1	0.33	0.43	0.56	1.62	0.93	0.45
						5	0.43	0.53	0.70	1.62	1.40	0.60
						10	0.56	0.66	0.83	1.67	2.05	0.82
640	3.73	3.5	0.69	1295	1.07	1	0.27	0.43	0.56	1.45	0.86	0.36
						5	0.36	0.54	0.72	1.44	1.27	0.49
						10	0.47	0.66	0.89	1.44	1.76	0.67
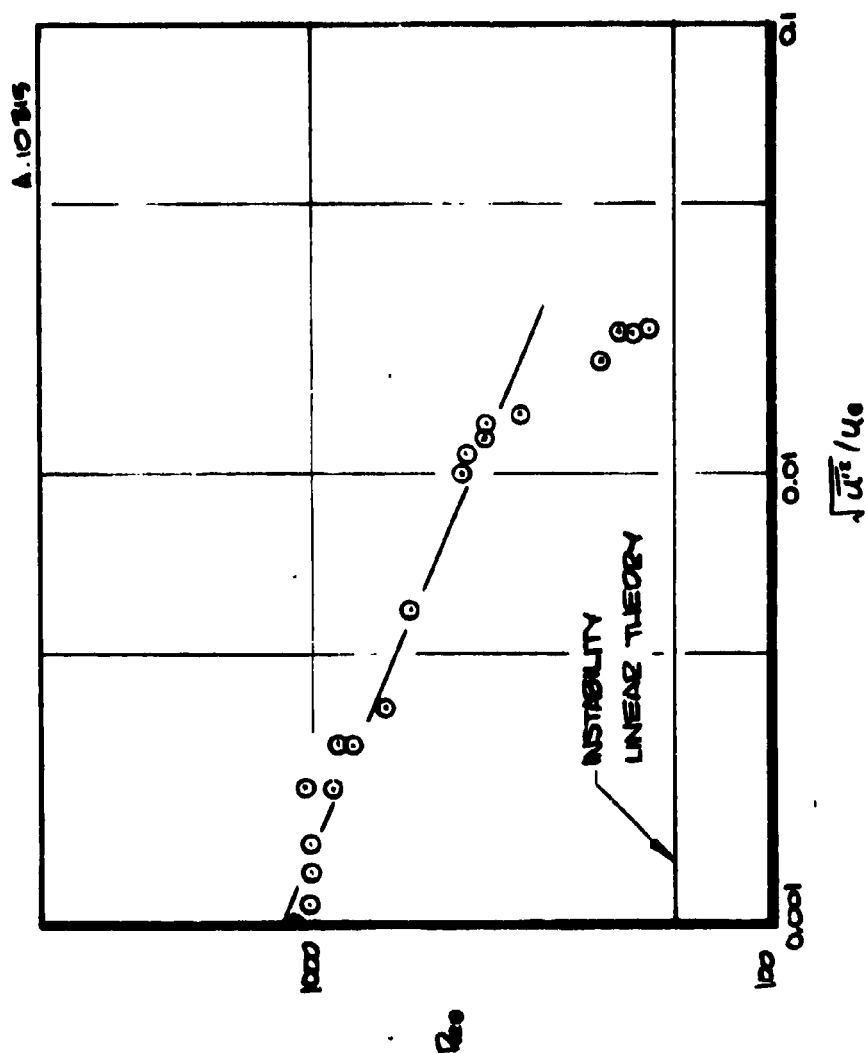
Figure A-7. Flat plate transition Reynolds numbers as a function of free stream turbulence intensity.

that, in general, the kinetic energy of a disturbance is the proper indicator of its magnitude. This concept will be used in a later section where the correlation developed below is extended theoretically to include blowing.

A.3.1.1 Amplification Potential Representation

Following this example, the momentum thickness Reynolds number (evaluated as if the wall were smooth) is used as the parameter whose magnitude represents the tendency of the boundary layer to amplify disturbances. For the above constant property example, the displacement thickness could have been used instead of the momentum thickness because the shape factor is constant ($\delta^*/\theta = 2.59$). However, in the subsonic region of a blunt body the displacement thickness is a strong function of wall cooling ratio while the momentum thickness is relatively insensitive to that parameter (see Appendix C, Reference A-2). Anderson (Reference A-2) discussed correlations based on δ^* along with those based on θ. The correlations based on displacement thickness are no longer recommended because (a) $\delta^* < 0$ for $T_w/T_e \leq 0.2$, (b) θ is most readily obtainable from engineering codes, and (c) the correlation based on a momentum thickness is slightly better when the data from Series J are included. In the following analysis, the momentum thickness Reynolds number is used as the sole measure of the amplification potential. However, two other influences, known to be stabilizing, are at work. These are the favorable streamwise pressure gradient and the normal pressure gradient associated with the centrifugal acceleration. It was not found necessary to explicitly include either of these effects in the correlation. However, the difference between the onset and location criteria discussed in a later section is most likely the result of these effects.

A.3.1.2 Disturbance Model

As mentioned above, the flat plate example (Figure A-7) suggests that the kinetic energy of a disturbance is the proper measure of its strength to promote transition. In the absence of a detailed knowledge of the flow around roughness elements immersed in a shear flow, this kinetic energy is impossible to evaluate. Instead, a correlation is developed in terms of the simple parameters available from an engineering code based on the integral momentum equation. The simple disturbance parameter identified during this correlation will later be shown to be associated with the kinetic energy of the mean boundary layer flow at the top of the roughness element.

The basic disturbance parameter is taken to be the relative roughness defined as k/θ. This is physically meaningful because roughnesses which protrude further out in a boundary layer will cause relatively larger disturbances. The magnitude of this influence depends upon the density and velocity profiles so that the

boundary conditions T_w/T_e and B' can also be expected to have an effect on the strength of the disturbance. The role of T_w/T_e is evident from the data while that of B' is inferred theoretically.

A.3.1.3 Transition Parameter Distributions Around a Sphere Cone

Distributions of momentum thickness, boundary layer edge unit Reynolds number, wall cooling ratio, and momentum thickness Reynolds number around a sphere cone at uniform wall temperature are shown in Figure A-8. Re_θ is seen to be a smoothly increasing function of streamwise distance because of compensating trends in the unit Reynolds number and momentum thickness distributions.

For uniform roughness height, the growth of the momentum thickness tends to decrease the disturbance (k/θ) while increasing the amplification potential (Re_θ). If these effects were exactly compensating (they aren't quite) the location of transition would not depend on the momentum thickness at all. In that case, ignoring wall cooling ratio effects, the correlation would be of the form

$$\frac{u_e \theta}{\nu_e} \; \frac{k}{\theta} = \frac{u_e k}{\nu_e} = \text{constant}$$

that is, a critical roughness Reynolds number. This may be regarded as a reasonable approximate indicator of the variation of the severity of the transition environment around the body. The distribution of Re_k, which is the same as the unit Reynolds number, indicates an increasing severity of transition environment with streamwise distance until a maximum near the sonic point followed by a 30 percent reduction to the cone level. The critical Re_k transition model would therefore indicate that transition should only occur ahead of the sonic point. PANT data, in fact, show that on the spherical surface rough wall transition locations are restricted to the subsonic region.

A.3.2 Transition Location Data Correlation

Initial efforts to correlate transition location data were in terms of Re_θ as the amplification parameter versus k/θ as the disturbance parameter. This is shown qualitatively in the sketch in the top left of page A-24. The primary shortcoming of this method of correlation is that the data trend during a run as the wall temperature increases is not parallel to the main (run to run) data trend. The simple Re_k criterion mentioned above is also shown on this sketch. It does not have the correct slope to properly correlate the data at any particular wall cooling ratio.
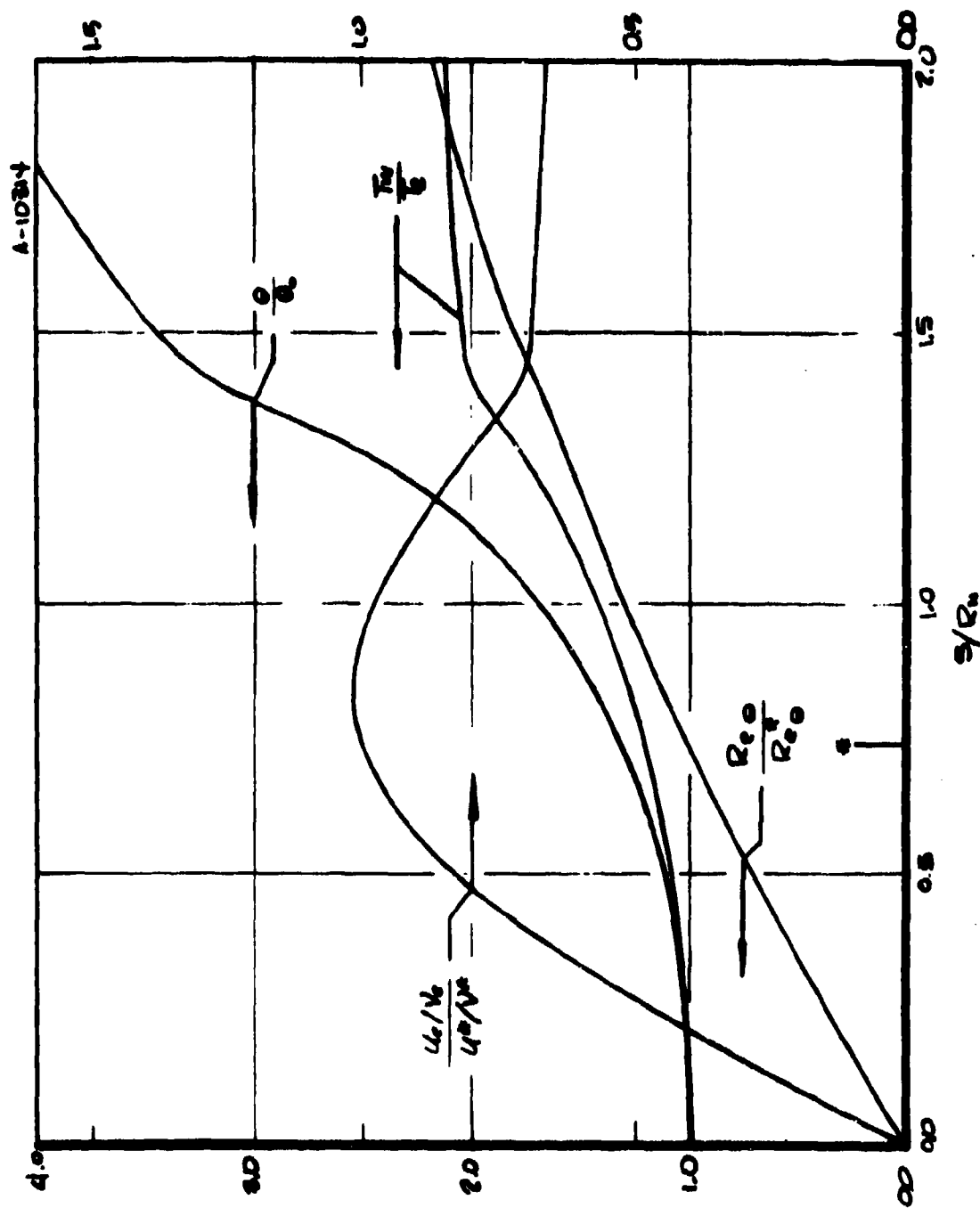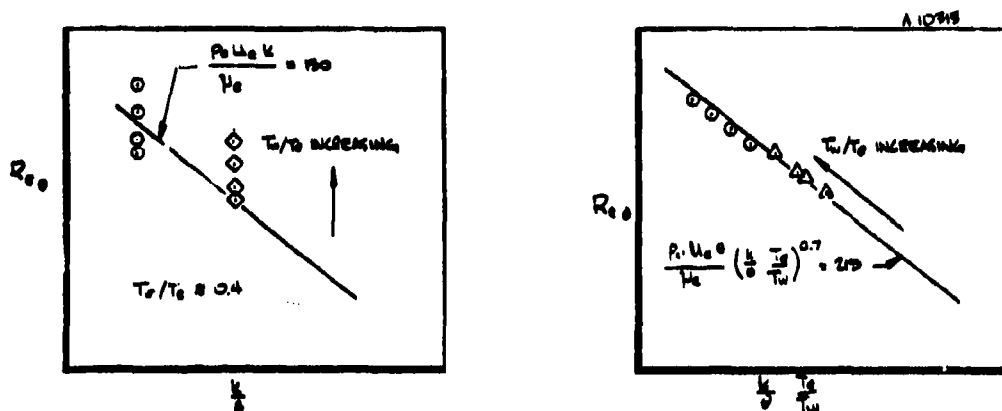
Figure A-8. Distribution of transition parameters around a sphere cone. Wall temperature constant, $T_w = T_0$.

It was found that the wall cooling ratio times the momentum thickness is an effective boundary layer thickness which allowed a satisfactory data correlation. This scheme is shown in the sketch on the right. Data trends for various runs (note large roughness exception below) are essentially colinear. This correlation technique is used throughout what follows.

A.3.2.1 Correlation of Series A Transition Location Data

The Series A data listed in Table A-1 is shown on the above suggested correlation plane in Figure A-9. In Reference A-2, data from two rays were usually reported; here, for the sake of brevity, only one ray is used. Model geometries for this series are shown in Figure A-2. These models had roughness heights between 0.6 and 40.0 mils as indicated in Figure A-9. All of the data except that from the 40.0-mil model are correlated within 20 percent by the equation

$$Re_\theta \left(\frac{T_e}{T_w} \ \frac{k}{\theta} \right)^{0.7} = 215$$

The expression on the left of this equation will hereinafter be called the transition parameter.

There is some possibility that another source of disturbance, namely, wind tunnel noise, is slightly influencing the data from the model with the lowest roughness. Transition Reynolds numbers for these data appear to be a little low with respect to the correlation line. If this is indeed a noise effect it would indicate that the roughness on this model is the threshold for roughness domination for the noise levels encountered in this tunnel.
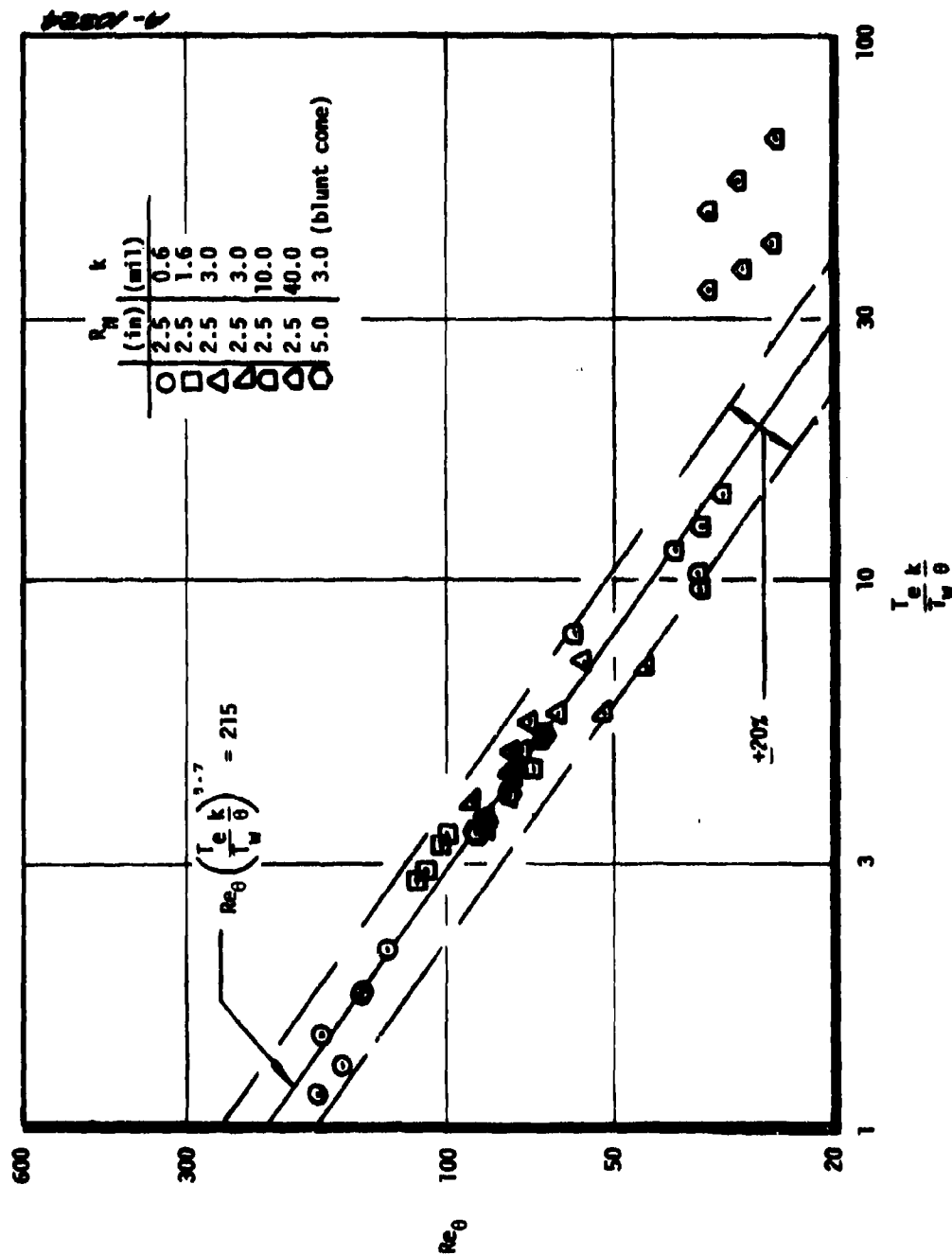
Figure A-9. Correlation of Series A transition location data.

It is not too surprising that the data from the 40 mil model do not agree with the correlation since k/θ is in the range of 20 to 30, so that the roughness is larger than the smooth wall boundary layer thickness. It can be seen from Figure A-1 that these relative roughnesses are much larger than those encountered in flight with k < 1.0 mil and, therefore, these data are not of too much concern.

As mentioned in Section A.2.1, it was judged necessary, after the correlation of the Series A data, to enlarge the data base to include experiments with a wider range of nosetip size and shape. For this purpose, Test Series J was performed.

A.3.2.1 Correlation of Series J Transition Location Data

The correlation of the Series J transition location data (listed in Table A-2) is shown in Figure A-10. Model geometries are shown in Figure A-3. Except for the one Series A model (R_N = 2.5 inch, k = 3.0 mil) which was reused, all of these models had roughnesses of 3.5 mil. No explicit influence of body size and shape is evident, and the quality of the correlation is about the same as it is for the Series A data.

Although the data from the biconic model fall within the scatter band, the trend with increasing wall temperature is not parallel to the correlation. This is not a typical nosetip shape, at least not until after transition and sharpening have occurred. These data would be useful as part of a cone transition data base.

A.3.3 Correlation of Transition Onset Data

The correlation presented in Section A.2 indicates the location of transition when it occurs. However, roughness dominated transition is not observed to occur in a region just forward of the sonic point even when the transition parameter exceeds 215. This anomaly is rationalized through the use of a separate onset criterion describing the conditions at which the transition location just enters (or leaves) the subsonic region. As mentioned in Section A.1, transition onset is the most important single event in determining total nosetip recession and therefore deserves specific attention.

Figure A-11 shows distributions of the transition parameter around a sphere cone for two conditions which differ slightly in the severity of the transition environment. These are computed assuming uniform wall temperature and uniform roughness height. Note that these distributions are quite similar to distributions of Re_k. For the conditions represented by the lower curve, transition is not observed (except perhaps on the cone) even though the transition parameter exceeds 215. As the environment becomes more severe, say by increasing the sonic point unit Reynolds number, transition first appears when the transition parameter evaluated at the sonic point becomes 255. The location criterion then determines the transition point.
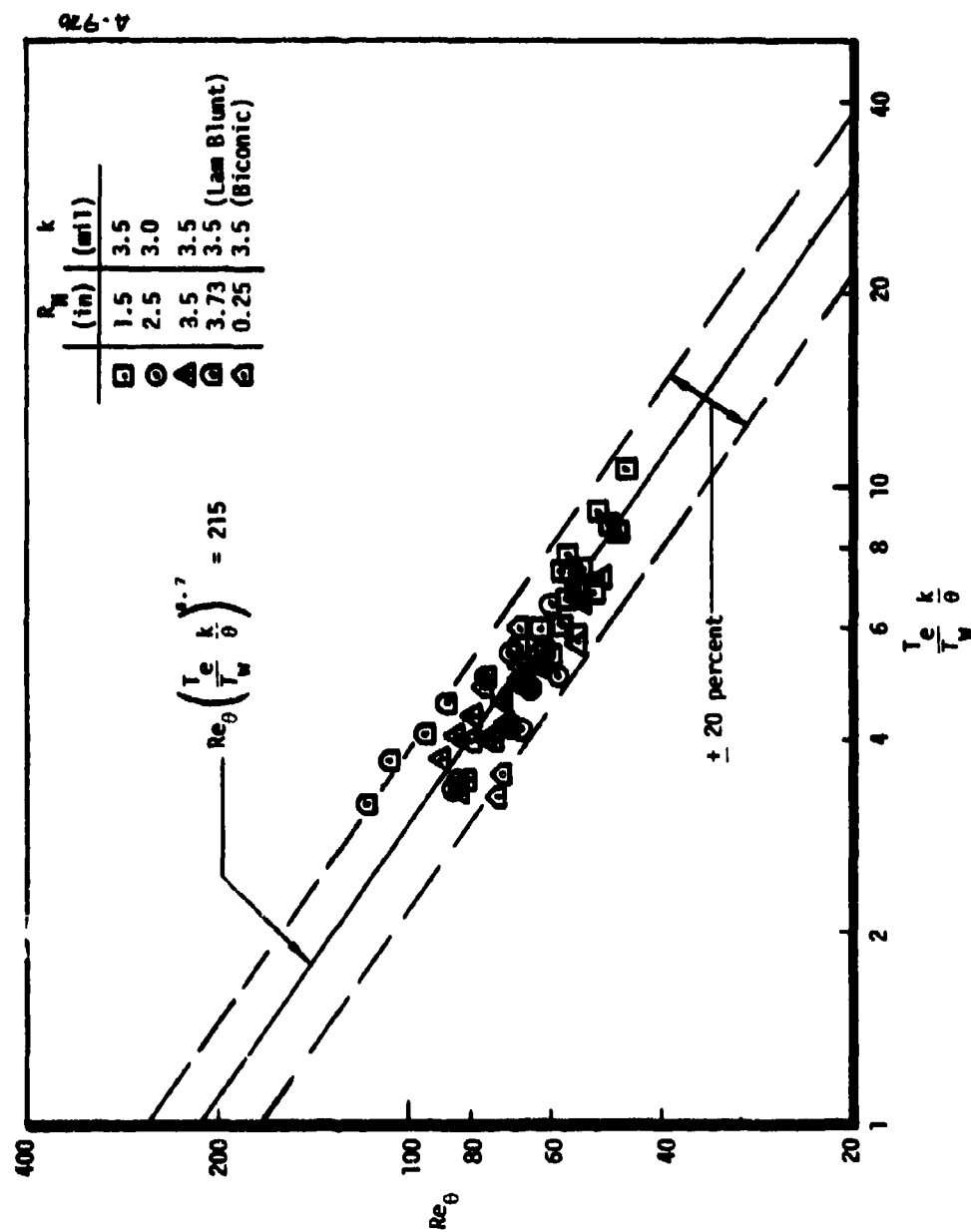
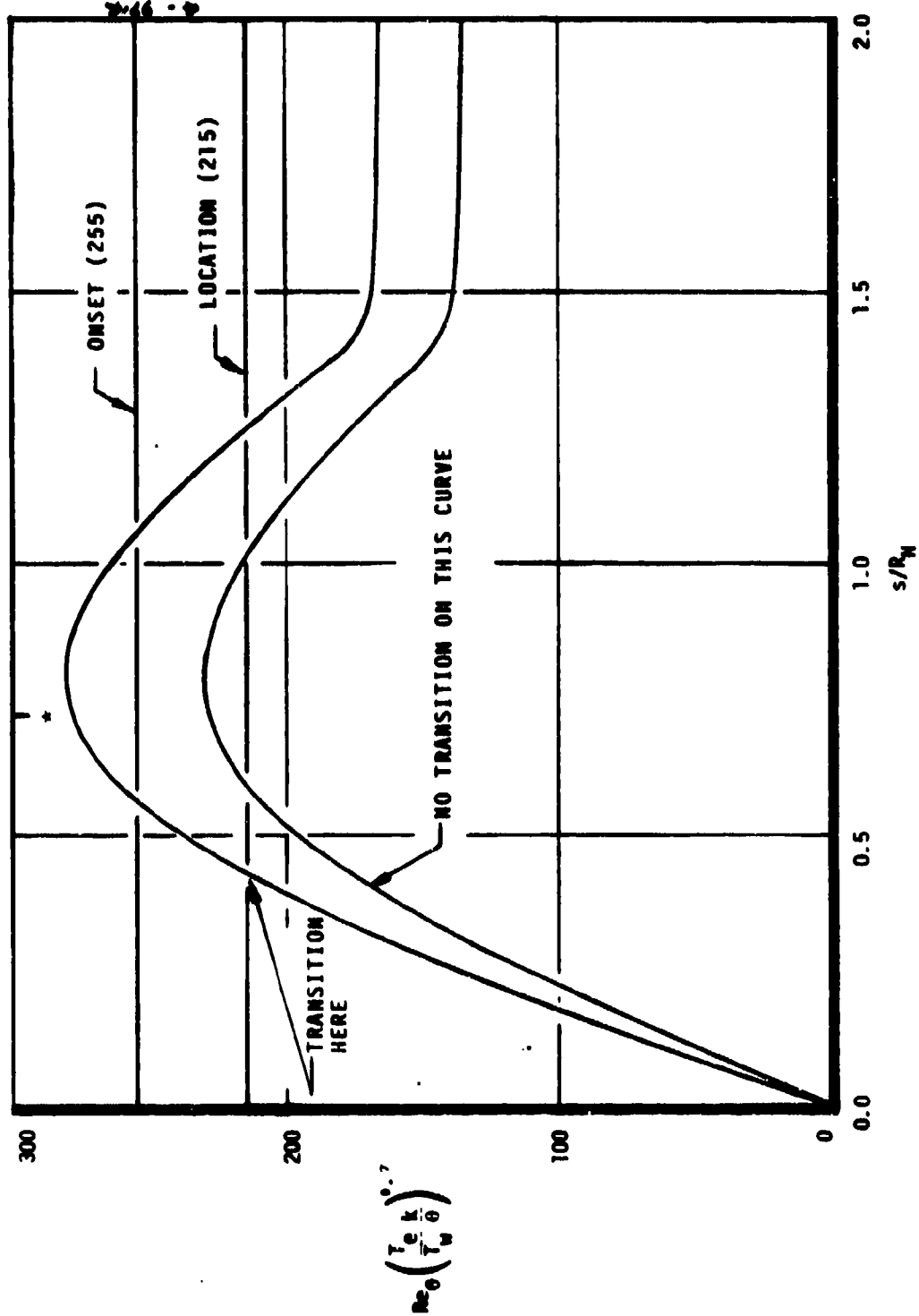Figure A-10. Correlation of Series J transition location data.

A-27

Figure A-11. Distributions of the transition parameter around a sphere cone of uniform wall temperature.

For any single geometry, the onset criterion could be replaced by a geometrical restriction on the application of the location criterion. However, the present scheme appears to be applicable to blunter shapes as well; for example, the Series A blunt cone.

Transition onset data from both test series are shown in Figures A-12. Data from the biconic model and the sphere cone with a 40 mil roughness height are not included. The various runs are classified according to whether transition was located in the subsonic region during the entire run (turbulent), transition passes aft of the sonic point during a run (onset), or, no subsonic transition was observed (laminar). For laminar runs, sonic values of the parameters are evaluated at the beginning of the run when conditions are most severe. For onset runs, the parameters are evalauted at onset time and for turbulent runs they are evalauted at the latest data time; that is, when conditions are least severe (largest T_w/T_e).

In general, the onset data are extremely well correlated by the suggested expression. Minor exceptions are apparent for the model with the smallest roughness. Again, since the Reynolds numbers for those data are low, this may be an indication of a minor tunnel noise influence at this small relative roughness.

A.3.4 Summary of Correlation Results

Using Re_θ as the amplification parameter, a modified relative roughness, $(T_e/T_w)(k/\theta)$, has been empirically identified as the disturbance parameter. The correlations for onset and location may be stated in terms of critical values of the transition parameter

$$Re_\theta \left(\frac{T_e}{T_w} \frac{k}{\theta} \right)^{0.7} = \begin{cases} 255*, \text{ onset} \\ 215, \text{ location} \end{cases}$$

The data correlated were from the subsonic region of roughened blunt calorimeters tested in a hypersonic wind tunnel. Tests covered the ranges of pertinent parameters of interest for graphite in flight with the exception of pressure, enthalpy level, and blowing rate.

A.4 THEORETICAL EXTENSION OF DISTURBANCE MODELING TO FLIGHT CONDITIONS

In the previous section, the modified relative roughness, $(T_e/T_w)(k/\theta)$, was empirically established as the measure of the disturbance introduced by roughness elements on solid calorimeters. This disturbance parameter is believed to be representative of a more physically meaningful measure of the disturbance, such as the
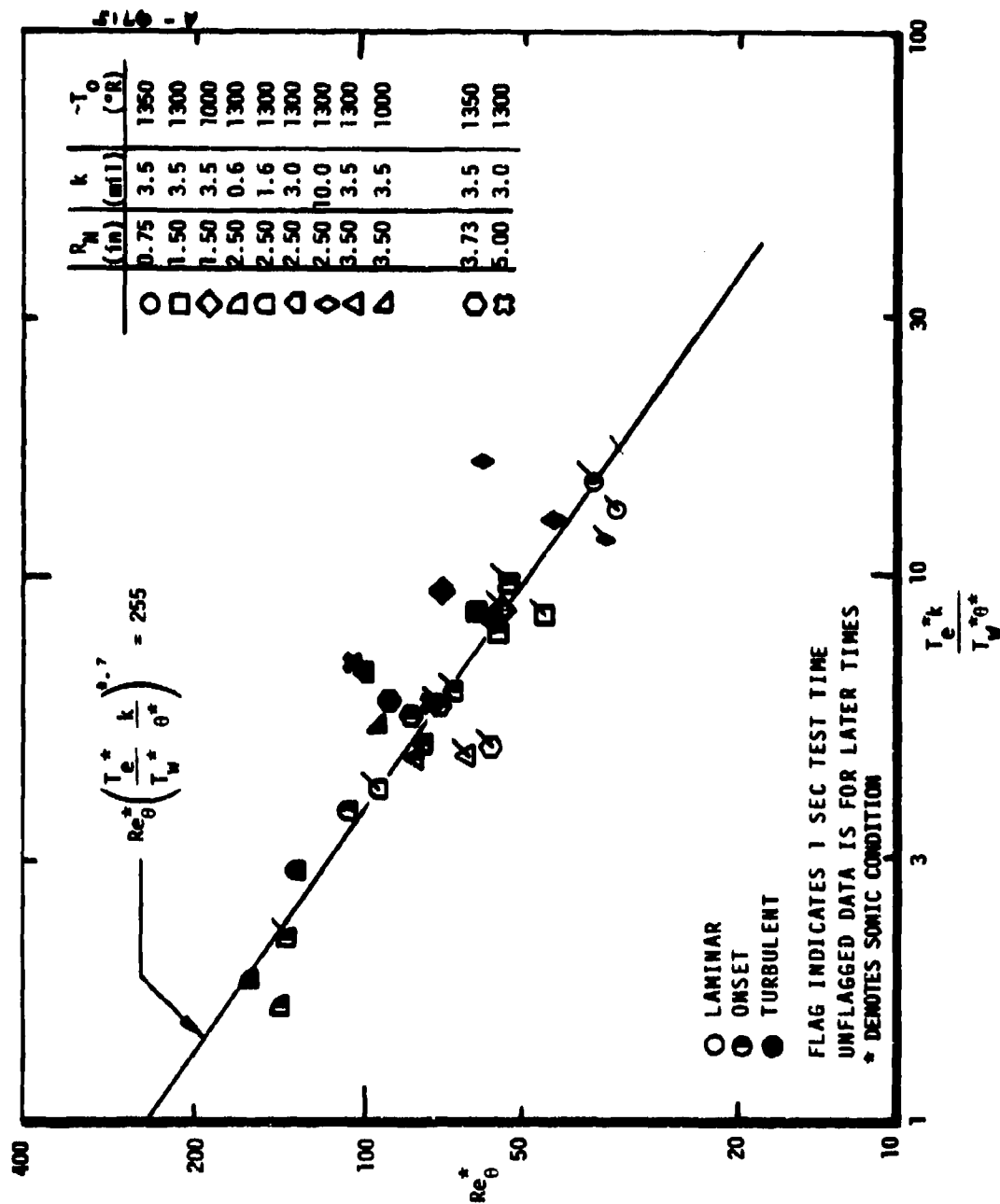
---

*Evaluated at the sonic point.

Figure A-12. Transition onset data correlation.

relative kinetic energy of the disturbance (refer to the flat plate example of Figure A-7). By analogy with this example, and with the additional postulate that the kinetic energy of the disturbance introduced by the roughness is closely related to the mean kinetic energy at the top of the roughness elements, the following hypothesis is suggested:

> The relative mean kinetic energy at the top of the roughness element, $\rho_k u_k^2 / \rho_e u_e^2$, is the key physical parameter in evaluating the tendency of roughness induced disturbances to promote boundary layer transition.

Laminar boundary layer profiles are a required input to the evaluation of this hypothesis and they are also essential to the related extension of the disturbance modeling to conditions of interest for flight. For application, however, the transition criteria must be formulated in terms of information available during the integral solutions used in shape change codes. This information does not include boundary layer profiles. The practical utility of the above hypothesis is realized primarily in relating the effects of ablation to the well understood effects of variation in wall cooling ratio. Once this is accomplished, the empirical disturbance parameter can be generalized, in terms available during an integral solution, to include the effects of ablation.

In the next subsection, the technique used to represent laminar kinetic energy profiles is discussed. This is followed by an analysis of these profiles (for conditions typical of the wind tunnel calorimeter experiments) which substantiates the hypothesis. The hypothesis is then assumed to also apply in the presence of blowing and is used in the determination of a modified empirical disturbance parameter which includes the effect of blowing. The influence of mass transfer on the boundary layer profiles is determined by the dimensionless blowing rate, $B' = (\rho v)_w / (\rho_e u_e C_H)$. Finally, using the same approach, this disturbance modeling is extended to include the effects of dissociation and ablation typical of graphite ablation in flight.

A.4.1 Boundary Layer Profile Representation

Laminar boundary layer solutions for the situations of interest were generated using the Boundary Layer Integral Matrix Procedure (BLIMP) code which is described in detail in Reference A-8. BLIMP is essentially an implicit code for the solution of the two-dimensional or axisymmetric boundary layer equations for transport of mass, momentum, energy, and species, assuming chemical equilibrium. Nonsimilar terms in the equations are reduced significantly by transformation to the appropriate Levy-Lees coordinates.

For an axisymmetric geometry these coordinates are

$$\xi(s) = \int_0^s \rho_e u_e \mu_e r^2 ds \ , \quad \eta(y,\xi) = \frac{\rho_e u_e r}{\sqrt{2\xi}} \int_0^y \frac{\rho}{\rho_e} dy$$

A-31

In the study of the solutions described below it is convenient to plot boundary layer profiles in terms of a normal coordinate which absorbs the influence of the boundary layer edge conditions but does not reflect the influence of the surface boundary conditions, T_w/T_e and B'. The effects of varying these parameters will appear in the profiles and not in the coordinates. The incompressible form of the above normal variable,

$$\eta_0(y,\xi) = \frac{\rho_e u_e r}{\sqrt{2\xi}} y$$

is the coordinate which provides these useful features and it is utilized below in the presentation of boundary layer profiles. It should be emphasized that this coordinate is simply convenient for the interpretation of solutions and is not involved in the generation of solutions.

For the purposes of comparing the relative influence of blowing and wall cooling ratio on the kinetic energy profile, solutions for the stagnation region, where

$$\beta = \frac{\xi}{2u_e} \frac{du_e}{d\xi} = 0.5$$

are used in all that follows. This is a good approximation for the subsonic region to which the present data and analysis are restricted. Note that

$$\lim_{\xi \to 0} \eta_0(y,\xi) = \sqrt{\frac{2\rho_e}{\mu_e} \frac{du_e}{ds}} \, y$$

Figure A-13 shows relative kinetic energy profiles for air in a stagnation region without mass transfer. Since the initial goal is to interpret data taken in a wind tunnel with $T_0 \approx 1300°R$, the enthalpy level for these solutions was selected accordingly. Note that at some fixed distance from the wall the variation of kinetic energy with wall temperature is in the direction consistent with trends in the transition data. That is, for a higher wall temperature ratio, the relative kinetic energy and, hence, the magnitude of the disturbance is lower so that transition is less likely.

A.4.2 Correlation of the Empirical and Phsycial Disturbance Parameters, No Blowing

In this section, the relative kinetic energy at the top of the roughness elements, for $B' = 0$, is shown to be a function of $(T_e/T_w)(k/\theta)$ only; that is, there is very little explicit dependence of $\rho_k u_k^2/\rho_e u_e^2$ on T_w/T_e.
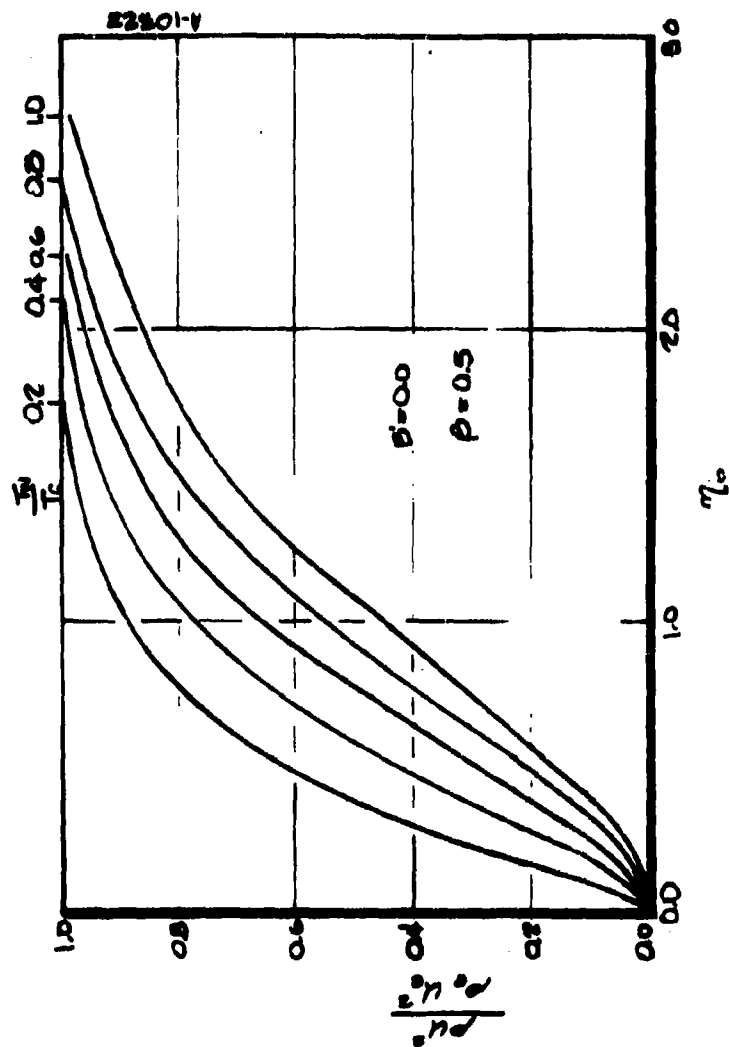
Figure A-13. Influence of wall cooling ratio on the relative kinetic energy.

A-33

The roughness elements are treated as if they protrude a distance k/2 into a
smooth wall boundary layer. This is essentially the distance from the mean surface
location. For selected values of $(T_e/T_w)(k/\theta)$ and T_w/T_e, the dimensionless location
of the top of the roughness elements in the boundary layer may be written as

$$\eta_0\left(\frac{k}{2}\right) = \frac{1}{2}\left(\frac{T_w}{T_e}\right)\left(\frac{T_e}{T_w}\ \frac{k}{\theta}\right)\eta_0(\theta)$$

The dimensionless momentum thickness,

$$\eta_0(\theta) = \sqrt{\frac{2\rho_e}{\mu_e}\ \frac{du_e}{ds}}\ \theta$$

is, for $B' = 0$ and $\beta = 0.5$, a function of T_w/T_e only. This function, evaluated from
BLIMP solutions is shown in Figure A-14. Also shown are values of this function
calculated by Dewey and Gross (Reference A-9) who report integral parameters and
wall derivatives for similar laminar boundary layer solutions. For laminar boundary
layers with no blowing, such close agreement (~1 percent) is expected.

Now, the kinetic energy may be picked off the appropriate cooling ratio curve
in Figures A-13. The results of this exercise are shown in Figure A-15. Clearly, the
two disturbance parameters correlate very well with each other. The conclusions is
that the transition Reynolds numbers (Re_θ) could have been correlated with the kinetic
energy ratio ($\rho_k u_k^2/\rho_e u_e^2$) about as well as with the empirical disturbance parameter
$(T_e/T_w)(k/\theta)$. Indeed the correlation shown in Figure A-15 indicates that the wind
tunnel data substantiate the hypothesis, stated above, regarding the key physical
measure of the disturbance.

Other profile parameters, u_k/u_e, $\rho_k u_k/\rho_e u_e$, and $u_k \nu_e/u_e \nu_k$, were examined in
addition to the kinetic energy ratio as candidates for the physical measure of the
disturbance. None of these correlates well with the empirical measure of the dis-
turbance, $(T_e/T_w)(k/\theta)$, and therefore all were rejected.

A.4.3 Effects of Blowing on the Roughness-Induced Disturbance

Because the kinetic energy profile adequately represents the effect of wall
temperature ratio variation on the rough wall disturbance, it is now assumed that the
modifications to the kinetic energy profile associated with blowing would likewise
be reflected in a modified rough wall disturbance. Therefore, boundary layer calcu-
lations including both blowing and wall cooling ratio variations were carried out
in order to provide kinetic energy profiles from which to assess modified disturbance
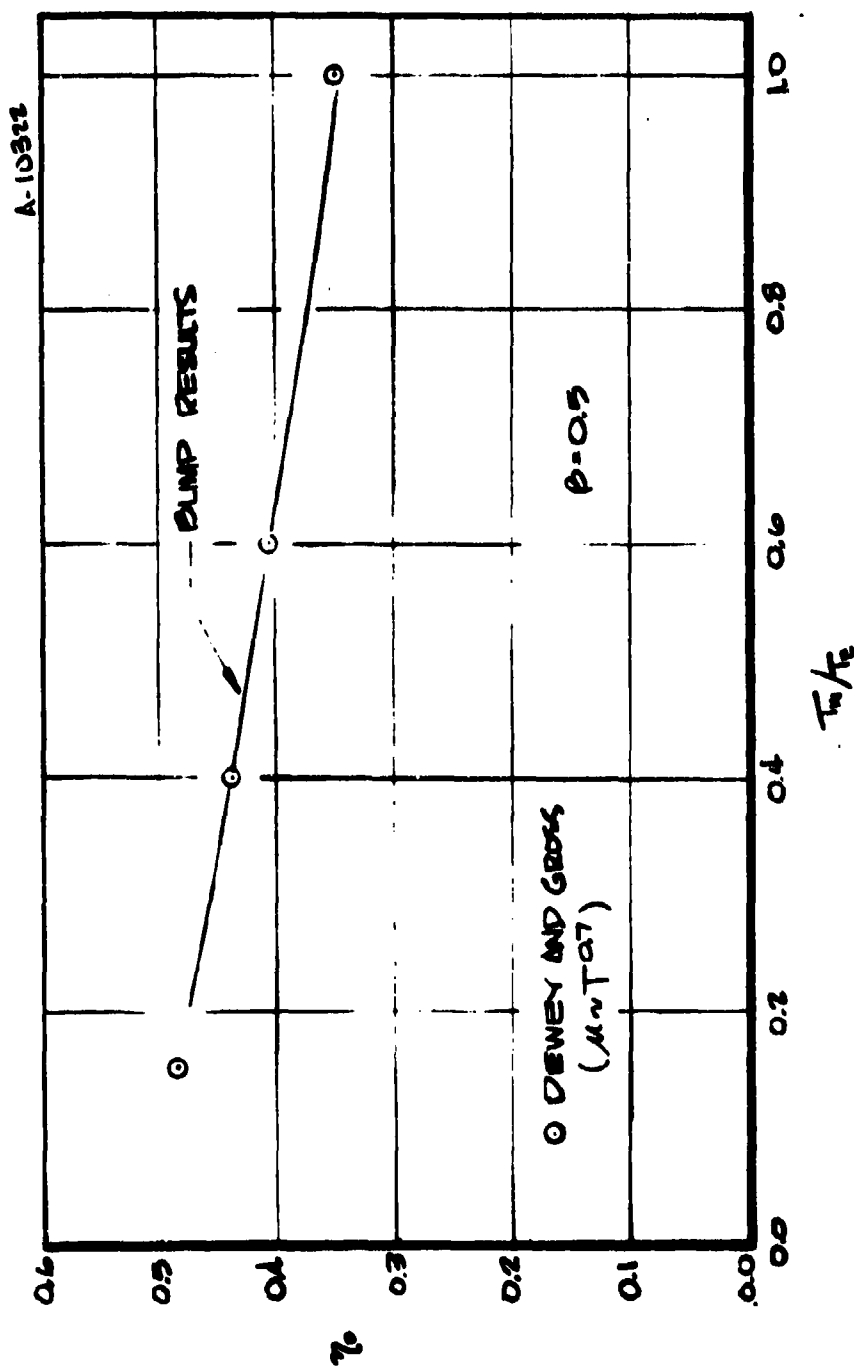magnitudes.

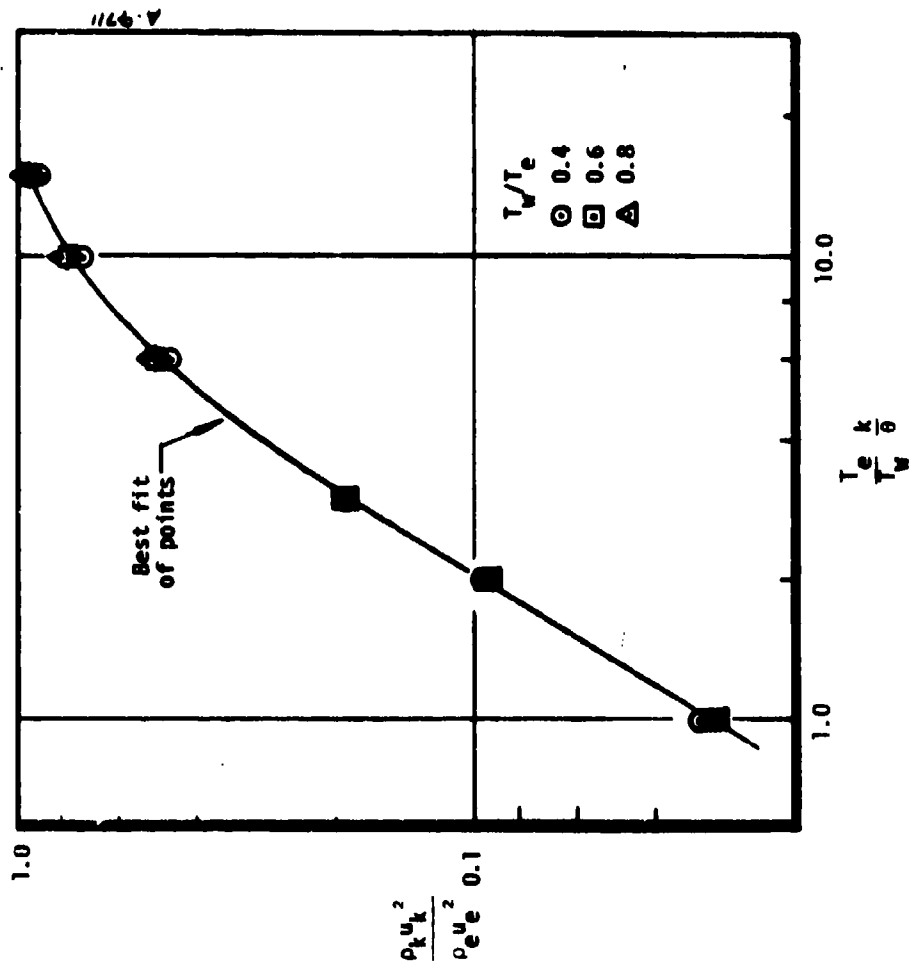Figure A-14. Dimensionless momentum thickness for B' = 0.

Figure A-15. Correlation of relative kinetic energy with the empirical disturbance parameter.

Figures A-16a, b, and c show the influence of air to air blowing on the kinetic energy profile for the wall cooling ratio range of primary interest. Note that blowing decreases the kinetic energy at any fixed n_0, an effect which is similar to the effect of increasing the wall cooling ratio.

Since boundary layer profiles are not usually generated during engineering reentry heat transfer calculations, the relative kinetic energy itself is not really suitable for use directly in a transition criterion. Rather, it is more useful to reverse the procedure which led to the establishment of the relative kinetic energy ratio as the physical measure of the disturbance. The object then is to establish a correlation between the physical disturbance parameter, $\rho_k u_k^2/\rho_e u_e^2$, and some modified empirical disturbance parameter, say

$$\frac{1}{\psi(T_w/T_e, B')} \frac{k}{\theta}$$

Since ψ replaces the wall cooling ratio in the empirical disturbance parameter, it must reduce to the cooling ratio for $B' = 0$.

The function $\psi(T_w/T_e, B')$ may be defined as that value of $(T_w/T_e)_{B'=0}$ which leads to the same relative kinetic energy at the same position in the boundary layer. For several discrete values of n_0, lines of constant B' were plotted on a relative kinetic energy versus wall cooling ratio plane. One of these plots is shown in Figure A-17 where some examples of ψ determinations are illustrated. Values of ψ from several such plots are shown correlated in Figure A-18. The straight lines shown have the equation

$$\psi = \frac{B'}{10} + \left(1 + \frac{B'}{4}\right) \frac{T_w}{T_e}$$

Figure A-19 substantiates this result. The correlation obtained for no blowing in Figure A-15 remains valid for the solutions which include blowing when the empirical disturbance parameter is modified as indicated above. The relative kinetic energy for each point shown on the graph is determined from the plots in Figures A-16a, b, and c, using the no blowing dimensionless momentum thickness evaluated at the actual wall cooling ratio to calculate $n_0(k/2)$.

A.4.4 Implications for Graphite Ablation in Flight

The primary differences between the flight and the low temperature air to air blowing situations just discussed are the differences in chemical composition arising from dissociation and graphite ablation. With molecular weight varying through the boundary layer, the density distribution is no longer the inverse of the temperature
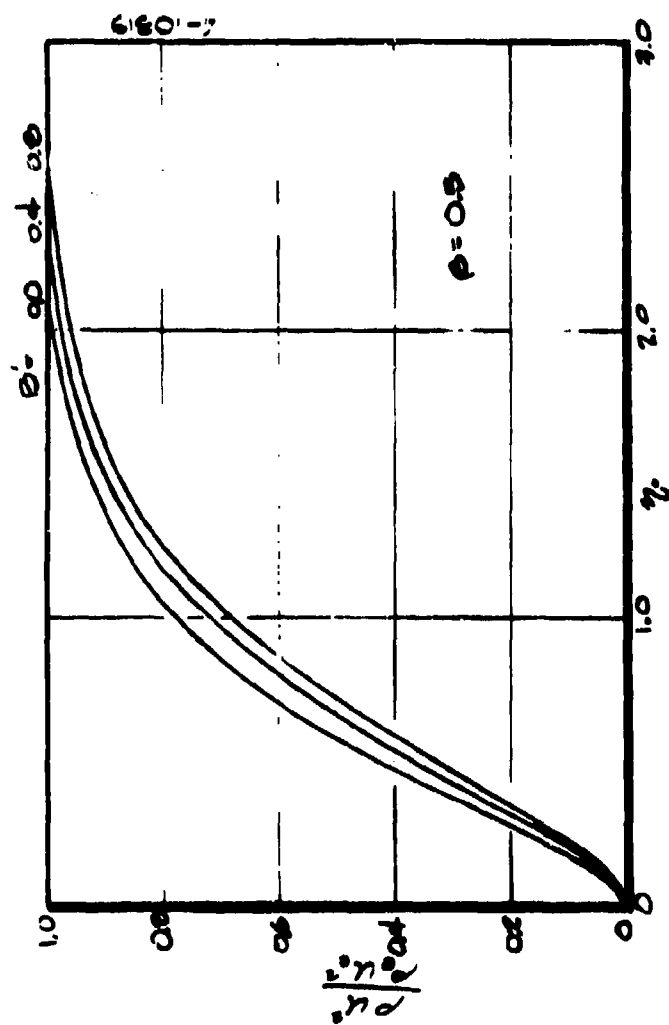
Figure A-16. Influence of air to air blowing on the relative kinetic energy.
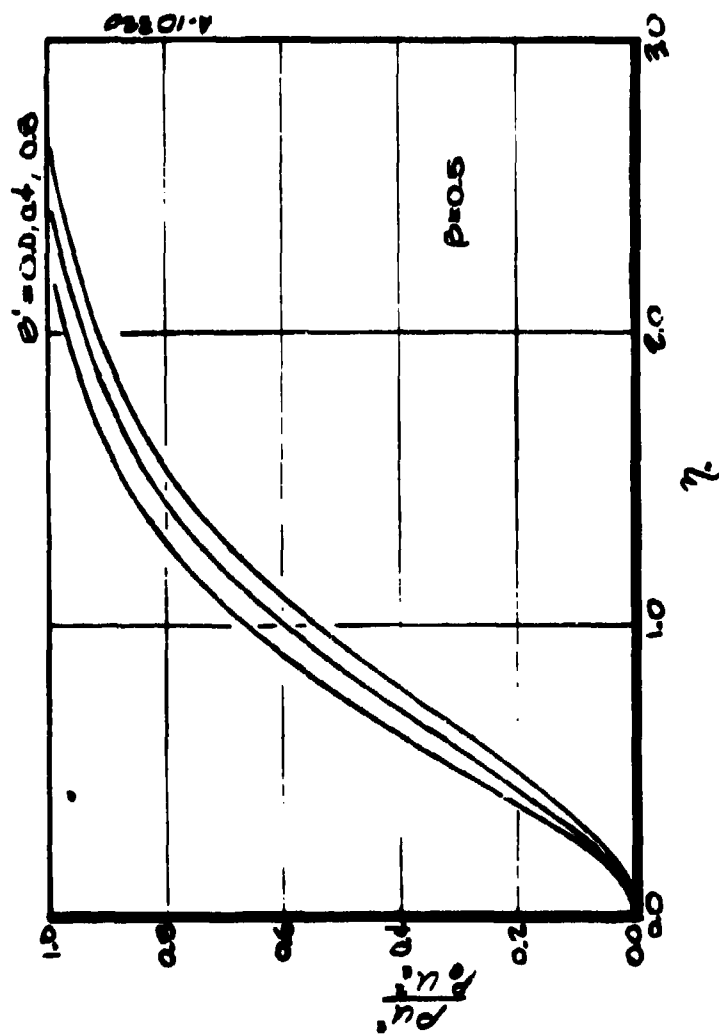
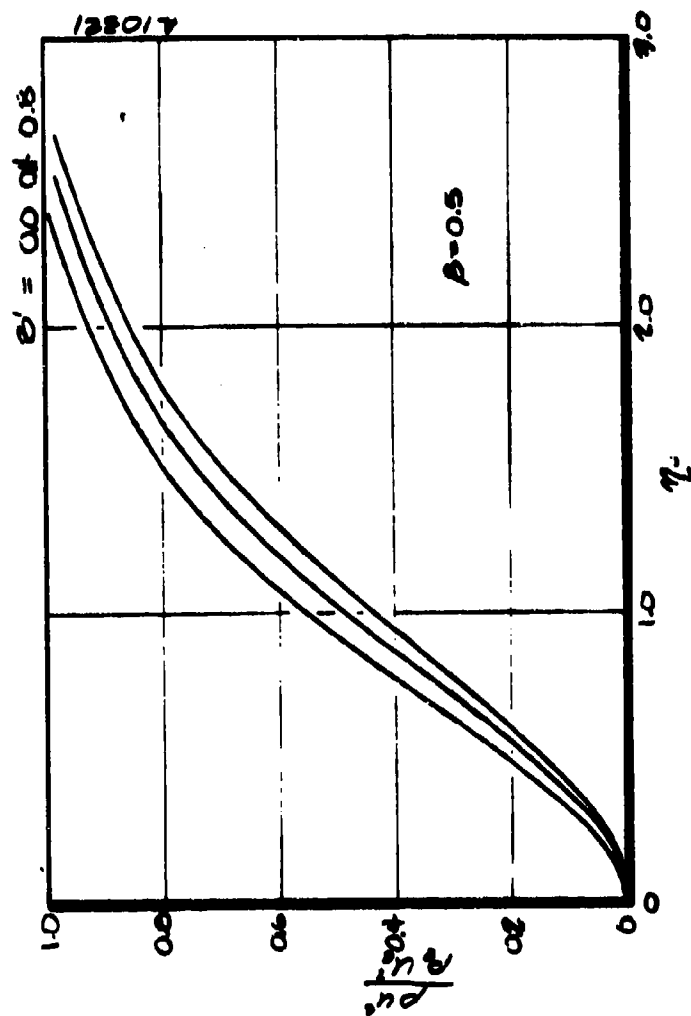(a) $T_w/T_e = 0.4$.

Figure A-16. (Continued)
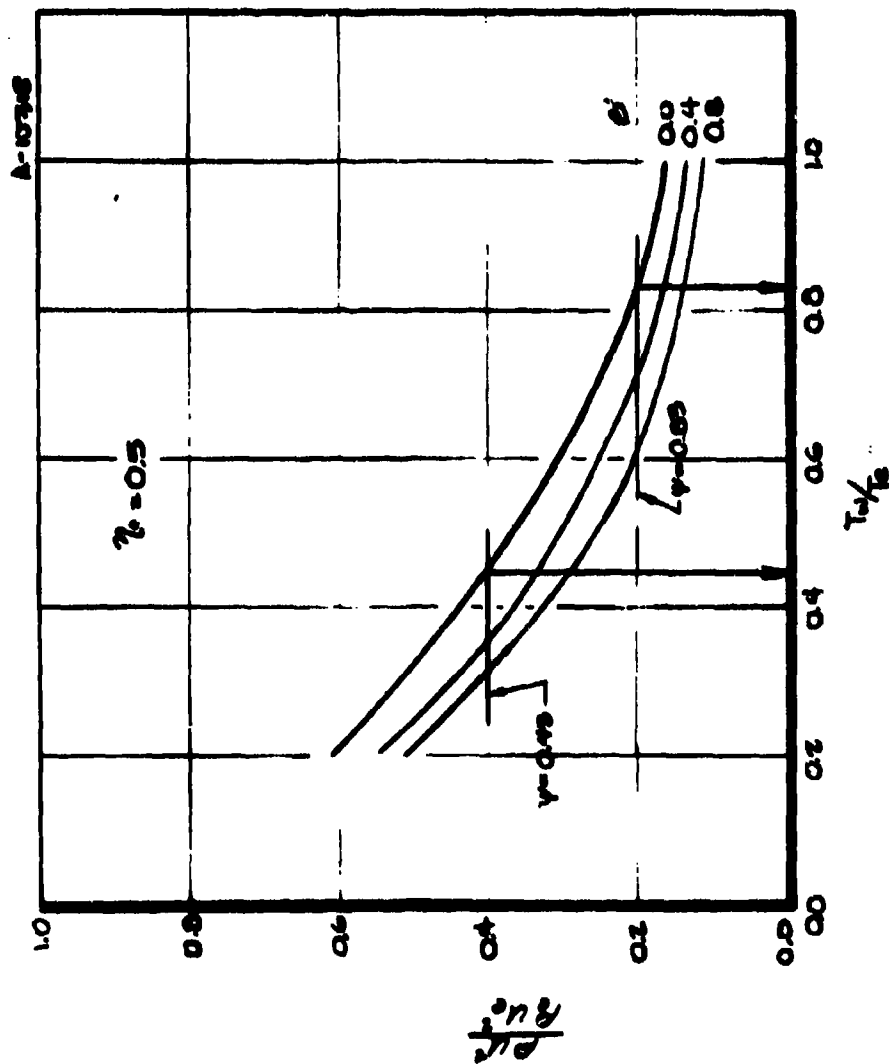(b) $T_w/T_e = 0.6$.

Figure A-16. (Concluded)
(c) $T_w/T_e = 0.8$.

A-40

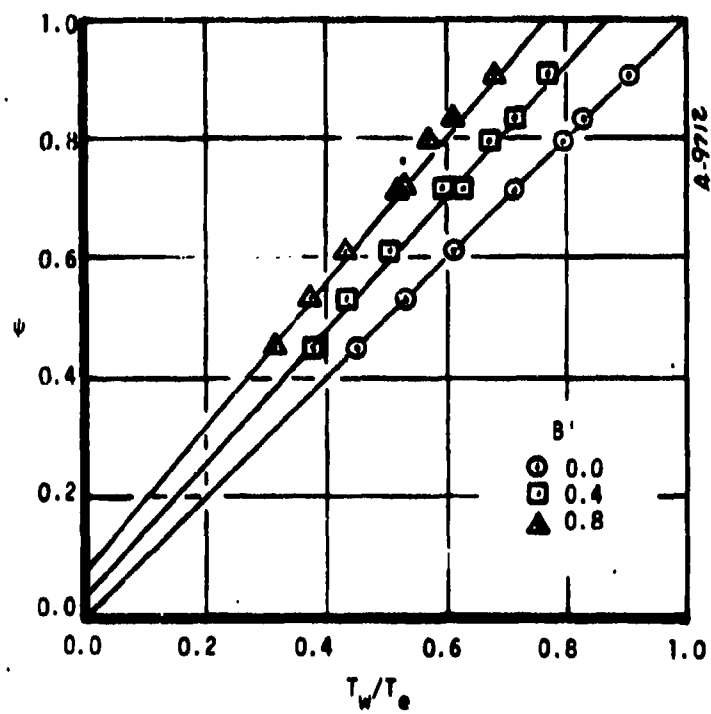Figure A-17. Example determinations of $\psi(T_w/T_e, B')$.

Figure A-18. Correlation of the effect of blowing on the relative kinetic energy.

$$\phi = \frac{B'}{10} + \left(1 + \frac{B'}{4}\right)\frac{T_w}{T_e}$$

From Figure A-15

$\frac{1}{\psi}\frac{k}{\theta}$

$\frac{\rho_k u_k^2}{\rho_e u_e^2}$

1.0

0.1

1.0   10.0

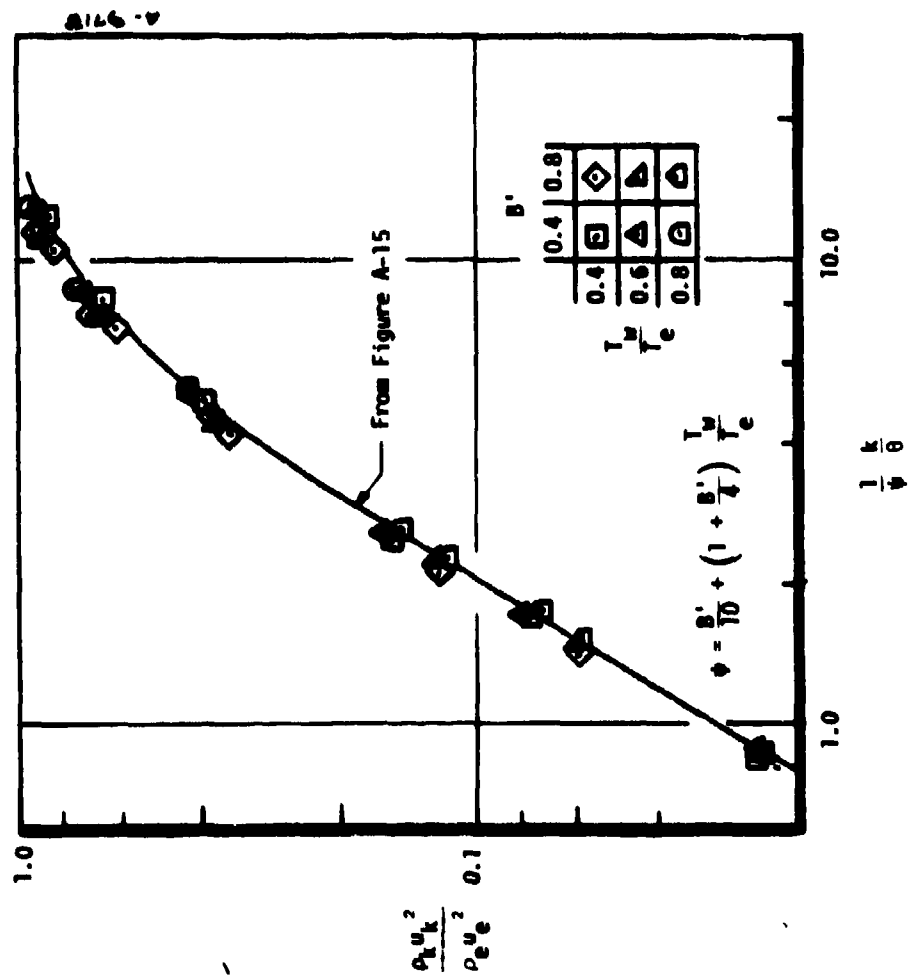| $\frac{T_w}{T_e}$	B'	
	0.4	0.8
0.4	◻	◇
0.6	◣	◢
0.8	◪	◨

Figure A-19.   Correlation of the relative kinetic energy with the modified empirical disturbance parameter.

A-43

distribution. Since density appears directly in the kinetic energy, it would seem more appropriate to use the density ratio, ρ_e/ρ_w, in the empirical disturbance parameter rather than the wall cooling ratio.

Two additional BLIMP calculations were performed in order to assess this proposed ρ_e/ρ_w modification. A graphite ablation solution was generated for a typical reentry situation at 50,000 feet assuming chemical equilibrium and a steady state surface energy balance. Using the wall temperature found for that case, a non-ablating solution was generated so that the influence of dissociation could be examined independent of ablation. These solutions were used to test the correlation between relative kinetic energy and the disturbance parameter ($k/\psi\theta$) using alternate choices for ψ. Figure A-20 shows these results compared to the correlation line from Figure A-15.

For the nonablating solution, the correlation using the wall cooling ratio is unsatisfactory except near the outer edge of the boundary layer. Using the density ratio the points near the surface are brought nicely into line with the correlation obtained for low enthalpy conditions.

It also appears that the density ratio properly correlates the dimensionless momentum thickness. For this case, $\rho_e/\rho_w = 0.439$, while $\eta_o(\theta) = 0.431$. This is in agreement with the results presented in Figure A-14 when the abscissa is interpreted as the density ratio ($T_w/T_e = \rho_e/\rho_w$ for the solutions on which this figure is based).

When the density ratio is used in conjunction with the blowing term developed earlier, the ablating solution is also well correlated. Although this technique does not yield a good correlation near the edge of the boundary layer, this region is not too important because, for flight conditions of interest, roughness heights are less than subsonic boundary layer thicknesses. Thus, the best choice for the disturbance is $k/(\psi\theta)$, where

$$\psi = \frac{B'}{10} + \left(1 + \frac{B'}{4}\right) \frac{\rho_e}{\rho_w}$$

The density ratio, as used here, includes the effects of ablation. This quantity is not readily available from engineering codes but its calculation is within the scope of this type of code. For the case of graphite ablation, use of the air density at the correct wall temperature would result in $k/\psi\theta$ being about 10 percent low. This in turn results in a 2 kft lower transition altitude prediction.
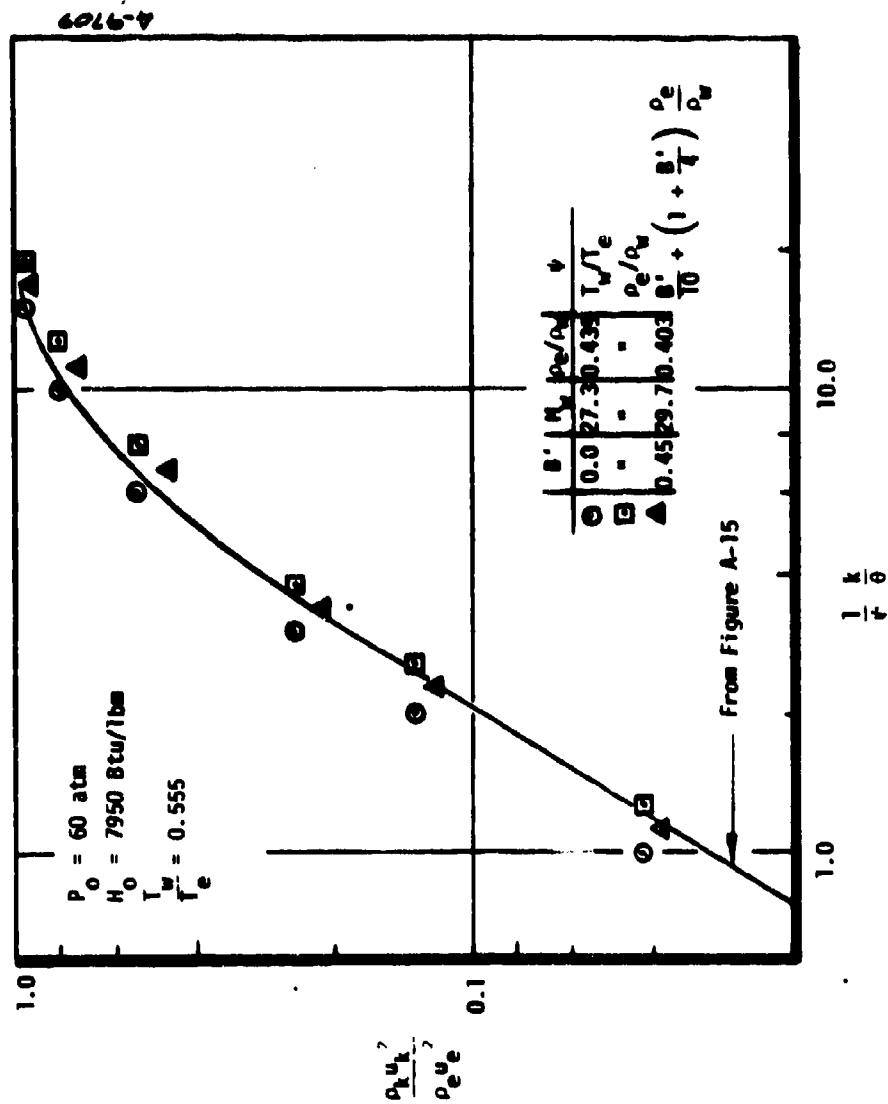
Figure A-20. Correlation of the relative kinetic energy with the modified disturbance parameter for flight conditions.

In summary, transition location and onset criteria, obtained as correlations of solid calorimeter wind tunnel data, have been rationally extended to include the flight case of carbon ablation at high enthalpy. Accurate prediction of transition during flight should now be possible provided sufficiently accurate evaluation of the surface roughness height is performed. Since fabrication variations apparently produce significant differences in surface roughness within a particular type of graphite (ATJ-S, for example), the determination of roughness height should be carried out using a similarly prepared sample. Furthermore, the appropirate roughness is the one produced after some amount of laminar ablation.

REFERENCES FOR APPENDIX

A-1. Anderson, L. W. and Bartlett, E. P., "Boundary Layer Transition on Reentry Vehicle Nosetips with Consideration of Surface Roughness," Aerotherm TM-71-9, Project 7040, Contract F04701-71-C-0027, July 1971.

A-2. Anderson, A. D., "Passive Nosetip Technology (PANT) Program, Interim Report, Volume III, Surface Roughness Effects, Part III, Transition Data Correlation and Analysis," SAMSO-TR-74-86, Aerotherm Report 74-90, Aerotherm Division, Acurex Corporation, January 1974 (CONFIDENTIAL).

A-3. "A Recommended Revised Wind Tunnel Test Plan for the PANT Program," Aerotherm Technical Memorandum TM-71-12, C/N 7040.72, July 1971.

A-4. Powars, C. A., "Passive Nosetip Technology (PANT) Program, Interim Report, Volume III, Surface Roughness Effects, Part II — Roughness Augmented Heating Data Correlation Analysis," SAMSO-TR-74-86, Aerotherm Report 74-90, Aerotherm Division, Acurex Corporation, January 1974 (CONFIDENTIAL).

A-5. Jackson, M. D., Baker, D. L., and Powars, C. A., "Passive Nosetip Technology (PANT) Program, Interim Report, Volume III, Surface Roughness Effects, Part I, Experimental Data," SAMSO-TR-74-86, Aerotherm Report 74-90, Aerotherm Division, Acurex Corporation, January 1974.

A-6. Jackson, M. D., "Passive Nosetip Technology (PANT) Program, Interim Report, Volume XV, Roughness Induced Transition on Blunt Axisymmetric Bodies — Data Report," SAMSO-TR-74-86, Aerotherm Report 74-100, Aerotherm Division, Acurex Corporation, August 1974.

A-7. Schlichting, H., Boundary Layer Theory, translated by Dr. J. Kestin, Sixth Ed., McGraw-Hill Book Company, Inc., 1968.

A-8. Kendall, R. M. and Bartlett, E. P., "Nonsimilar Solution of the Multicomponent Laminar Boundary Layer by an Integral Matrix Procedure," AIAA Journal, Vol. 6, No. 6, June 1958, pp. 1089-1097.

A-9. Dewey, C. F., Jr. and Gross, J. F., "Exact Similar Solutions of the Laminar Boundary-Layer Equations," The Rand Corporation, RM-5089-ARPA, July 1967.